Molecular beam studies with a time-of-flight machine

molecular beam studies with a time-of-flight machine

H.C.W. Beijerinck

molecular beam studies with a time-of-flight machine

PROEFSCHRIFT

ter verkrijging van de graad van
doctor in de technische wetenschappen
aan de Technische Hogeschool Eindhoven
op gezag van de rector magnificus
prof.dr.ir. G. Vossers, voor een
commissie aangewezen door het college
van Dekanen, in het openbaar te verdedigen
op vrijdag 5 september 1975 te 16.00 uur.

door

Herman Coenraad Willem Beijerinck

geboren te 's-Gravenhage

Dit proefschrift is goedgekeurd door de promotoren

prof.dr. N.F. Verster en
prof.dr.ir. H.L. Hagedoorn

aan Jurriaan

CONTENTS

1.	INTRODUCTION	1
1.1.	Aim of the experiment	1
1.2.	History of the experiment	2
1.3.	Contents of thesis	3
2.	ELASTIC SCATTERING THEORY	5
2.1.	Introduction	5
2.2.	Elastic scattering in classical mechanics	7
2.3.	Quantum mechanical theory of elastic scattering	9
2.4.	Semiclassical correspondence	18
3.	INTRODUCTION TO THE SCATTERING EXPERIMENT	23
3.1.	The intermolecular potential	23
3.2.	Measurement of total cross-sections	28
4.	TIME-OF-FLIGHT METHOD	31
4.1.	Introduction	31
4.2.	CALIBRATION OF A TIME-OF-FLIGHT MACHINE FOR MOLECULAR BEAM STUDIES	33
4.2.0.	Abstract	33
4.2.1.	Introduction	33
4.2.2.	The time-of-flight method	34
4.2.3.	Description of the apparatus	36
4.2.3.1.	*Vacuum system*	36
4.2.3.2.	*Beam chopping*	37
4.2.3.3.	*Particle detecting*	39
4.2.4.	Signal at the detector	39
4.2.5.	Calibration of the flight-time scale	41
4.2.6.	Systematic errors in the time-of-flight spectrum	44
4.2.6.1.	*Memory effects in the ionizer*	44
4.2.6.2.	*Memory effects in the detector chamber*	46

4.2.7.	Calibration of the detector	47
4.2.8.	Acknowledgments	48
4.3.	Comparison of the single burst and the random correlation time-of-flight method	49
4.3.1.	Introduction	49
4.3.2.	General assumptions for the comparison	51
4.3.3.	The single burst method	52
4.3.4.	The correlation time-of-flight method	53
4.3.5.	Comparison of signal-to-noise ratio's	55
4.3.6.	Discussion	56
5.	MOLECULAR BEAM SOURCES	59
5.1.	General survey of beam sources	59
5.1.1.	Introduction	59
5.1.2.	Effusive source	60
5.1.3.	Supersonic beam source	62
5.2.	VELOCITY DISTRIBUTION AND ANGULAR DISTRIBUTION OF MOLECULAR BEAMS FROM MULTICHANNEL ARRAYS	67
5.2.0.	Abstract	67
5.2.1.	Introduction	68
5.2.2.	Flow description	68
5.2.3.	Theory	70
5.2.3.1.	*Transparent channel*	71
5.2.3.2.	*Opaque channel*	75
5.2.4.	Experimental set-up	79
5.2.4.1.	*Time-of-flight machine*	79
5.2.4.2.	*Rotatable source*	81
5.2.4.3.	*Multichannel arrays*	82
5.2.5.	Experimental results	83
5.2.5.1.	*Transmission probability*	83
5.2.5.2.	*Peaking factor*	85
5.2.5.3.	*Angular distribution*	85
5.2.5.4.	*Center-line velocity distribution*	87
5.2.5.5.	*Off center-line velocity distribution*	90

5.2.6.	Conclusions	90
5.2.7.	Acknowledgments	91
5.3.	MONTE CARLO CALCULATION OF MOLECULAR FLOW THROUGH A CYLINDRICAL CHANNEL	93
5.3.0.	Abstract	93
5.3.1.	Introduction	93
5.3.2.	Molecular flow through a cylindrical channel	94
5.3.3.	The Monte Carlo program	100
5.3.3.1.	*The position of first collision*	102
5.3.3.2.	*The displacement along the axis*	103
5.3.4.	The wall collision rate and the angular distribution	105
5.3.4.1.	*Channel with $l = 2$*	105
5.3.4.2.	*Channel with $l = 25$*	107
5.3.5.	Transmission probabilities	108
5.3.6.	Collision number distribution	109
5.3.7.	Conclusions	114
5.3.8.	Appendix	115
6.	THE NEW TIME-OF-FLIGHT MACHINE	119
6.1.	Introduction	119
6.1.1.	*The cryopumping facility*	121
6.1.2.	*The computer facility*	122
6.2.	Vacuum system	123
6.2.1.	*Differential pumping*	126
6.3.	Primary beam	127
6.3.1.	*Beam source*	127
6.3.2.	*Beam collimation*	127
6.4.	Chopper motor	129
6.4.1.	*Synchronization assembly*	131
6.4.2.	*Constructure features*	133
6.5.	Secondary beam	135
6.6.	Detector system	137
6.6.1.	*Ionizer design*	139
6.6.2.	*Construction of the detector*	141

6.6.3.	*Performance of the detector*	141
6.7.	Data acquisition with the PDP-11	143
6.7.1.	*The time-of-flight multiscaling interface*	145
7.	TOTAL CROSS-SECTION MEASUREMENTS	149
7.1.	Angular resolution	149
7.2.	Velocity resolution	154
7.3.	Analysis of the results	156
7.4.	Discussion of the results	163
8	CONCLUSIONS	167
	References	169
	Summary	175
	Samenvatiing	177
	Nawoord	179
	Levensloop	179

1. Introduction

1.1. Aim of the experiment

During the last years it has been realised that to determine the interaction potential for two atoms one has to use information of a variety of experiments (or theories), as each experiment (theory) only probes a limited part of the potential. For the like pairs of rare gas atoms the following sources of information have been used: spectroscopic data on vibrational levels of dimers, crystallographic data, shock wave data, transport properties as viscosity and thermal conductivity, second virial coefficients, liquid state properties, theory (long range forces) and last but not least the increasing amount of molecular beam scattering data, i.e. measurements of the differential and the total cross-section.

In this introduction we limit ourselves to a discussion of the total cross-section. The average behaviour of the velocity dependence of the total cross-section only reflects the long range forces at large interatomic separations. Interference effects in the total cross-section, the so-called glory oscillations, give additional information on the potential well. Measurements of the total cross-section can supply additional information for fixing a unique potential.

To obtain valueable information from total cross-section measurements the following conditions have to be fulfilled:
- a high angular resolution, of the order of $3\ 10^{-4}$ radian, to limit the corrections on the experimental data to a few percent;
- a well calibrated scale of the relative velocity, with an accuracy of one percent or less, for an accurate determination of the positions of the glory extrema;
- a good resolution of the relative velocity, of the order of five percent, to measure glory oscillations that are only slightly damped;
- a high accuracy of the measurement of the attenuation, of the order of one percent or less, as the amplitude of the glory oscillations is only of the order of ten percent of the total cross-section.

Considering these demands, the time-of-flight method for the analysis of velocity distributions has a number of promising features. Simultaneous analysis of a broad velocity region eliminates drift of the measuring equipment and increases the relative accuracy of measurements at different velocities. An accurate calibration of the velocity scale and flexibility in choosing the velocity resolution are two qualities inherent to the time-of-flight method. Measuring times get quite long and automation of the experiments is inevitable. With the time-of-flight method this is readily achievable.

The first aim was to develop the time-of-flight method into a reliable and well calibrated method for analysing the velocity distribution of a molecular beam.

The second aim was the research on molecular beam sources with the time-of-flight machine, both to achieve a better fundamental understanding of their operation and to develop well determined primary and secondary beam sources.

The third aim is the use of the time-of-flight method to measure the velocity dependence of the total cross-section for all like and unlike pairs of rare gas atoms.

1.2. History of the experiment

At the beginning of 1970 our first time-of-flight machine became operational. It was used to investigate the time-of-flight method and for research on molecular beam sources. The latter is still the main aim of the current research with this old machine.

In the fall of 1971 we decided to design and build an improved time-of-flight machine, which became operational in the end of 1974. The new machine is alternately used for several research projects, two of which are the basis for a thesis.

The first project is the measurement of the velocity dependence of the total cross-section for elastic atom-atom scattering. Interesting features of the total cross-section are the glory undulations, the symmetry undulations for like pairs of atoms and the small angle differential scattering cross-section. The first results are reported in chapter 7 of this thesis.

The second project is a detailed investigation of supersonic expansion into a vacuum under near-ideal conditions, as provided by the 20 K cryopumping facility (section 6.1.). This research will be the subject of the thesis of Habets (scheduled 1976).

1.3. Contents of thesis

In chapter 2 we review elastic scattering theory. The total cross-section and the small angle differential cross-section are treated in so far as needed for a discussion of the experimental results in chapter 7.

In chapter 3 we briefly review the experimental and theoretical information on the intermolecular potential, with special emphasis on the Ar-Ar potential. Molecular beam scattering experiments are discussed in general and our experimental method is compared with other methods used.

In chapter 4 the time-of-flight method is treated. The single burst time-of-flight method is compared with other ways of velocity selection, with special emphasis on the comparison with the cross-correlation time-of-flight method. An experimental investigation and calibration of the old time-of-flight machine is also presented in this chapter.

In chapter 5 we give a general survey of molecular beam sources, i.e.the effusive source, the supersonic source and the multichannel source. The multichannel source has been investigated in detail, and both experimental and theoretical results are given.

In chapter 6 the design and the performance of the new time-of-flight machine are discussed and the experimental conditions of the total cross-section measurements (chapter 7) are given.

In chapter 7 the first experimental results for the measurement of the total cross-section are given for the systems Ar-Ar and Ar-Kr. Corrections due to the finite angular and velocity resolution of the apparatus are calculated.

Some parts of this thesis are integral copies of papers that have been published (section 4.2. and 5.2.) or that will be published (section 5.3.). For this reason the reader will encounter some

information more than once.

The thesis reports on measurements with two different time-of-flight machines. In chapter 4 and 5 all measurements have been performed with the old time-of-flight machine; the chapters 6 and 7 concern the new time-of-flight machine.

2. Elastic scattering theory

2.1. Introduction

In this chapter we give a short survey of the quantum mechanical theory of elastic scattering to introduce the scattering formula we need in chapter 7 for the evaluation of the total cross-section measurements and to obtain the design requirements for the measuring instrument. Attention is paid to the semiclassical correspondence of classical particle trajectories with the partial waves of the quantum mechanical solution.

For a more detailed treatment of the elastic scattering process the reader is referred to the following books. The classical description of elastic scattering is treated in a clear way by Landau and Livshitz (LAN 60), in part I of their series on theoretical physics. For a general treatment of the quantum mechanical theory one is referred to part III of the same series (LAN 67). Good reviews of the specific case of atom-atom elastic scattering are given by Pauly and Toennies (PAU 65) and Bernstein (BER 66). The semiclassical treatment of this case is discussed in a lucid way by Beck (BEC 70).

The interaction of two atoms is described by the spherically symmetric potential $V(r)$, with r their relative distance. To simplify the scattering problem we transform to a reduced coordinate frame where an incoming particle of reduced mass $\mu = m_1 m_2/(m_1 + m_2)$ moves with a position $\vec{r} = \vec{r}_1 - \vec{r}_2$ and a velocity $\vec{g} = \vec{v}_1 - \vec{v}_2$ in a fixed potential field $V(r)$, with $(m_i , \vec{r}_i , \vec{v}_i)$ the mass, position and velocity respectively of particle i in the laboratory (L) system. Scattering results obtained in this reduced system are equivalent to those in the center-of-mass (CM) system, where the center-of-mass is at rest.

Figure 2.1. Classical elastic scattering in a Lennard-Jones potential.
Top: Lennard-Jones potential (equation (2.6)).
Middle: Classical trajectories of the incident particles for different impact parameters b , at an energy $\mu g^2/2 = 2\varepsilon$.
Bottom (right): Classical scattering angle θ *as a function of the impact parameter b (equation (2.1)).*
Bottom(left) The three contributions to the classical differential cross-section. The numbers 1, 2 and 3 refer to the different contributing impact parameters in $\theta(b)$.

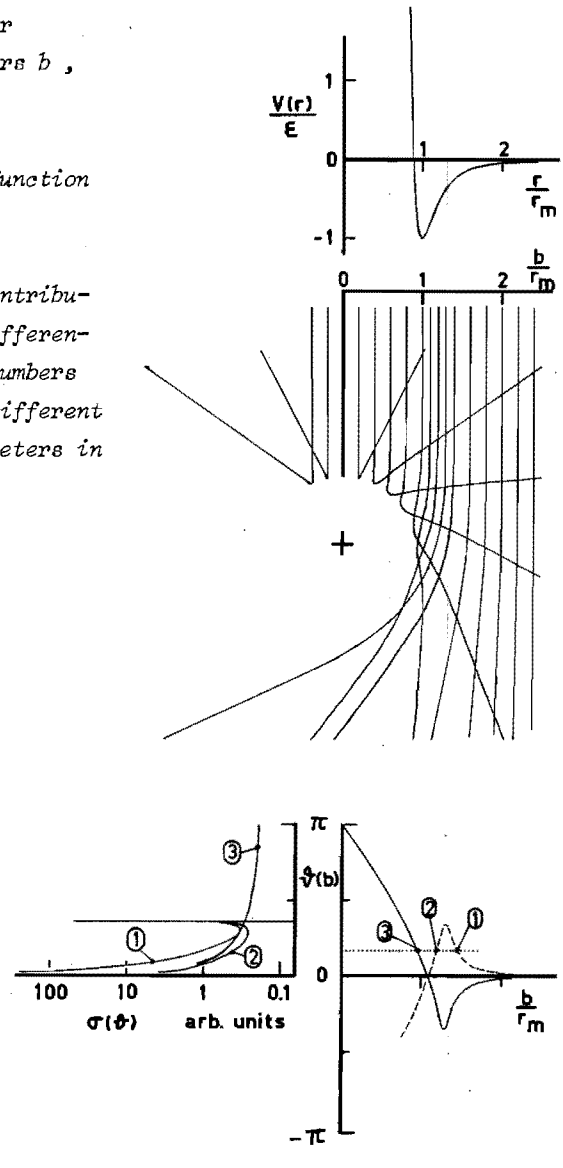

2.2. Elastic scattering in classical mechanics

We first discuss elastic scattering within the framework of classical mechanics. For the incident particle with impact parameter b the scattering angle θ is given by

$$\theta(b) = \pi - 2 \int_{r_c}^{\infty} \frac{b \, dr}{r^2 (1 - 2V(r) / \mu g^2 - b^2/r^2)^{\frac{1}{2}}} \qquad (2.1)$$

where r_c is the classical turning point, i.e. the zero of the denominator of the integrand. The differential cross-section $\sigma(\theta)$ (m^2 sr^{-1}) is defined as the intensity per unit of solid angle divided by the incident flux, and is given by

$$\sigma(\theta) = \sum_i \frac{b_i}{\sin\theta \left|\frac{d\theta}{db}\right|_i} \qquad (2.2)$$

as a summation over the contribution impact parameters b_i. For an attractive potential of type $V(r) = - C_s/r^s$ the scattering angle for large impact parameters can be calculated by integration of the tangential force over a straight line trajectory (which is equivalent to expanding equation (2.1) for large b), resulting in

$$\theta(b) = (s - 1) f(s) \left(\frac{2 C_s}{\mu g^2}\right) b^{-s} \qquad (2.3)$$

with

$$f(s) = \pi^{\frac{1}{2}} \frac{\Gamma\left(\frac{s-1}{2}\right)}{\Gamma\left(\frac{s}{2}\right)}$$

With equation (2.2) and (2.3) the small angle differential cross-section is given by

$$\sigma(\theta) = \frac{1}{s} \left(\frac{2(s-1) f(s) C_s}{\mu g^2} \right)^{2/s} \theta^{-2 - 2/s} \qquad (2.4)$$

and $\sigma(\theta)$ goes to infinity in the limit of $\theta \to 0$. The total cross-section Q is defined as

$$Q = \int_0^{\pi} \sigma(\theta) \quad 2\pi \sin\theta \quad d\theta \tag{2.5}$$

which is singular dueto the infinite range of the potential (equation (2.4)).

In figure 2.1 we show the classical particle trajectories, the deflection function $\theta(b)$ (equation (2.1)) and the contribution of the different impact parameters b_i to the differential cross-section $\sigma(\theta)$ (equation (2.2)) for a Lennard-Jones potential, given by

$$V(r) = \varepsilon \{ (\frac{r_m}{r})^{12} - 2(\frac{r_m}{r})^{6} \} \tag{2.6}$$

with ε and r_m the depth and the position of the potential well respectively, which is the traditional example for the interaction potential of two atoms. The energy of the incident particle in figure 2.1 is $\mu g^2 / 2 = 2\varepsilon$.

For small angles the function $b(\theta)$ is triple valued. The contribution of the impact parameters b_2 and b_3 to the small angle differential cross-section is proportional to θ^{-1} (equation (2.)) and can be neglected in comparison with the contribution of the large impact parameter b_1 , as given in equation (2.4).

Due to the wave nature of the colliding partners the actual scattering process differs in various aspects from the classical picture given in this section. In equation (2.2) for the differential cross-section,interference of the different contributing branches of the deflection function has to be taken in account. The uncertainty relation modifies the scattering process at small angles ($\theta \sim \lambda\!\!\!^{-}/r_m$) and the small angle differential cross-section of equation (2.4) levels off to a finite value for $\theta = 0$. Consequently the total cross-section also becomes finite. In the total cross-section interference effects are also present, due to the existence of a zero in the

deflection function $\theta(b)$. The full quantum mechanical solution is discussed in the following section.

2.3. Quantum mechanical theory of elastic scattering

In the quantum mechanical description of elastic scattering the problem is to solve the time-independent Schrödinger equation

$$(\Delta + k^2)\ \Psi\ (r\ ,\ \theta) = \frac{2\mu}{\hbar^2}\ V(r)\ \Psi\ (r\ ,\ \theta) \qquad (2.7)$$

with $k = \mu g\ /\ \hbar \quad (2\ \mu E/\hbar^2)^{\frac{1}{2}}$ the wave number of the incident wave. The desired solution behaves asymptotically as

$$\Psi\ (r\ ,\ \theta) = e^{ikr\ \cos\theta} + f(\theta)\ \frac{e^{ikr}}{r} \qquad (2.8)$$

The first term represents the incident plane wave along the z-axis, the second term is the outgoing spherical wave. The function $f(\theta)$ is called the scattering amplitude. The differential cross-section $\sigma(\theta)$ is given by

$$\sigma(\theta) = |\ f(\theta)\ |^2 \qquad (2.9)$$

The total cross-section Q is given by equation (2.5). With the optical theorem Q is given by

$$Q = \frac{4\pi}{k}\ \mathrm{Im}\ f(0) \qquad (2.10)$$

For measurements of the total cross-section Q, which have to be corrected with the differential cross-section $\sigma(0)$ (or $\sigma(\theta)$ for very small θ) due to the finite angular resolution of the apparatus, we are interested in $f(0)$. In solving equation (2.7) the incident plane wave is expanded in a sum of incoming and outgoing partial waves, each with orbital angular momentum l. The effect of the scattering potential $V(r)$ is to shift the phase of each outgoing partial wave by $2\eta_l$. The

result for $f(\theta)$ obtained by this method of partial waves is

$$f(\theta) = \frac{i}{k} \sum_{l=0}^{\infty} (l + \tfrac{1}{2}) (1 - \exp 2i\eta_l) P_l(\cos\theta) \qquad (2.11)$$

with P_l the Legendre functions.

The equations (2.8) and (2.11) are correct for collisions of non-identical particles. For identical particles Ψ has to be symmetrized, resulting in a scattering amplitude $f^*(\theta) = f(\theta) \pm f(\pi - \theta)$ where the plus sign is for the symmetric case and the minus sign is for the antisymmetric case. The scattering amplitude $f^*(\theta)$ differs from equation (2.11) by an extra factor 2 and a summation over only the even or odd l-terms respectively. The two contributions to $f^*(\theta)$ will cause an extra interference, the so-called symmetry or exchange oscillations. For heavy particles (argon) these oscillations are rapid and their relative contribution to the total cross-section and the small angle differential cross-section is very small and can be neglected. Apart from these oscillations the results derived in this section are the same for $f^*(\theta)$ and $f(\theta)$, and we will always use equation (2.11).

The phase shifts η_l are required to calculate the scattering amplitude in equation (2.11). They are determined by the asymptotic behaviour of the radial part of Ψ , which in general has to be calculated by a numerical solution of the radial Schrödinger equation. When large numbers of partial waves contribute this is a tedious job.

Approximate methods are available to determine η_l in the semi-classical case, when the wave length of the incident wave is small in comparison with the typical range of the potential (for Ar-Ar at g = 1000 m/s the quantity $r_m/\lambda\!\!\!^{-} = k\, r_m = 120$). The most important is the Jeffreys-Wentzel-Kramer-Brillouin (JWKB) method. The JWKB phase shifts are given by

$$\eta_l^{JWKB} = \lim_{R\to\infty} \{ \int_{r_c}^{R} (k^2 - \frac{2\mu V(r)}{\hbar^2} - \frac{(l+\frac{1}{2})^2}{r^2})^{\frac{1}{2}} \, dr$$

$$- \int_{r_c'}^{R} (k^2 - \frac{(l+\frac{1}{2})^2}{r^2})^{\frac{1}{2}} \, dr \} \qquad (2.12)$$

where r_c and r_c' are the zero's of the first and the second integrand respectively. The term $l(l+1)$ of the radial Schrödinger equation has been replaced by $(l+\frac{1}{2})^2$ as suggested by Langer. Only then the force-free JWKB radial function has the correct asymptotic behaviour.

The JWKB phase shifts and the classical scattering angle $\theta(b)$ are related by

$$\frac{d\, 2\, \eta_l^{JWKB}}{dl} = \theta(b(l)) \qquad (2.13)$$

as can be seen from equation (2.12) and (2.1). Equation (2.13) is often called the semiclassical equivalence relationship. The impact parameter b is related to l by the semiclassical relation $b = (l+\frac{1}{2})/k$.

For large l and/or small η_l values, i.e. small scattering angles $\theta < 0.1$, the phase shift can be calculated in the Jeffreys-Born (JB) or high energy approximation.

$$\eta_l^{JB} = \frac{1}{2\hbar g} \int_{-\infty}^{+\infty} V(r(b, z))\, dz \qquad (2.14)$$

where the integration is performed along a straight line parallel to the z-axis with an impact parameter b . For an attractive potential of type $V(r) = -C_s/r^s$ the JB phase shifts are $(s > 2)$

$$\eta_l^{JB} = \frac{C_s}{\hbar g} \left(\frac{l+\frac{1}{2}}{k}\right)^{1-s} f(s) \qquad (2.15)$$

with $f(s)$ as defined in equation (2.3). Equation (2.15) can also be directly calculated with equation (2.13) and equation (2.3) (for Ar-Ar

at g = 1000 m s^{-1} the phase shifts are $\eta_l = 1.1\ 10^{11}\ (l + \frac{1}{2})^{-5}$ assuming an $s = 6$ potential with $C_6 = 1.1\ \varepsilon\ r_m^6$ (see section 3.1.)).

In the Landau-Livshitz approximation the scattering amplitude $f(0)$ is calculated by using the η_l^{JB} and replacing the summation in equation (2.11) by an integral. The result is ($s > 3$)

$$f(0)_{attr} = |f(0)_{attr}| \exp i(\pi/2 - \pi/(s-1)) \qquad (2.16)$$

$$|f(0)_{attr}| = \frac{k}{2}\ \Gamma\left(\frac{s-3}{s-1}\right)\ (2\ f(s))^{2/(s-1)}\ \left(\frac{C_s}{\hbar g}\right)^{2/(s-1)}$$

The JB phase shifts become incorrect for $\frac{d\ 2\eta_l^{JB}}{dl} > 0.1$, corresponding to $\eta_l > 1$, but in this region $f(0)$ is insensitive to their exact value. The large phase shifts vary rapidly with decreasing l and the net result is that the terms $\sin 2\eta_l$ and $\cos 2\eta_l$ in $f(0)$ are replaced by their average value i.e. zero. Only the small phase shifts for large l contribute separately.

With equation (2.9), (2.10) and (2.16) the differential cross-section $\sigma(0)$ and the total cross-section Q are related by (figure 2.2)

$$\sigma(0)_{attr} = \frac{k^2\ Q_{attr}^2}{16\pi^2}\ \left(1 + \tan^2\left(\frac{\pi}{s-1}\right)\right) \qquad (2.17)$$

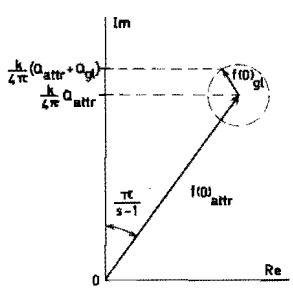

Figure 2.2. The scattering amplitude $f(0) = f(0)_{attr} + f(0)_{gl}$ *. With increasing relative velocity g the glory contribution* $f(0)_{gl}$ *rotates clockwise and causes glory oscillations in the total cross-section* $Q = (4\pi/k)$ Im $f(0)$ *and the differential cross-section* $\sigma(0) = |f(0)|^2$*, with a phase difference* $\pi/(s-1)$.

For $s = 6$ the total cross-section Q can be calculated from equation (2.10) and (2.16), resulting in

$$Q_{attr} = 8.083 \left(\frac{C_6}{\hbar g} \right)^{2/5} \qquad (2.18)$$

(for Ar-Ar at g = 1000 m/s the total cross-section $Q_{attr} = 2.6\ 10^2$ Å^2, by using $s = 6$ and $C_6 = 1.1\ \varepsilon\ r_m^6$ (see section 3.1); with equation (2.17) and $k\ r_m = 120$ the differential cross-section $\sigma(0)_{attr} = 6.9\ 10^5$ Å^2 sr^{-1}).

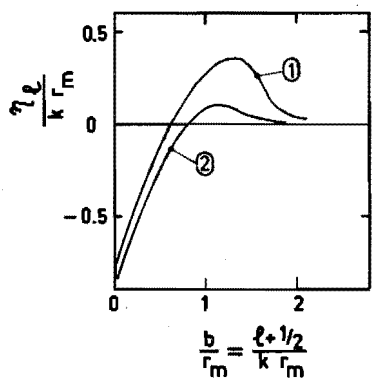

Figure 2.3. The phase shifts η_ℓ for a Lennard-Jones potential.
1) energy $\mu g^2/2 = \varepsilon$
2) energy $\mu g^2/2 = 4\varepsilon$ (PAU 65)

For a more realistic potential with a repulsive core (equation (2.6)) the phase shifts are given in figure 2.3. With decreasing ℓ the phase shifts rise to a maximum and then decrease to negative values due to the repulsive interaction. Near this maximum the phase shift is stationary and will contribute to $f(0)$ in a non-random way. The maximum $\eta_{\ell max}$ in the phase shift curve for $\ell = \ell max$ corresponds to a particle trajectory for which the attractive and repulsive forces cancel and the scattering angle $\theta = 0$ (equation (2.13)). We represent the phase shift function near $\ell = \ell max$ by a parabola (DUR 63)

$$\eta_\ell = \eta_{\ell max} + \tfrac{1}{2}\, \eta''_{\ell max}\, (\ell - \ell max)^2 \qquad (2.19)$$

and calculate the contribution $f(0)_{gl}$ to the scattering amplitude, resulting in ($\eta''_{l_{max}} < 0$)

$$f(0)_{gl} = |f(0)_{gl}| \quad \exp\{ i\,(2\eta_{l_{max}} - \pi/4) - i\,\pi/2 \}$$

$$|f(0)_{gl}| = \frac{\pi^{\frac{1}{2}}\,(l_{max} + \frac{1}{2})}{2k\;|\eta''_{l_{max}}|^{\frac{1}{2}}} \qquad (2.20)$$

which is called the glory contribution to the scattering amplitude.

The scattering amplitude of this realistic potential is given by the sum

$$f(0) = f(0)_{attr} + f(0)_{gl} \qquad (2.21)$$

as shown in figure 2.2. With decreasing $\eta_{l_{max}}$, i.e. increasing velocity, the vector $f(0)_{gl}$ rotates clockwise. In first order the length of the glory contribution to the scattering amplitude is $|f(0)_{gl}| \sim k$. From equation (2.16) one can derive $|f(0)_{attr}| \sim k\, g^{-2/(s-1)}$. The relative contribution of $f(0)_{gl}$ to the scattering amplitude increases proportional to $g^{2/(s-1)}$.

The extra contribution $f(0)_{gl}$ will cause oscillations in $\sigma(0)$ and Q, with a phase difference $(\pi / (s-1))$. The contribution to the total cross-section is

$$Q_{gl} = \frac{4\pi}{k}\,|f(0)_{gl}|\,\cos(2\eta_{l_{max}} + 3\pi/4) \qquad (2.22)$$

$$= A_{gl}\,\cos(2\eta_{l_{max}} + 3\pi/4)$$

and

$$Q = Q_{attr} + Q_{gl} = Q_{attr}\,(1 + \frac{A_{gl}}{Q_{attr}}\,\cos(2\eta_{l_{max}} + 3\pi/4)\,) \qquad (2.23)$$

The oscillations in Q are called glory oscillations. The total cross-section will have extrema at

$$\eta_{l\max} = (N - 3/8)\,\pi \qquad N = \begin{cases} 1,2,3.... & \text{for maxima} \\ 1.5,2.5,... & \text{for minima} \end{cases}$$

(2.24)

The maximum phase shift $\eta_{l\max}$ can be expanded in a series of the form (BER 73, BUC 72)

$$\eta_{l\max} = \frac{2\,\varepsilon\, r_m}{\hbar g} \sum_{i=0}^{\infty} a_i \left(\frac{\varepsilon}{E}\right)^i \qquad (2.25)$$

The first term $\eta_{l\max} = a_0^2\, \varepsilon\, r_m / \hbar g$ suffices for a qualitative description of the position of the extrema in the total cross-section, the coefficient $a_0 = 0.43 \pm 0.02$ depending on the specific potential model used (for Ar-Ar with $a_0 = 0.43$ the maximum phase shift is $\eta_{l\max} = \frac{6\ 10^3}{g}$).

For $\eta_{l\max} < 5\pi/8$ the separate treatment of the maximum in the phase shift curve and the small phase shifts for large l is no longer valid, and no further oscillations occur. With further decreasing $\eta_{l\max}$, i.e. increasing velocity, the cross-section will be determined mostly by the negative phases of the repulsive

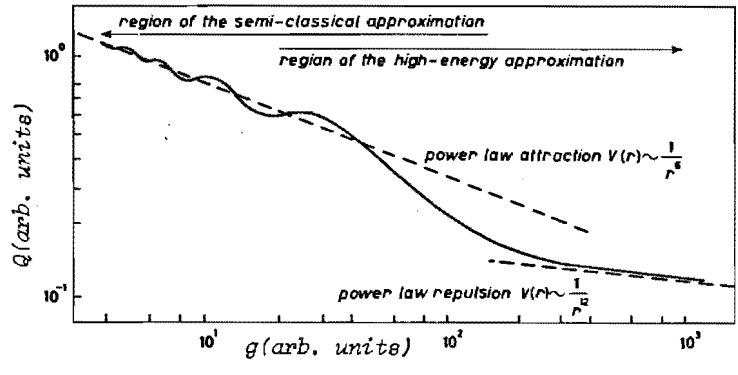

Figure 2.4. The total cross-section Q as a function of the relative velocity g, calculated for a Lennard-Jones potential (PAU 65).

branch of the potential (figure 2.4).

With the cosine rule (figure 2.2) and equation (2.9) we can calculate the differential cross-section $\sigma(0)$, resulting in

$$\sigma(0) = |f(0)_{attr}|^2 + |f(0)_{gl}|^2 - 2|f(0)_{attr}|\ |f(0)_{gl}| \times$$

$$\cos\ (2\eta_{l_{max}} + 3\pi/4 + \pi/(s-1)\ ) \qquad (2.26)$$

With equation (2.17) , (2.22) and (2.23) the differential cross-section $\sigma(0)$ in equation (2.26) can be written as (HEL 66)

$$\sigma(0) = \sigma(o)_{attr}\ \{1 + 2(\ \frac{A_{gl}}{Q_{attr}}\ )\ \cos(\pi/(s-1)) \times$$

$$\cos(2\eta_{l_{max}} + 3\pi/4 + \pi/(s-1)\ ) + (\ \frac{A_{gl}}{Q_{attr}}\ )^2\ \cos^2(\pi/(s-1))\} \qquad (2.27)$$

By neglecting the last term in (2.27) and comparing this equation with equation (2.23) we see that the oscillations in $\sigma(0)$ are a factor $2\ \cos(\pi/(s-1))$ larger than the oscillations in the total cross-section Q (for $s = 6$ this factor is equal to 1.62).

We now discuss the angular dependence of the differential cross-section $\sigma(\theta)$ for very small angles. In a simple approximation (BER 66) the Legendre functions $P_l(\cos\theta)$ are expanded in a Taylor series in $\theta = 0$, the sum in equation (2.11) is replaced by an integral and the JB phase shifts for an attractive potential $V(r) = -C_s/r^s$ are used. Only the integral of the constant and the quadratic term in the expansion of P_l converges, resulting in

$$\sigma(\theta)_{attr} = \sigma(0)_{attr}\ (1 - (\ \frac{\theta}{\theta^*}\ )^2\ ) \qquad (2.28)$$

with

$$\theta^* = (\ \frac{8\pi}{c(s)}\ )^{\frac{1}{2}}\ k^{-1}\ Q^{-\frac{1}{2}}$$

and

$$c(s) = \frac{\Gamma^2\ (2/(s-1))}{2\pi\ \Gamma(4/(s-1))} \quad \tan\ (2\pi/(s-1))$$

For $s = 6$ the value of $c(6) = 2.07$. By considering equation (2.28) as the first term in the expansion of an exponential function, it is written as

$$\sigma(\theta)_{attr} = \sigma(0)_{attr} \quad \exp - \left(\frac{\theta}{\theta^*}\right)^2 \qquad (2.29)$$

By comparison with the exact results for a Lennard-Jones potential the approximation of equation (2.29) has been improved, resulting in (BUS 67)

$$\sigma(\theta) = \sigma(0) \quad \exp - \left(\frac{\theta}{\theta^*}\right)^2 \quad \text{with } \theta^{**} = 1.20\ \theta^* \qquad (2.30)$$

This approximation is valid for angles θ in the range

$$\theta < (2\pi^3)^{\frac{1}{2}}\ k^{-1}\ Q^{-\frac{1}{2}} \qquad (2.31)$$

For larger angles the average behaviour of the differential cross-section is again described by the classical result for the differential cross-section, as given in equation (2.3).

All angles in this part are of the order of magnitude of $k^{-1}\ Q^{-\frac{1}{2}}$. The contribution ΔQ of the differential cross-section for $\theta \leq k^{-1}\ Q^{-\frac{1}{2}}$, i.e. a solid angle of $\pi\ k^{-2}\ Q^{-1}$, is in good approximation given by

$$\Delta Q = \pi\ k^{-2}\ Q^{-1}\ \sigma(0) \qquad (2.32)$$

Using $\sigma(0)_{attr}$ from equation (2.17) this results in

$$\Delta Q = \frac{Q}{16\pi}\ \left(1 + \tan^2\left(\frac{\pi}{s-1}\right)\right) \qquad (2.33)$$

If all differentially scattered particles with a scattering angle $\theta \leq k^{-1}\ Q^{-\frac{1}{2}}$ are detected the measured value Q_{eff} of the total cross-

section is (s = 6)

$$Q_{eff} = Q - \Delta Q = 0.97\ Q \qquad (2.34)$$

This calculation demonstrates an essential impact of theory on the measuring equipment. If we want to restrict the magnitude of the corrections which have to be applied to the order of a few percent, the angular resolution (in the CM system) has to be of the order of $k^{-1}\ Q^{-\frac{1}{2}}$ (for Ar-Ar at g = 1000 m/s the angle $k^{-1}\ Q^{-\frac{1}{2}} = 1.9\ 10^{-3}$ with $Q = 2.6\ 10^{2}$ Å^2). The transformation of the CM system to the L system is treated in section 7.1..

2.4. Semiclassical correspondence

In figure 2.5 (VER 73a) we show the classical particle trajectories in a Lennard-Jones potential $V(r)$ (equation (2.6)), with the same circumstances as in figure 2.1. Perpendicular to the z-axis (at position $z = z_0 = -3r_m$) a surface of constant action S = 0 is chosen. Particles with velocity g leave this surface parallel to the z-axis, i.e. perpendicular to the basic surface S = 0. Along the particle trajectories $s(x\ ,\ y\ ,\ z)$ the increase ΔS of the action is calculated as

$$\Delta S = \int_{s(b(x,y),z_0)}^{s(x,y,z)} \mu\ v(s)\ ds \qquad (2.35)$$

with $v(s)$ the velocity along the trajectory. At fixed intervals of ΔS a mark is set on the trajectory. By connecting the corresponding marks surfaces of equal action are constructed, and are indicated in figure 2.5. According to the Hamilton-Jacobi equation of classical mechanics the particle trajectories are perpendicular to these surfaces.

The surfaces of equal action in classical mechanics have their analog in optics as the surfaces of equal phase or wave fronts. Vice versa light rays in geometrical optics are the analog of particle trajectories in classical mechanics.

By introducing the De Broglie wave length

$$\lambda = h / \mu v(s) \tag{2.36}$$

of the particle, the surface of equal action in classical mechanics (equation (2.35)) become surfaces of equal phase ϕ of the matter waves, to which Huygens principle can be applied. In figure 2.5 the surfaces of equal action are drawn at intervals of 10 h, i.e. at intervals of 20 π in phase, and thus are wave fronts at intervals of ten wave lengths.

The solution of the Schrödinger equation in the JWKB approximation and this description have an equal range of validity, as the JWKB method assumes a solution $\Psi \sim \exp(iS/\hbar)$ of the Schrödinger equation. The main condition of validity is that the fractional change of the wave length per wave length is small. Only at the classical turning point this condition is not fulfilled.

In the limiting case of infinitely small wave length the Hamilton equation of classical mechanics (and geometrical optics) and the wave equation of Fresnel (and thus the Schrödinger equation) all coincide.

From this description we can derive the attenuation of the forward intensity, i.e. the total cross-section (VER 73). For large b the effect of the scattering potential is a phase difference $\Delta\phi(b)$ between the actual wave front and the plane wave front of the undisturbed beam. With decreasing b this phase difference increases rapidly. The contribution of an angular surface element of radius b and width db to the wave amplitude in forward direction is reduced by a factor factor $\cos(\Delta\phi(b))$. The total loss in amplitude is given by

$$Q' = \int_0^\infty \{ 1 - \cos(\Delta\phi(b)) \} 2 \pi b \, db \tag{2.37}$$

The corresponding loss in intensity Q is given by

$$Q = 2Q' \tag{2.38}$$

Integrating (2.35) along a straight line (which is a good approximation

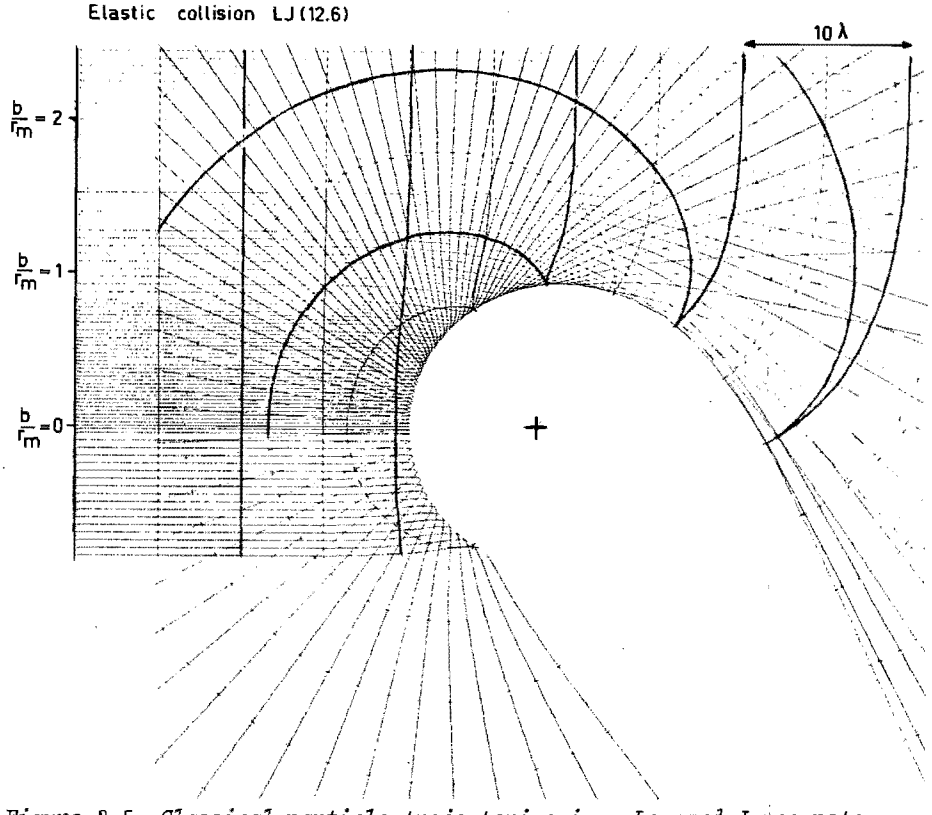

Figure 2.5. Classical particle trajectories in a Lennard-Jones potential for $\mu g^2/2 = 2\varepsilon$. *For Ar-Ar the relative velocity is then equal to* $g = 480$ m s^{-1} *with* $kr_m = 58$. *Perpendicular to the trajectories the surfaces of constant action are indicated at intervals of 10 h, i.e. wavefronts at intervals of 10* λ.

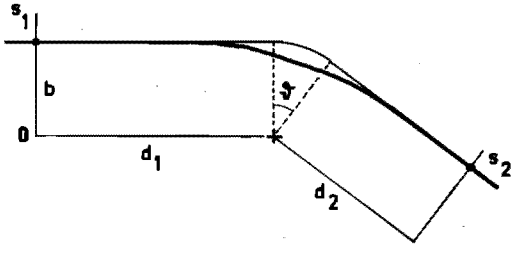

Figure 2.6. The actual particle trajectory (bold line) and the reference trajectory (thin line) of length $(d_1 + d_2 - b\theta)$, *following the convention of* θ *being negative for an attractive potential.*

in the case of small scattering angles) results in a classical phase difference $\Delta\phi(b)$ which is equal to $2\eta_l^{JB}$ (equation (2.14)) and equation (2.38) is equal to the expression for the total cross-section Q that can be derived from equation (2.10) and (2.11) in the Landau-Livshitz approximation (equation (2.16)).

At the glory trajectory, for which $\theta = 0$, we see a spherical wave front with a constant phase difference with respect to the undisturbed plane wave front. This spherical wave front will also contribute to the amplitude in forward direction. The curvature of the spherical wave front will determine the magnitude of its contribution, as it determines the effective range of contributing b values near the glory trajectory. (equation (2.20) and (2.22))

The relation of these surfaces of equal phase and the JWKB phase shifts is clarified with figure 2.6. The phase shift $2\eta_l^{JWKB}$ is the difference in phase ϕ of the actual particle trajectory in comparison with the reference trajectory indicated, consisting of two straight line trajectories at distance b and an arc $b\theta$, as given by

$$\phi(s_2) - \phi(s_1) = 2\pi \left(\frac{d_1 + d_2 - b\theta}{\lambda} \right) + 2\eta_l^{JWKB} \qquad (2.39)$$

with $\lambda = h / \mu g$ and s_2 and s_1 two positions on the actual particle trajectory as indicated in figure 2.6. With $k = 2\pi / \lambda$ and $b = (l + \frac{1}{2}) / k$ we recognise the semiclassical equivalence relation given in equation (2.13).

The picture given in this section helps us to achieve insight in the correspondence of the classical particle trajectories with the partial wave solution of quantum mechanics. For a more detailed discussion of classical mechanics and the optico-mechanical analogy the reader is referred to the excellent book of Lanczos (LAN 66).

3. Introduction to the scattering experiment

3.1. The intermolecular potential

In this discussion we limit ourselves to the spherical symmetric intermolecular potential between two neutral atoms.

At large interatomic separations the potential is in good approximation given by

$$V(r) = - C_6 / r^6 \qquad (3.1)$$

due to the induced dipole-induced dipole interaction. The constant C_6 is called the Van der Waals constant. With decreasing distance the higher order dispersion forces also have to be taken into account (induced dipole-induced quadrupole interaction, etc.), resulting in a series

$$V(r) = - C_6 / r^6 - C_8 / r^8 - C_{10} / r^{10} \qquad (3.2)$$

Theoretical values of these coefficients can be calculated with perturbation theory or by variational calculus.

The short range intermolecular forces are repulsive due to the overlap of electron clouds. Results of theoretical calculations are best described by an exponential term(or the sum of two exponential terms),as given by

$$V(r) = e^{-\alpha r} \qquad (3.3)$$

The net result of the attractive and repulsive forces is a potential with a minimum, as the example given in equation (2.6) (figure 2.1).

For a detailed discussion of the theory of the intermolecular forces and the available calculation schemes the reader is referred to

Table 3.1 Parameter values of the three "best" potentials for argon-argon

	BFW a)		MS b)		MSV III c)	
ε/k (K)	142.095		142.5		140.8	
r_m (Å)	3.7612		3.75		3.760	
C_6	1.10727		1.11976		1.1802	
C_8	0.16971325		0.171551		0.61194	
C_{10}	0.013611		0.012748		0	
	α 12.5	α	12.5	β	6.279	
	A_o 0.27783	A_o	0.29214	b_1	-0.7	
	A_1 - 4.50431	A_1	- 4.41458	b_2	1.8337	
	A_2 - 8.331215	A_2	- 7.70182	b_3	-4.5740	
	A_3 -25.2696	A_3	- 31.9293	b_4	4.3667	
	A_4 -102.0195	A_4	-136.026	x_1	1.12636	
	A_5 -113.25	A_5	-151.0	x_2	1.4	
	δ 0.01	δ	0.01			
		α'	0.04			

a) Barker et al (BAR 74)

b) Maitland et al (MAI 71)

c) Parson et al (PAR 72)

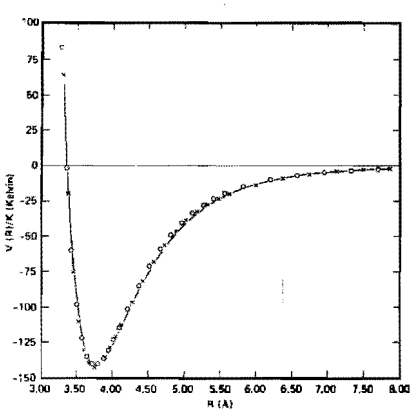

Figure 3.1. The three "best" potentials for argon-argon. Solid line, BFW potential; crosses, MS potential; open circles, MSV III potential (BAR 74).

the review book on intermolecular forces of Hirschfelder (HIR 67). A review of the recent developments in elastic scattering by Buck (BUC 74a) contains a summary of the available intermolecular potentials for the various systems studied with the molecular beam method. For the like and unlike pairs of the noble gas atoms, the determination of the intermolecular potential from experimental data and the available intermolecular potentials are extensively discussed by Barker (BAR 74).

We restrict ourselves to a discussion of the Ar-Ar potential, which is the best known pair potential. For this reason we have chosen the Ar-Ar system for the first measurements in the new time-of-flight machine.

At this moment there are three "best" potentials for argon-argon: the BFW potential of Barker, Fisher and Watts (BAR 71), the MS potential of Maitland and Smith (MAI 71) and the MSV III potential of Lee and his coworkers (PAR 72). All three potentials are flexible multiparameter functions. They have in common that they all are successive refinements of previous potentials, obtained by a successive extension of the set of experimental data to which they were fitted.

The first two potentials (BFW and MS) are based on the potential form first proposed by Barker and Pompe (BAR 68), as given by

$$V_B(r) / \varepsilon = \exp(\alpha\,(1-x)) \sum_{i=0}^{L} A_i\,(x-1)^i$$

$$- C_6/(x^6+\delta) - C_8/(x^8+\delta) - C_{10}/(x^{10}+\delta) \qquad (3.4)$$

with $x = r/r_m$, r_m the position of the minimum in the potential and ε the depth of the potential well. The choice $V(r_m) = -\varepsilon$ and $V'(r_m) = 0$ determines the parameters A_0 and A_1 in terms of the other parameters. The parameter δ is added to prevent a spurious maximum at small separations, and it has been shown that provided it is reasonably small its precise value is unimportant (BAR 68). The number of remaining free parameters is equal to $(L + 5)$. The main characteristic of this type of potential function is that they are flexible multi-parameter analytic functions with a functional form that has the

correct asymptotic behaviour at small and large distances (equation (3.2) and (3.3)) and flexibility in the intermediate range, i.e. in the potential well.

The BFW potential has the functional form given in equation (3.4), with $L = 5$. The parameter values are given in table 3.1 (BAR 74). The BFW potential is an improved version of two previous potentials of Barker and Pompe (BAR 68) and Bobetic and Barker (BOB 70), all with the same functional form. The experimental data used for the determination of the BFW potential are (BAR 74): high energy molecular beam data; the zero-temperature and -pressure lattice spacing, energy and Debeye parameter; theoretical values of C_6 , C_8 and C_{10} ; second virial coefficients; the liquid phase at one temperature and one density.

With the BFW potential a wide range of thermodynamic properties of solid, gaseous and liquid argon have been calculated, and the agreement with the experiment is excellent (BAR 71, KLE 73, FIS 72). Also the transport properties as thermal diffusion ratio and viscosities are well predicted (BAR 71a). With the BFW potential the differential cross-section has been calculated and compared with the low energy molecular beam measurements of Lee et al. (PAR 72) and Scoles et al. (CAV 70, 71), showing an excellent agreement. Moreover the BFW potential gives a good description of spectroscopic measurements of vibrational level spacings (TAN 70).

Simultaneously with the development of the BFW potential, Maitland and Smith (MAI 71) also improved the potential of Bobetic and Barker (BOB 70) to give a better fit to the measurements of vibrational level spacings (TAN 70). This improvement was obtained by adding an extra term and making slight changes in the parameter values of Bobetic and Barker, resulting in the MS potential given by

$$V_{MS}(r) = V_B(r) + \varepsilon \{\alpha' \exp(-50\ (x - 1.33)^2)\} \qquad (3.5)$$

with $V_B(r)$, x and ε the same as in equation (3.4). In table 3.1 the parameter values are given and in figure 3.1 the MS potential is compared to the BFW potential. We can observe that they are very

similar.

The third "best" potential for argon-argon is of Lee and his co-workers. Their potential is of a functional class different from the previous two. It is characterised by the use of different analytic functions for the different regions. At small and large separations again a functional form of the correct asymptotic behaviour is chosen. The specific form used is given by

$$V(r)/\varepsilon = \exp(-2\beta(x-1)) - 2\exp(-\beta(x-1)) \quad \text{for } 0 < x \leq x_1$$

$$= b_1 + (x - x_1)\{b_2 + (x - x_2)(b_3 + (x - x_1)b_4)\}$$

$$\text{for } x_1 \leq x \leq x_2$$

$$= -C_6/x^6 - C_8/x^8 - C_{10}/x^{10} \quad \text{for } x_2 \leq x \qquad (3.6)$$

with $x = r/r_m$ and ε and r_m the depth and position of the potential well respectively.

Their first potential MSV I (Morse-Spline-Van der Waals) was derived by using only their differential cross-section measurements and the theoretical values of C_6 , C_8 and C_{10} . As this potential gave a poor fit of second virial coefficients, Lee et al derived improved potentials MSV II and MSV III, by successively extending the set of experimental data with second virial coefficients (resulting in the use of a larger theoretical estimate of C_8) (MSV II) and vibrational level spacings (MSV III).

In table 3.1 we give the values of the parameters in equation (3.6) for the MSV III potential. In figure 3.1 the MSV III potential is compared with the two other best potentials. The MSV III potential gives a good agreement with solid state data (GIB 73) and gas viscosities (PAR 72).

At this moment it is difficult to give preference to one or the other potential. Only one field of experimental information seems to prefer the BFW (and the MS) potential, i.e. the measurements of the velocity dependence of the total cross-section of Bredewout (BRE 73)

and the absolute value of the total cross-section of Swedenburg et al. (SWE 70), as pointed out by Bredewout (BRE 73). In chapter 7 this will be discussed in more detail, together with the presentation of our experimental results.

Although small differences are still existent, we can observe in figure 3.1 and table 3.1 the excellent agreement of all three "best" potentials for argon-argon. The difference with the traditional Lennard-Jones potential for argon-argon (MIC 49) with ε = 119.8 K and r_m = 3.81 Å is noteworthy.

3.2. Measurement of total cross-sections

In figure 3.2 a schematic view of an ideal total cross-section measurement is given. A monoenergetic primary beam with velocity v_1 is crossed by a monoenergetic secondary beam with velocity v_2. The angular resolution is infinitely high and the contribution of the scattered molecules to the signal at the detector is negligible. The opening angle of the secondary beam is negligible and thus the relative velocity g is also monoenergetic.

The number of scattering events $\dot{M}(m^{-3}\ s^{-1})$ per unit of volume per time unit in the scattering center is given by

$$\dot{M} = n_1\, n_2\, g\, Q \qquad (3.7)$$

with n_1 and n_2 the number densities of the primary and secondary beam particles in the scattering center, Q the total cross-section and g the relative velocity. Equation (3.7) is independent of the coordinate system (*L* versus *CM*) as n_1, n_2 and g are invariant to this coordinate transformation.

Transformation of equation (3.7) to laboratory variables results in

$$I(v_1) = I_o(v_1)\ \exp-\ (g\, J_2\, l\, Q / v_1\, v_2) = I_o(v_1)\ \exp-\ \xi Q \qquad (3.8)$$

with ξ defined by this equation as $\xi = g\, J_2\, l\, /\, v_1\, v_2$, with $I_o(v_1)$ (s^{-1}) and $I(v_1)(s^{-1})$ the unattenuated and the attenuated primary beam signal at the detector respectively, $J_2(m^{-2}\ s^{-1})$

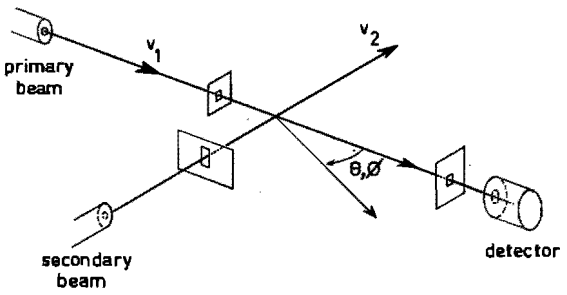

Figure 3.2. Schematic view of an ideal total cross-section measurement.

the secondary beam flux at the scattering center and l the length of the intersection of the two beams, as measured along the primary beam. By alternately measuring $I_o(v_1)$ and $I(v_1)$ for a range of primary beam velocities, we obtain the attenuation ξQ as a function of v_1 . By multiplying the attenuation ξQ with v_1/g and keeping $J_2 l/v_2$ constant, we get a relative measurement of $Q(g)$ as a function of g .

The actual experiment will differ in two respects from this ideal situation. In the first place the angular resolution of the apparatus is finite and molecules scattered over a small angle still reach the detector. Their contribution to the signal at the detector can not be neglected. This effect has already been discussed in section 2.3. The resulting correction that has to be applied to the measured value of the total cross-section is discussed in section 7.1.

Secondly all beam quantities have a certain distribution around their nominal value. As a result we measure a value of Q averaged over a small g-region. The resulting effect on Q is discussed in section 7.2.

To obtain a narrow distribution of secondary beam velocities we use a high intensity supersonic secondary beam, collimated to a small opening angle (section 5.1.3. and 6.5.),

To obtain a narrow distribution of primary beam velocities, we use the time-of-flight method (chapter 4).

In the field of total cross-sections most measurements have been done by using a mechanical velocity selector for the primary beam, measuring the attenuation at all velocities v_1 in succession. The demands on the stability of the scattering center, i.e. the product $J_2 l/v_2$, and the apparatus are very high.

To eliminate drift of the apparatus and to improve accuracy, Von Busch (BUS 67) measured alternately at two velocities, by splitting the primary beam emerging from the source slit and using two velocity selectors. Both beams pass through the same scattering center (a scattering box in this case) and are detected by the same detector. The time between measurements with one beam at the desired velocity v_1 and the other beam with the reference velocity v_{ref} is of the order of a few seconds to several tens of seconds, a considerable decrease compared to the case of measurements with a single velocity selector.

As an alternative we use the time-of-flight method. A short burst of molecules is periodically transmitted by a fast rotating chopper disc with a narrow slit. The period between two succeeding bursts is divided into many short time channels. All particles travel the flight path from the chopper disc to the detector. At the detector single particles are detected and counted in the time channel corresponding to their time of arrival. During many periods this procedure is repeated and the total count is accumulated in each time channel. With the time-of-flight method we measure at all velocities in the velocity distribution of the primary beam during each period, eliminating errors due to density fluctuations of the scattering center on a time scale of milliseconds. Particles with different velocities all travel exactly the same flight path, thus encountering exactly the same experimental conditions. The first measurements of this type have been done by Lempert (LEM 70, 71).

4. Time-of-flight method

4.1. Introduction

To analyse molecular beam sources and to measure physical properties, e.g. total cross-sections, as a function of velocity we need a means to select the velocity of beam molecules. The conventional way is to use a Fizeau type slotted disc velocity selector (STE 72). As an alternative one can use a time-of-flight method, either the conventional single burst method or the cross-correlation method. The specific experimental circumstances determine which method is to be preferred.

In section 4.3. we compare both methods of measuring time-of-flight distributions.

In this introduction we compare the use of a velocity selector with the use of the single burst TOF method, in the case of measurement of a whole velocity spectrum. The transparancy ε' of a velocity selector is $\varepsilon' \leq 0.5$. To measure the background the beam has to be chopped, with a typical duty cycle of 0.5. Thus the overall duty cycle is typically 0.25. With the same total measuring time, the same velocity resolution and the same detector the signal-to-noise ratio's of both methods are comparable when at least 1/4 of the time channels of the TOF spectrum contain significant information. In this comparison the time needed for tuning the velocity selector to a different frequency, i.e. a different velocity, is not taken in account.

A major drawback of the time-of-flight method is the need of a detector with a fast response, to eliminate memory effects in the ionizer. The efficiency of a detector with a fast response is typically a factor 10^2 or 10^3 lower than what can be achieved with a slow response ionizer.

A major advantage of the time-of-flight method is the simultaneous measurement of the whole velocity spectrum. Also the change of velocity resolution and the achievement of a very high velocity

resolution is easier with the TOF method.

4.2. Calibration of a time-of-flight machine for molecular beam studies

(published by H.C.W. Beijerinck, R.G.J.M. Mooneri and N.F. Verster, J.Phys.E.: Sci.Instr. 7(1974)31).

4.2.0. Abstract

A time-of-flight machine for the velocity analysis of molecular beams is described together with an experimental investigation of systematic errors. A velocity selecting chopper is used to measure all delay times, including the delay in the beam detector due to the extraction time from the ionizer and the flight time of the ions in the quadrupole mass filter. With our ionizer no memory effects occur at emission currents smaller than 1 mA. Memory effects in the detector chamber due to the direct reflection of beam particles are eliminated by collimating the beam before the entrance and by trapping the beam in a separate volume afterwards, while obstacles inside the detector chamber are carefully avoided. The absolute calibration of the detector gives an efficiency of $1.6\ 10^{-6}$ counts/molecule for an O_2 beam of 1000 m s^{-1}. Calibrations a week apart reproduce to within 6%.

4.2.1. Introduction

For measuring the velocity distribution of a molecular beam the time-of-flight method (KOF 48 , BEC 56) can be used as an alternative for a slotted-disc velocity selector. Many papers have been published on the design (STE 72) and calibration (CAN 71) of slotted-disc velocity selectors, but little research has been done on the design (HAG 68 , ALC 69a, 69b, 70 , HAG 70) and calibration of machines using the time-of-flight method. In this paper we give a description of our time-of-flight machine and report the work we have done on calibrating

the flight-time scale and on finding and eliminating systematic errors.

One aim of our work (BEIJ 71) is the measurement of the velocity dependence of total cross-sections for elastic atom-atom scattering. These measurements can give important information on the intermolecular potential, provided that the experimental results have a rather high accuracy of the order of 0.1%. In this field most measurements have been done with a mechanical velocity selector, measuring at all velocities in succession. With the time-of-flight method molecules with different velocities travel exactly the same path, thus encountering exactly the same experimental conditions. Measurements are made at all velocities during each period, eliminating on a time scale of milliseconds errors due to density fluctuations in the scattering centre. Measurements of this type have been performed by Lempert (LEM 70, 71).

Another aim of work with our time-of-flight machine is research on different types of molecular beam sources. Information on this subject gains very much in value when absolute intensities can be measured with an accuracy of a few percent. Therefore we have determined the detector efficiency for molecular beam detection with a calibrated molecular effusion source.

4.2.2. The time-of-flight method

A short burst of particles is periodically transmitted by a rotating chopper disc with a narrow slit. The period between two succeeding bursts is divided into many short time channels. All particles travel the flight path L from the chopper disc to the detector. At the detector, single particles are detected and counted in the time channel corresponding to their time of arrival. A synchronization pulse from the chopper disc is the time zero for each period. This procedure is repeated for many periods and the total count is accumulated in each time channel.

To illustrate the time-of-flight method we use an (x,t) diagram, as shown in figure 4.1. x is the position of the particle on the beam axis and t is the time. In the diagram the path of a particle

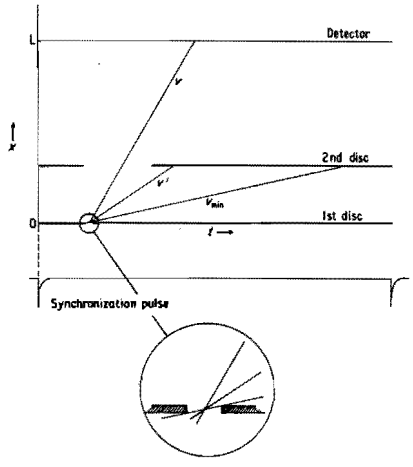

Figure 4.1. (x,t) diagram of the time-of-flight method, where x is the position of the molecule on the beam axis and t is the time.

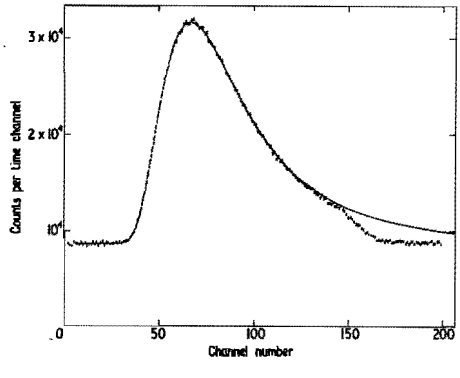

Figure 4.2. Time-of-flight spectrum of an O_2 room temperature molecular effusion source, recorded at an emission current of 1 mA. The solid line is the Maxwell-Boltzmann distribution. The error bars indicate the statistical error $N^{\frac{1}{2}}$. Period 9.27 ms; number of periods, 2 10^6.

with velocity v is a straight line with slope v. To avoid overlap of two succeeding periods, a second disc, with a broader slit, intercepts the low velocity v' particles. Particles with such low velocities that they could pass the second disc in the following period cannot in general pass the slit in the first disc because of its thickness. The lowest velocity transmitted is v_{min}. If the slit is rather wide an intermediate disc will be necessary.

The cut-off of the second disc has another important function. To retrieve the time-of-flight signal from the spectrum accumulated in the time channels, we have to subtract the background. Beyond the cut-off we can accurately determine the background simultaneously with the signal.

Figure 4.2. shows the time-of-flight spectrum of an O_2 room-temperature molecular effusion source, collimated at 1 mm diameter before entering the detector. The Knudsen number is five. The solid curve is the theoretical Maxwell-Boltzmann distribution. The error bars indicate the $N^{\frac{1}{2}}$ statistical error. Within this error the experimental data are in good agreement with theory. At the low velocity side we see a slight attenuation of the beam by the residual gas. The cut-off of the second disc can be clearly seen.

4.2.3. Description of the apparatus

4.2.3.1. Vacuum system

In the design of the apparatus more emphasis has been laid on achieving a low background pressure in the detector chamber than on developing high intensity beams. This enables us to use a large variety of low-intensity molecular beam sources.

A four-stage differentially pumped vacuum system is used, with a fifth stage as a beam trap (figure 4.3.) The last three stages are standard UHV equipment, bakeable at 400°C (BEIJ 73). The pumps used are 330 l s^{-1} oil diffusion pumps in the first two stages, a 25 l s^{-1} getter ion pump with a liquid nitrogen cryopump and a titanium sublimator in the third stage, and a 50 l s^{-1} getter ion pump with a titanium sublimator in the fourth stage, i.e. the detector chamber. The fifth stage is a 20 l s^{-1} getter ion pump. The second stage is

also connected to a circuit of a cryodistribution station (SES 72)for 20 K cryopumping of secondary beams. Flow resistances in the range 0.1 - 0.5 l s^{-1} connect the different stages. These flow resistances are 100 mm long tubes with diameters in the range 5 - 8 mm. Standard molecular beams have a diameter of 1 mm. Thus the alignment of the beam diaphragms is set apart from the alignment of the flow resistances. Both the beam collimators and the flow resistances are optically aligned with a telescope.

The total pressure in the detector chamber is less than 5 10^{-12}torr. The main components of the residual gas spectrum are located at mass number 2, 4, 18, 28, 35 and 37, which are respectively H_2, He, H_2O, N_2/CO and ^{35}Cl and ^{37}Cl. The detector chamber is only opened for maintenance, on the average less than once a year. The UHV part of the apparatus is separated from the first two stages by a pneumatically operated in-line valve which closes as soon as the pressure in the second stage rises above a preset level, i.e. 5 10^{-6}torr. The whole vacuum system is safeguarded by using standard safeguard and control modules (BEIJ 74).

4.2.3.2. Beam chopping

The source-detector distance is 186 cm. The chopper is located at 50 cm from the source so that the flight path is 136 cm. The chopper is a synchronous motor with a frequency range of 25 - 100 Hz. The diameter of the discs is 11 cm and their thickness 1 mm. The first disc has two slits of 1 mm opposite each other; the second disc has two 9 mm slits and is located 10 cm behind the first.

At 100 Hz the 1 mm slit corresponds to 30 μs. The leading edges of the slits in the first and the second disc are aligned. The thickness of the first disc prevents low velocity particles being transmitted in following periods. The effective slit width decreases slightly with increasing flight time, and the measurements are correspondingly corrected. Sharp synchronization pulses are obtained from a lamp, lens and phototransistor set at the first disc.

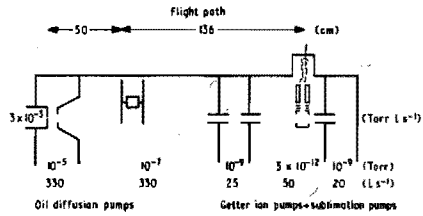

Figure 4.3. Schematic diagram of the time-of-flight apparatus.

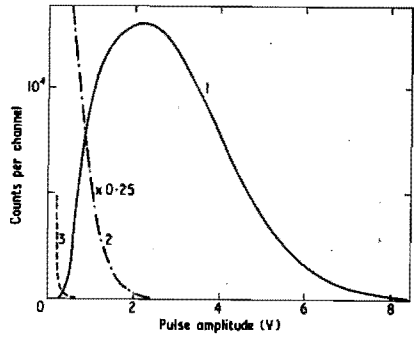

Figure 4.4. Pulse height spectra: 1, pulses due to O_2^+ ions; 2, noise pulses (photons) with the ionizer on; 3, noise pulses with the ionizer off. The energy scale is 4.1 10^{-5} V per electron at the output of the multiplier.

4.2.3.3. Particle detection

The detector is a standard quadrupole gas analyser (EAI Quad 230) fitted with a cross-beam ionizer and a Cu-Be multiplier. The length of the ionizing region is less than 8 mm.

Output pulses first pass a charge-sensitive preamplifier, mounted on the detector flange, and are then fed into a nuclear physics multiscaler. The shortest channel time is 40 μs. All measurements have been done with a maximum count rate of 1 kHz, to avoid large dead time corrections caused by the 20 μs dead time of the multiscaler. Recently the multiscaler has been replaced by a PDP-11 with a multiscaling interface with 2.5 μs as the shortest channel time and 100 ns dead time (GEE 73), but all measurements reported in this paper have been obtained with the nuclear physics multiscaler.

The pulse height spectra of pulses due to ions and noise pulses with the ionizer switched on (photons) and with the ionizer switched off are shown in figure 4.4. The discriminator in the multiscaler is adjusted to a level where noise pulses give a negligible contribution to the background of the time-of-flight spectrum. An appreciable fraction of the ion pulses also fall below this level. For this reason the total gain and the position of the discriminator level have a critical influence on the sensitivity of the detector system. We believe that changes in the gain of the Cu-Be multiplier are the main cause of the drift mentioned in 4.2.7. Improvement by a better initial discrimination between photons and ions is planned.

4.2.4. Signal at the detector

The number N of molecules leaving the source can be represented by

$$d^4 N = I(0)\, P(v)\, d^2\Omega\, dv\, dt \qquad (4.1)$$

where $I(0)$ (molecules s^{-1} sr^{-1}) is the intensity in forward direction and $P(v)$ is the normalised velocity distribution function. The collimator in front of the detector limits the solid angle to $d^2\Omega = A/l^2$ where A is the collimator area and l the source-collimator

distance. In each period the chopper is open during time t_b and transmits a burst of molecules, so that the number of molecules reaching the detector in one period becomes

$$dN(v) = I(0)\ P(v)\ (A/l^2)\ t_b\ dv \qquad (4.2)$$

Transformation of the distribution over the velocity given in formula (4.2) with $v(t_{fl}) = L/t_{fl}$ and $|\ dv| = (v^2(t_{fl})/L)\ dt_{fl}$, where L is the length of the flight path, gives the distribution over the flight time t_{fl}:

$$dN(t_{fl}) = \dot{N}\ dt_{fl} = I(0)\ P(v(t_{fl}))\ (A/l^2)\ t_b\ (v^2(t_{fl})/L)\ dt_{fl} \qquad (4.3)$$

We record the counts of detected molecules in time channels of duration t_{ch}. The number of molecules arriving at the detector during the time channel k centred at t_{fl} is $\dot{N}(t_{fl})t_{ch}$, and the recorded number of counts in this channel in each period is

$$N_k(t_{fl}) = \eta_b(v(t_{fl}))\ \dot{N}(t_{fl})\ t_{ch} \qquad (4.4)$$

where the detection efficiency $\eta_b(v)$ gives the probability that a molecule with velocity v is counted. The detector is a density detector; thus $\eta_b(v)$ is proportional to v^{-1} and is given by

$$\eta_b(v) = \eta_o\ v_o/v \quad \text{(count/molecule)} \qquad (4.5)$$

where η_o is the detection efficiency at velocity v_o. Substitution of equation (4.3) and (4.5) in (4.4) gives the full expression for the recorded number of counts in each time channel in one period:

$$N_k(t_{fl}) = \{\eta_o\ v_o\ t_{ch}\ t_b\ A/l^2\ L\}\ I(0)\ v(t_{fl})\ P\{v(t_{fl})\} \qquad (4.6)$$

where the first, bracketed part characterizes the apparatus and the rest is determined by the molecular beam source. Equation (4.6) can also be written as

$$N_k(t_{fl}) = \eta_o \, v_o \, t_{ch} \, A \quad n(t_{fl}) \tag{4.7}$$

where $n(t_{fl})$ is the density at the detector at time t_{fl} due to one burst of molecules.

In the above formulae we have ignored all convolution corrections due to the finite width of the chopper slit and the beam, the length of the ionizing region and the finite duration of the time channels. With our experimental conditions the maximum error in formula (4.6) due to this approximation used is less than 0.1% for an O_2 room-temperature molecular effusion source.

4.2.5. Calibration of the flight-time scale

The mean flight time t_{fl} and the corresponding velocity v of the molecules that are recorded in time channel k can be written as

$$t_{fl}(k) = (k - \tfrac{1}{2}) \, t_{ch} + t_o \tag{4.8}$$

$$v(k) = L/t_{fl} \tag{4.9}$$

where L is the flight path, t_{ch} the duration of one time channel and t_o the effective delay. The value of L can be measured with sufficient accuracy as the position of the ionizer and the first disc of the chopper are both well determined. The value of t_{ch} is determined with a very high accuracy by the quartz clock of the multiscaler. The effective delay t_o is the difference between the delay in the trigger action and the delay in the recording of an arriving molecule. Many effects contribute; a careful experimental measurement seems the only reliable way to determine t_o.

The contributions to t_o are (figure 4.5):

(i) the delay $t_1(T)$ from the synchronization pulse to the centre of the transmission function of the slit in the first disc for beam particles: this delay is due to the offset of the synchronization mechanism to the location of the molecular beam and is proportional to the period T of the chopper:

$$t_1(T) = c' T \tag{4.10}$$

(ii) the fixed delay t_2 from the synchronization pulse to the actual start of the first time channel. This delay is caused by the electronics of the multiscaler; t_2 is the difference between the delay in the response of the multiscaler to the synchronisation pulse and the delay in the storing of the input pulses.
(iii) The fixed delay t_3 in the detection of beam particles at the detector: this is the sum of the extraction time of the ions from the ionizer and the flight time of the ions in the quadrupole mass filter.

The effective delay time in equation (4.8) is given by

$$t_0 = - t_1(T) + t_2 - t_3 \tag{4.11}$$

One method to determine t_0 is by using a variation of the length of the flight path (DAV 73). Another method to determine the time zero of the flight-time scale is to substitute a light source for the molecular beam and to use a photomultiplier as a detector. The time channel in which the photons are detected then gives $-t_1(T) + t_2$. Delay in the detection of beam particles is not measured in this way and an estimated correction has to be made. We extended this method to measure all delay times involved by using a special configuration of chopper discs and a beam of light and a molecular beam simultaneously. The beam particles transmitted by the first disc are velocity-selected by the second disc.

An (x, t) diagram of the method is given in figure 4.5. The first disc has a single 1 mm slit; the second has two slits with a 5 mm interspace. The centres of the slit in the first disc and the first slit in the second disc are aligned. The first slit in the second

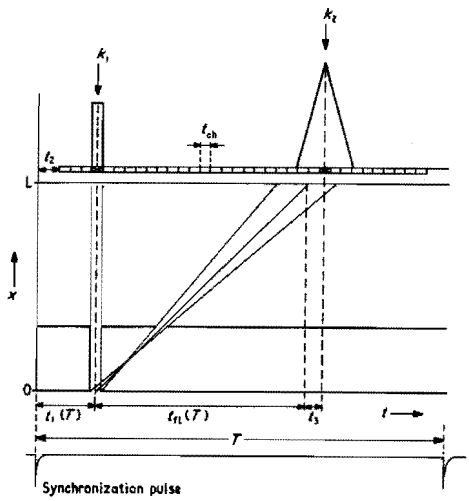

Figure 4.5. (x,t) diagram of the use of a velocity selecting chopper to determine all delay times.

disc allows the detection of photons transmitted by the first disc; this slit is slightly broader than the 1 mm slit in the first disc to prevent shielding of the transmitted photons by misalignment of the chopper motor. The second slit in the second disc is 1 mm wide and velocity-selects the beam particles transmitted by the first disc.

The time channel k_1 of the centre of the transmission function for the photons detected by the photomultiplier is given by

$$(k_1 - \tfrac{1}{2})\, t_{ch} = t_1(T) - t_2 \qquad (4.12)$$

By measuring k_1 as a function of the chopper period T we can determine c' and find t_2 by extrapolation to T=0. The time channel k_2, the centre of the transmission function for beam particles, is given by

$$(k_2 - \tfrac{1}{2})\, t_{ch} = t_{fl}(T) - t_0 \qquad (4.13)$$

where $t_{fl}(T)$ is the mean flight time of the molecules with the selected velocity. Thus

$$t_{fl}(T) = c''T \qquad (4.14)$$

where c'' is a constant depending on the configuration of the velocity-selecting chopper. By measuring k_2 as a function of the chopper period T we find $t_2 - t_3$ by extrapolation to T=0. With the value found for t_2 we can now determine t_3.

All contributions to the time offset t_0 are thus experimentally determined. For T in the range 5-20 ms and with 40 μs time channels these measurements have been performed with a room temperature O_2 molecular effusion source. The experimental results are

$$t_2 = (83 \pm 4)\ \mu s$$

$$t_3 = (29 \pm 16)\ \mu s$$

The accuracy of the t_3 measurement is limited by the small frequency range of the chopper motor. The extrapolation of $k_2(T)$ to T=0 causes an error in t_3 that is approximately ten times larger than the error in t_2. We also calculated t_3, using the dimensions of the quadrupole detector and the voltages applied, resulting in

$$t_3 = (15 \pm 1)\ \mu s$$

The agreement of the experimental value of t_3 with this calculated value is sufficient.

We also checked the value of t_2, using our PDP-11 multiscaling interface (GEE 73) with 2.5 μs time channels, giving

$$t_2 = (83.7 \pm 0.6)\ \mu s$$

In figure 4.2 the zero point of the calculated Maxwell-Boltzmann distribution is determined with the experimental value of the effective time delay t_0.

4.2.6. Systematic errors in the time-of-flight spectrum

4.2.6.1. Memory effects in the ionizer

In the ionizer we can expect memory effects due to extraction difficulties caused by space charge of the electrons. In the first

place this can show up in the delay time measurements, as described in 4.2.5. The measurements with this special configuration of chopper discs, however, contain more information. The shape of the experimentally determined particle profiles will give us extra information on the existence of memory effects. The transmission function of this combination of two slits is well known. It is triangular and symmetric around the top.

Experimentally it has been checked that in our ionizer no memory effects occur up to an electron current of 1 mA. All particle profiles follow the theoretical transmission function precisely. Above 1 mA memory effects start to show up. This is demonstrated with a time-of-flight spectrum of molecular flow from a room temperature effusive source shown in figure 4.6, recorded at the same conditions as in figure 4.2 except the electron current which was changed from 1 to

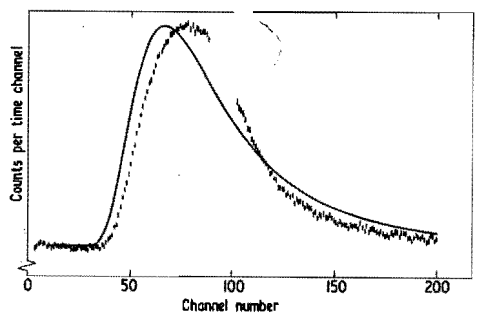

Figure 4.6. Time-of-flight spectrum of an O_2 room-temperature molecular effusion source, recorded with an emission current of 5 mA. The solid line is the Maxwell-Boltzmann distribution. Memory effects in the ionizer can be seen.

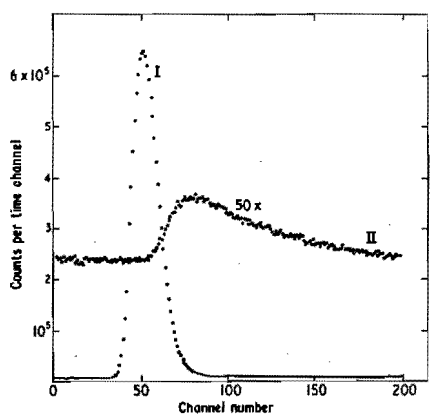

Figure 4.7. Time-of-flight spectrum of a supersonic beam collimated in the detector chamber: I, spectrum with the ionizer in the beam; II, spectrum of the background with the ionizer completely shielded from the direct beam. Memory effects due to molecules reflected from the collimator can be seen.

5 mA. It can clearly be seen that there is an extra delay of the order of 100 μs and a loss of shape of the time-of-flight distribution. The drawn curve is again the Maxwell-Boltzmann distribution, converted to time-of-flight. The memory effects are disastrous for the time-of-flight signal.

4.2.6.2. Memory effects in the detector chamber

To obtain the time-of-flight signal from the spectrum accumulated in the multiscaler we have to subtract the background. The background is due to the residual gas in the detector chamber and to noise of the electron multiplier and the amplifiers used. If the background is not constant this subtraction is not a straightforward procedure.

We can check if the noise is correlated to the synchronization pulse by accumulating a time-of-flight spectrum of the background with the detector chamber closed. We have not found any correlation as long as the chopper frequency is not in a rational relation to the mains frequency. A more serious problem stems from periodic fluctuations of the residual gas pressure at the ionizer, due to the pulsed beam entering the detector chamber. The only right way of handling the molecular beam is as follows. The beam must be collimated in a separate, differentially pumped, chamber before entering the detector chamber. The beam then passes through the detector chamber without hitting any object and is trapped in another differentially pumped chamber behind it.

If the beam is not handled in this way the effects can be seen in the time-of-flight spectrum. If the beam is trapped in the detector chamber there is a time-dependent decrease of the background beyond the cut-off of the second disc, due to reflected beam particles. This effect vanishes when the beam is trapped in a separate differentially pumped chamber. If the beam is collimated in the detector chamber, the detector can see beam particles that are first reflected from the collimator and then reflected by the wall. This has been checked experimentally with a supersonic O_2 beam. The beam is collimated in the detector chamber and the time-of-flight spectrum recorded. This is spectrum I in figure 4.7. The ionizer is then completely shielded

from the beam with the collimating device. Again a time-of-flight spectrum is recorded. This measurement is displayed enlarged as spectrum II in figure 4.7, in which a peak can be seen. The time that has elapsed between the peak in spectrum I of the direct beam and this peak in the background corresponds to the flight time of the reflected beam particles from the collimating device to the wall of the detector chamber and back again to the detector. The broadening of the peak in the background is due to the residence time distribution of the reflected particles on the surfaces and to the partial accommodation of the particles to a room-temperature velocity distribution.

The best way to check on these effects is to lift the detector completely out of the beam, and to record a time-of-flight spectrum with the beam on. This spectrum of the background will show any memory effects of this type. In our present set-up this was not possible.

4.2.7. Calibration of the detector

To calibrate our detector we used a molecular effusion source operated at large Knudsen numbers, of the order of ten. For molecular flow from this source both the velocity distribution and the angular intensity distribution are well known. Our source is a circular hole with a 1.00 mm^2 area in a 20 mm diameter wall of 50 μm thickness. The cosine distribution and the Maxwell-Boltzmann velocity distribution have been checked experimentally. The source is fed with a calibrated gas flow from a gas handling system, using a glass capillary as fixed flow resistance, together with a high pressure reservoir. By measuring the drop in pressure as a function of time we can determine the gas flow very accurately. By using a fixed flow resistance the gas flow can be reproduced very well, and there is no need for frequent recalibration.

With our calibrated source we can now determine the detector efficiency in equation (4.6). A calibration measurement for O_2 is shown in figure 4.2. The forward intensity, at 90 torr in the high pressure reservoir, is

$$I(0) = (1.45 \pm 0.03) \ 10^{16} \text{ molecules } s^{-1} \ sr^{-1}$$

The error is determined by the reproducibility of the high pressure measurement with a capsule dial gauge (Edwards CG3).

The molecular beam is collimated at 1.00 mm diameter before entering the detector. The electron current in the ionizer is 1 mA. The solid line is the theoretical Maxwell-Boltzmann distribution at 293 K. The zero point of the time scale is calculated with the experimentally determined value of t_0. Only the scale of the vertical axis is adjusted to give the best fit to the experimental data. This scaling determines $\eta_0 v_0$. The detection efficiency for an O_2 beam of velocity v_0= 1000 m s^{-1} is

$$\eta_0(O_2) = (1.60 \pm 0.06)\ 10^{-6} \quad \text{counts/molecule}$$

After initial warm-up of the equipment, during which the signal decreases, the output signal stabilizes. Repeated measurements a week apart reproduce within 6%. In a full year the efficiency has decreased by a factor two.

In the maximum of the time-of-flight distribution in figure 4.2 the density at the detector is 6 10^{-12} torr. This figure helps to illustrate the need for UHV conditions in the detector chamber. With a 1 mm diameter beam the signal-to-background ratio is of the order of 3 for O_2, and varies around this number depending on the gas used. By constructing another ionizer this figure could be improved appreciably. For residual gas the EAI cross beam ionizer has an ionizing volume approximately 25 times larger than the volume through which the 1 mm diameter beam passes. The absolute calibration of the detector system is being used for measurements on multichannel arrays and supersonic beam sources, which will both be used as secondary beams.

4.2.8. Acknowledgments

The authors would like to thank A.H.M.Habets for helpful comments on preparing the manuscript.

4.3. Comparison of the single burst and the random correlation time-of-flight method

4.3.1. Introduction

In this section we compare the statistical accuracy of the pseudo random correlation or cross-correlation TOF method with the conventional or single burst TOF method. The latter is used in the time-of-flight machine described in section 4.2. and chapter 6.

The TOF method transforms the velocity distribution of the molecular beam into a time delay distribution. The experiment is characterised by an intensity I and the normalised time delay distribution $s(t)$, with

$$\int_0^\infty s(t)\, dt = 1 \qquad (4.15)$$

and $s(t) = 0$ for $t < 0$ (causality).

In the measurement the incoming beam is modulated with a chopper function $F(t)$, which is either 1 or 0. The value 1 corresponds to beam on and the value 0 to beam off. At time t the signal $X(t)$ at the detector is given by

$$X(t) = I \int_0^\infty F(t-t')\, s(t')\, dt' \qquad (4.16)$$

Two methods can be used to retrieve the distribution $s(t)$ from the measured signal $X(t)$: the single burst method and the cross-correlation method. With the single burst method the chopper function is a delta function

$$F(t) = \delta(t) \qquad (4.17)$$

and the signal at the detector directly reflects the time delay distribution function

$$X(t) = I\ s(t) \qquad (4.18)$$

With the correlation method the chopper function is a random function

$$F(t) = \tfrac{1}{2}\,(R(t) + 1) \tag{4.19}$$

with $R(t)$ either +1 or -1. The auto correlation function of R is given by

$$\overline{R(t')\,R(t'-t)} = \lim_{T\to\infty} \frac{1}{2T} \int_{-T}^{+T} R(t')\,R(t'-t)\,dt' = \delta(t) \tag{4.20}$$

and the average value of $R(t)$ is

$$\overline{R(t)} = 0 \tag{4.21}$$

The time delay distribution $s(t)$ is retrieved from the detector signal $X(t)$ by calculating the cross-correlation function of X and R, as given by

$$C(t) = \lim_{T\to\infty} \frac{1}{2T} \int_{-T}^{+T} R(t'-t)\,X(t')\,dt' = I\,s(t) \tag{4.22}$$

The second method has the advantage of a high duty cycle of the chopper function, namely 0.5. However, not the signal but the signal-to-noise ratio is decisive for the choice which method is to be preferred.

In section 4.3.2. we specify the experimental circumstances of our comparison and introduce a suitable notation that is used in the following sections. In section 4.3.3. we discuss the conventional time-of-flight method and in section 4.3.4. we discuss the cross-correlation method. In section 4.3.5. we compare the statistical accuracy of both methods and discuss criteria for using one or the other method. In section 4.3.6. we discuss various papers that have been published on the comparison of both methods.

4.3.2. General assumptions for the comparison

To make an honest comparison we have to define our experimental circumstances very clearly.

At the detector the signal is due to counting of single particles. In the beam intensity I (counts s^{-1}) the beam geometry and the overall detection efficiency is taken into account, in $s(t)$ (s^{-1}) the velocity dependence of the detection efficiency and the length of the flight path is accounted for.

Time is measured in units of τ, and time dependent functions are characterised by an index i with $t = i\,\tau$. The width of one chopper slit is equal to τ. The chopper function is periodic and the number of slits per chopper period is equal to N. At the detector the signal is accumulated in N time channels of width τ. Concerning $s(t)$ we restrict ourselves to $s(t) = 0$ for $t \geq N\tau$, and thus no overlap of succeeding periods occurs.

The number of counts S_i in a time channel with index i, centered at $t = i\tau$, due to the transmission of one chopper slit at $t = 0$ is given by

$$S_i = \tau^2\, I\, s(i\tau) \tag{4.23}$$

which is the product of the transmitted intensity τI and the probability $\tau\, s(i\tau)$ for detection in time channel i. If b (counts s^{-1}) is the count rate due to the background (residual gas, electronic noise), the number of background counts per time channel is given by

$$B = b\,\tau \tag{4.24}$$

The chopper function F is periodic

$$F_{i+kN} = F_i \tag{4.25}$$

with k an integer.

For the single burst method the chopper function is given by

$$F_i = \delta_{i,o} \qquad i \;\; o, \ldots\ldots N-1 \qquad (4.26)$$

For the correlation method the chopper function is

$$F_i = \tfrac{1}{2}(R_i + 1) \qquad (4.27)$$

with R_i a pseudo random sequence with $R_i = +1$ or -1. A more detailed discussion is given in 4.3.4.

After measuring M periods the signal X_i in time channel i is given by

$$X_i = M \sum_{j=0}^{N-1} F_{i-j} \; S_j + MB \qquad (4.28)$$

In comparing signal-to-noise ratio's we only take into account the statistical noise $X_i^{\frac{1}{2}}$ in the number of counts per time channel. We neglect all uncertainties in the subtraction of the background from the accumulated signal.

4.3.3. The single burst method

After M periods the number of counts X_i in time channel i is found by substituting equation (4.26) in equation (4.28), resulting in

$$X_i = M S_i + M B \qquad (4.29)$$

The contents of channel i can also be written as

$$X(i\tau) = (MN\tau) \; \frac{1}{N} \; I \; \tau \; s(i\tau) + M\tau b \qquad (4.30)$$

The contribution of the beam source is equal to the product of the total measuring time $MN\tau$, the duty cycle $1/N$ of the chopper, the intensity I and the probability $\tau \; s(i\tau)$ for detection in time channel i of width τ. The contribution of the background equals the product of the measuring time $M\tau$ per time channel and the background counting

rate b.

The statistical error σ_i in the value of X_i is given by

$$\sigma_i^2 = X_i \tag{4.31}$$

and the resulting relative error η_i in MS_i, i.e. the noise-to-signal ratio, is given by

$$(\eta_i^2)_{\text{single burst}} = \frac{1}{MS_i}\left(1 + \frac{B}{S_i}\right) \tag{4.32}$$

4.3.4. The correlation time-of-flight method

A suitable periodic pseudo random sequence is a so-called maximum length sequence with $N = 2^m - 1$ elements, with $m = 0,1,2,\ldots$ This sequence has an auto correlation function given by

$$\overline{R_i\, R_{i+j}} = \frac{1}{N}\sum_{i=0}^{N-1} R_i\, R_{i+j} = \begin{cases} 1 & j = 0 \\ -1/N & j \neq 0 \end{cases} \tag{4.33}$$

and the average value of all elements is

$$\overline{R_i} = \frac{1}{N}\sum_{i=0}^{N-1} R_i = +1/N \tag{4.34}$$

The larger N is, the more the sequence R_i resembles a pure random sequence. In the paper of Stern et al. (STE 62) references are given to tabulations of maximum length sequences. General information is given by Davies (DAV 66).

After M periods the total number of counts X_i is found by substituting equation (4.27) in equation (4.28). To retrieve the function S_i we calculate the unnormalised cross-correlation function C'_i of R_j and X_j, as given by

$$C'_i = \sum_{j=0}^{N-1} R_{j-i}\; X_j \tag{4.35}$$

By substituting X_j and using equation (4.33) and (4.34) we obtain

$$C'_i = M \tfrac{1}{2}(N+1)\, S_i + MB \qquad (4.36)$$

Using equation (4.23) the correlation function can also be written as

$$C'(i\tau) = (MN\tau)\, \frac{N+1}{2N}\, I\, \tau\, s(i\tau) + M\tau b \qquad (4.37)$$

Equation (4.37) is identical to equation (4.30) with the exception that the duty cycle $1/N$ of the single burst chopper is now replaced by the duty cycle $(N+1)/2N$ of the pseudo random chopper.

The statistical error σ_i in the value of the cross-correlation function C'_i is found by using equation (4.35) and the relation $|R_i| = 1$, resulting in

$$\sigma_i^2 = \sum_{j=0}^{N-1} X_j = M\, \tfrac{1}{2}(N+1)\, N\, \overline{S} + MNB \qquad (4.38)$$

with $$\overline{S} = \frac{1}{N} \sum_{i=0}^{N-1} S_i \quad . \qquad (4.39)$$

Using equation (4.23) and (4.24) the statistical error σ_i can be written as

$$\sigma_i^2 = (MN\tau)\, (\frac{N+1}{2N}\, I + b) \qquad (4.40)$$

and one can see that σ_i is due to the background counting rate b and the fraction $(N+1)/2N$, i.e. the duty cycle of the pseudo random chopper, of the intensity of the continuous beam. With the correlation method the beam itself creates a continuous background with a corresponding noise level.

The relative error η_i is given by

$$(\eta_i^2)_{\text{correlation}} = \frac{M \tfrac{1}{2}(N+1) \quad N\,\overline{S} + MNB}{(M \tfrac{1}{2}(N+1) \quad S_i)^2} \tag{4.41}$$

With $N >> 1$ formula (4.41) reduces to

$$(\eta_i^2)_{\text{correlation}} = \frac{1}{MS_i} \left(\frac{2\overline{S}}{S_i} + \frac{4B}{NS_i} \right) \tag{4.42}$$

4.3.5. Comparison of signal-to-noise ratio's

The decision which method is superior in statistical accuracy has to be taken by comparing the relative errors of both methods. Using equation (4.32) and (4.42) one finds

$$\frac{(\eta_i^2)_{\text{single burst}}}{(\eta_i^2)_{\text{correlation}}} = \frac{S_i + B}{2\overline{S} + \frac{4}{N}B} \tag{4.43}$$

The correlation method will be superior when this ratio is larger than unity. Assuming $4/N << 1$ the two conditions where the correlation method always should be used are:

1. $S_i > 2\overline{S}$, i.e. the signal in the channels of interest is more than twice the average signal per channel;
2. $B > 2\overline{S}$, i.e. the background per channel is higher than twice the average signal per channel.

Increasing demands on the time resolution work in favor of the cross-correlation method. Both $\overline{S}$ and S_i decrease with τ^2 , while B only decreases proportional to τ , and the condition $B > 2\overline{S}$ will be sooner fulfilled.

Very narrow velocity distributions also favor the correlation method, as for most channels the conditions $S_i > 2\overline{S}$ will be fulfilled.

Considering these criteria one should be aware that $\overline{S}$ is the average signal over the whole period of N time channels (formula (4.39)). Increasing the chopper period will result in a lower value of $\overline{S}$, and will thus favor the cross-correlation method. Price and Sköld (PRI 70) mention various reasons that could lead to using a period that extends farther than the actual range of interest, i.e. the significant part of $s(t)$. Firstly, the signal $s(t)$ is in principle not zero for any positive t and may have a low velocity tail. The period then has to be extended to avoid overlap of succeeding periods. Secondly, we have to extend the period beyond the range of $s(t)$ to measure uncorrelated background.

With the single burst method we have solved both these problems by using a second chopper disc to cut-off the low velocity particles, as described in section 4.2.2. and 4.2.3.2. Directly beyond this sharp cut-off we can measure the background.

With the correlation method overlap is avoided by extending the period into the range where $s(t) = 0$. One does not loose in statistical accuracy, as the duty cycle of the pseudo random chopper is not influenced by the length of the chopper period.

A disadvantage of the correlation method is that all channels are measured with the same statistical error σ_i and thus regions where the intensity is low are measured with lower relative accuracy. Perhaps an important advantage of the correlation method is the fairly constant counting rate at the detector. Rapid fluctuations of the counting rate as encountered in the single burst method can easily influence the electronics and thus distort the shape of the TOF spectrum.

4.3.6. Discussion

The results given in the previous sections are similar to those given by Sköld (SKO 68), Price and Sköld (PRI 70) and Verster (VER 70), showing that both methods are complementary and that the specific experimental circumstances determine which method is to be preferred.

A discussion by Visser et al. (VIS 70) of a molecular beam experiment using the correlation method only mentions the increase in signal in comparison with the conventional single burst method, due to the higher duty cycle of the correlation chopper. From this fact only they conclude that the correlation method will be more efficient, i.e. give a better signal-to-noise ratio.

Hirschy and Aldrigde (HIR 71) give a comparison of the cross-correlation method with the conventional TOF method. By not specifically taking in account beam noise, their discussion is rather misleading. In fact they only demonstrate the insensitivity of the cross-correlation method for coherent noise, i.e. noise which is correlated to the trigger signal and accumulates as rapidly as the contribution due to the beam. In their paper coherent noise is created by using a chopper motor driven at the mains frequency, and a conventional TOF spectrum is compared with a cross-correlation TOF spectrum. However, coherent noise is no major problem in molecular beam TOF work and can be eliminated by using a suitable frequency to drive the chopper (see section 4.2.6.2.).

5. Molecular beam sources

5.1. General survey of beam sources

5.1.1. Introduction

In this chapter we discuss different types of beam sources. In a molecular beam experiment the important features are the center-line intensity $I(0)$ (molecules s^{-1} sr^{-1}), the flow rate $\dot{N}$ (molecules s^{-1}) and the center-line velocity distribution. To compare the performance of different types of beam sources we introduce the peaking factor κ, i.e. the ratio of the center-line intensity to the total flow rate, defined as

$$\kappa = \pi \frac{I(0)}{\dot{N}} \tag{5.1}$$

The factor π is added to normalize to $\kappa=1$ for an effusive source.

In section 5.1.2. we discuss the effusive source and give some recent experimental results for operation in the transition region.

In section 5.1.3. we discuss the supersonic beam source. This type of source is used in the scattering experiment as a secondary beam. Reseach on supersonic beams started as a secondary project in our research group to develop a reliable secondary beam source, but has grown out to be a primary project. In this section the virtual source model is introduced. Together with the peaking factor formalism it allows us to predict in an easy way the center-line intensity and the beam profile of the secondary beam.

The sections 5.2. and 5.3. concern a third type of source, where the molecular beam is formed by near molecular flow through a long channel. In general a large package of these channels is used, a

so-called multichannel array. This type of source is often used as a secondary beam source. In the scattering experiments described it has not been used, but an extensive investigation has been performed. The experimental investigation in section 5.2. concerns the so-called opaque mode where intermolecular collisions have to be taken into account. This mode is commonly used in experiments. The Monte Carlo calculations in section 5.3. concern the classical problem of free molecular flow in a cylindrical channel. This limiting case is a good reference for the description of the experimental results of a channel operated in the opaque mode. One paper has been published and one paper will be published on this research; they are reproduced as the sections 5.2. and 5.3. respectively.

5.1.2. Effusive source

The most simple type of beam source is the effusive source. It consists of an orifice with a diameter that is large compared to the wall thickness and small compared to the interior dimensions of the source chamber. The mean free path λ corresponding to the number density n inside the source is much larger than the orifice diameter $2a$. The flow rate and the peaking factor, and thus the center-line intensity, can be predicted from kinetic gas theory and are given by

$$\begin{aligned} \dot{N} &= (\tfrac{1}{2}\pi^{\frac{1}{2}})\, n\, \alpha\, A \\ \kappa &= 1 \end{aligned} \qquad (5.2)$$

with $\alpha = (2kT/m)^{\frac{1}{2}}$ the characteristic molecular velocity inside the source chamber and $A = \pi a^2$ the area of the orifice. With fixed operating conditions, i.e. a fixed ratio of the mean free path to the orifice diameter, the intensity increases proportional to the orifice diameter.

In a molecular beam experiment intensity is a crucial factor. Also the beam diameter in general is restricted, e.g. by demands of angular resolution. In many cases the condition $\lambda >> 2a$ of free molecular flow can therefore not be satisfied. For this reason the performance of an

effusive source in the onset of the transition region to continuum flow has been investigated.

With decreasing Knudsen number $Kn = \lambda/2a$ the particle flow increases with respect to the prediction given by formula (5.2). The experiments of Liepmann (LIE 60) and Stickney et al (STI 67) are sufficiently described by

$$\dot{N} = (\tfrac{1}{2}\pi^{\frac{1}{2}})\, n\, \alpha\, A\, (1 + \beta_1/Kn) \tag{5.3}$$

in the region $Kn > 1$ with the theoretical value $\beta_1 = 0.13$ of Narashima (NAR 60, 61). A model of Wahlbeck (WAH 71) describes the increase of the flow for $Kn < 1$ (WEY 72).

Also the angular distribution of the flow becomes more peaked in forward direction, resulting in an increase of the peaking factor which can be written as

$$\kappa = 1 + \beta_2/Kn \tag{5.4}$$

Experimental information on β_2 is scarce. Our experiments for O_2 give $\beta_2 = 0.20$ for $Kn \geq 1$ (UIT 75). From the center-line intensity measurements of Stickney (STI 67) one can derive a value of β_2 by correcting for the increase in particle flow with formula (5.3), resulting in $\beta_2 = 0.32$ for $Kn \geq 4$ for Cs vapor. Theoretical predictions for β_2 result in 0.28, 0.17 and 0.10 respectively if we correct the results of Morton (MOR 64), Narashima and Willis (as given by Stickney (STI 67)) in the same way as mentioned above.

For $Kn \gg 1$ the normalized velocity distribution of particles leaving the source can be calculated directly from the Maxwell-Boltzmann distribution for number density inside the source, resulting in

$$F_{MB}(v)\, dv = \frac{2}{\alpha} \left(\frac{v}{\alpha}\right)^3 \exp\left(-\left(\frac{v}{\alpha}\right)^2\right) dv \tag{5.5}$$

With decreasing Knudsen number the velocity distribution shifts to higher velocities. This shift can be described with a deformation function Γ as

$$P(v) = \Gamma(v)\, F_{MB}(v) \qquad (5.6)$$

with $P(v)$ the normalised velocity distribution of the center-line molecules. The measurements of Scott (SCO 66, 71) are described with

$$\Gamma(v) \propto 1 + \phi(v)/Kn \qquad (5.7)$$

with $\phi(v)$ calculated by Morton (MOR 64). However, this report of Morton is not readily available and $\phi(v)$ has not been published elsewhere. Our experimental investigations for O_2 (UIT 75) can be described by

$$\Gamma(v) \propto v^{\beta_3}$$

with $\beta_3 = 0.8\ Kn^{-1.4}$ for $Kn \geq 1$.

5.1.3. Supersonic beam source

If $\lambda << 2a$ many collisions occur during the flow through the nozzle and the process of beam formation has to be described as supersonic expansion into a vacuum. We will give a short description of this process.

In a small region near the nozzle, some five nozzle diameters long, the gas is accelerated to a velocity very close to its final value. When this has finished the streamlines have become straight lines, radiating from a point near the nozzle. From then on the expansion is governed by geometry: the density decreases as the inversed squared distance from the nozzle. Obviously rarefaction occurs in the direction perpendicular to the streamlines. The degree to which this perpendicular cooling communicates with the parallel velocity distribution, i.e. the distribution of the velocity component parallel to the stream lines, depends on the product of the

local collision frequency and some characteristic time of the expansion process. Continuum theory can be applied as long as this heat transfer maintains a more or less isotropic temperature. When collisions grow rare the parallel temperature freezes at its final value. The geometrical character of the expansion may then be recognized by the resulting pure geometrical cooling of the perpendicular temperature in the region where free molecular flow conditions exist.

The final flow velocity u of the gas is given by the relation

$$c_p T = \tfrac{1}{2} m u^2 + c_p T_f \qquad (5.9)$$

with c_p the specific heat per molecule at constant pressure, T the temperature of the gas inside the nozzle, m the molecular mass and T_f the final temperature of the gas after expansion. Due to the ellipsoidal final velocity distribution the term $c_p T_f$ has to be adjusted. However, for $\lambda << 2a$ the relation $T >> T_f$ holds and the final velocity u for a monatomic gas is in good approximation given by

$$u = \alpha (\gamma / (\gamma - 1))^{\frac{1}{2}} \qquad (5.10)$$

with γ the ratio of specific heats. For a diatomic gas the internal degrees of freedom freeze at an earlier stage, i.e. higher temperature, and this effects also has to be taken in account in $c_p T_f$.

The distribution of parallel velocities $v_{//}$ is characterised by

$$P(v_{//}) \propto \exp - ((v_{//} - u)/ \alpha_{//})^2 \qquad (5.11)$$

with $\alpha_{//} = (2k T_{//} / m)^{\frac{1}{2}}$ the characteristic velocity of the distribution. A commonly used parameter to specify the parallel temperature $T_{//}$ is the parallel speed ratio $S_{//} = u/ \alpha_{//}$. Simple model calculations (AND 65) lead to an expression for $S_{//}$ given by

$$S_{//} = c (2 / \gamma)^{\frac{1}{2}} (1 / Kn)^{(\gamma-1)/\gamma} \qquad (5.12)$$

with Kn the Knudsen number based on the nozzle diameter and c a numerical constant of the order of unity.

All older measurements are well described with the emperical value $c = 1.17$ (AND 65). Recent experiments for Ar (BUC 74, HAB 75) give an exponent 0.47 of the inverse Knudsen number, slightly larger than the value 0.4 predicted by equation (5.12) for $\gamma = 5/3$. The measured c-values for Ar differ from one experimental set-up to another, depending on how undisturbed the expansion is by background and skimmer. Measured values are $c = 1.04$ (HAB 75) for a cryopumped expansion, $c = 0.94$ and $c = 0.80$ (BUC 74) for two conventional diffusion pumped systems and $c = 0.76$ (MIL 69) for another diffusion pumped system. The largest measured values are in reasonable agreement with recent detailed model calculations using a realistic intermolecular potential (AND 74).

The distributions of the two velocity components perpendicular to the streamlines is given by

$$P(v_\perp) \propto \exp - (v_\perp / \alpha_\perp)^2 \qquad (5.13)$$

with $\alpha_\perp = (2kT_\perp / m)^{\frac{1}{2}}$. Unlike $\alpha_{//}$ the value of $\alpha_\perp$, and thus $T_\perp$, keeps changing throughout the free molecular part of the expansion. If collisions may be neglected altogether the relations $\alpha_\perp \sim x^{-1}$ and $T_\perp \sim x^{-2}$ hold, with x the distance to the nozzle. Insight can be achieved by considering the virtual source model as introduced by Habets et al. (HAB 74). From the free molecular region of the expansion the particle trajectories are prolonged backwards to find a virtual source from which they radiate along straight lines. As in optics, the characteristic property of such a source is that the intensity as a function of the angle is not correlated with the position. In the paraxial approximation this implies isotropic radiation. The virtual source lies in a plane very close to the nozzle. If we use the perpendicular velocity distribution as given in formula (5.13) the intensity distribution of the virtual source is gaussian, and given by

$$i(r) \propto \exp - (r / R)^2 \qquad (5.14)$$

with r the polar coordinate in the virtual source plane and $R = \alpha_1(x)\, x/u$ the characteristic radius of the virtual source. The virtual source radius has been determined experimentally by Habets (HAB 74) as a function of the nozzle pressure. A typical value of R is one nozzle diameter.

We now consider the flow rate and the centre-line intensity. The flow rate is given by (ZIE 62)

$$\dot{N} = f(\gamma)\ n\, \alpha\, A \qquad (5.15)$$

with $f(\gamma) = (\tfrac{1}{2}\gamma)^{\frac{1}{2}}\ (\tfrac{1}{2}(\gamma+1))^{-(\gamma+1)/2(\gamma-1)}$

For a monatomic gas $f(5/3) = 0.51$ and for a diatomic gas $f(7/5) = 0.48$. The peaking factor is also dependent on γ . Calculated values are (OWE 52, SHE 63, SHE 66)

$$\kappa = 1.97 \qquad \gamma = 5/3 \qquad (5.16)$$

$$\kappa = 1.26 \qquad \gamma = 7/5$$

The value $\kappa = 1.97$ gives a good description for beam measurements on argon (HAB 74).

Without any skimmer the center-line intensity $I(0)_\infty$ is directly given by formula (5.1) and (5.15) resulting in

$$I(0)_\infty = \kappa \frac{f(\gamma)\ n\, \alpha\, A}{\pi} \qquad (5.17)$$

When using a skimmer, part of the virtual source is shielded. For example, in the case of a circular skimmer of diameter $2r_s$ at a distance x_s from the nozzle, the center-line intensity $I(0)_s$ is given by

$$I(0)_s = I(0)_\infty\ (1 - \exp(-(qr_s/R)^2)) \qquad (5.18)$$

with q a geometrical correction factor equal to $q = x/(x-x_s)$, with x the distance from the nozzle (in all practical cases q is equal to

unity.

The beam profile beyond the skimmer is determined in the same way, by calculating for each position which part of the virtual source can be seen. This calculation depends only on the skimmer geometry and the intensity distribution of the virtual source.

5.2. Velocity distribution and angular distribution of molecular beams from multichannel arrays

(published by H.C.W. Beijerinck, and N.F. Verster, J.Appl. Phys. 46(1975)2083.

5.2.0. Abstract

Three stainless-steel multichannel arrays with channels of 16, 50 and 140 μm diameter have been investigated experimentally. The whole flow pattern is measured, including the angular dependence of the velocity distribution. All measurements concern the opaque mode, with $\lambda \leq L$ and $\lambda \geq a$, where λ is the mean free path in the source and a and L are the radius and length of the channel, respectively. The results are compared with the predictions for free molecular flow in the same channel, as a function of the reduced source density $n^* = L/\lambda$. The peaking factor is 30% lower than predicted by the Giordmaine-Wang model. At angles Θ larger than the half-width-half-maximum $\Theta_{\frac{1}{2}}$ the angular distribution is not perturbed by the opaque conditions; for $\Theta < \Theta_{\frac{1}{2}}$ it levels off to a lower peaking factor due to operation in the opaque mode. The center-line beam shows an increasing loss of slow molecules for increasing n^*. At $n^* = 10$ the gain in mean translational energy is 15%, much larger than predicted by the model of Olander. The deformation of the velocity distribution decreases with increasing angle, and for $\Theta > \Theta_{\frac{1}{2}}$ the molecules again have an unperturbed Maxwell-Boltzmann distribution.

5.2.1. Introduction

In molecular beam experiments, intensity is often the crucial factor. The intensity is, in general, limited by the maximum permissible flow rate. Multichannel arrays, densely packed arrays of many small bore channels with a large length-to-diameter ratio, are molecular beam sources which can give a large ratio of center-line intensity to total flow rate. In molecular beam scattering experiments, they are often used as a secondary beam source. An accurate knowledge of the angular distribution and the velocity distribution is essential for evaluating the scattering data (BER 62 , ANG 72).

In the last decade, several papers have been published on theory (GIO 60 ,IVA 63, ZUG 66, OLA 70) and experiments (GUN 57, HAN 60, BEC 61, NAU 63, JOH 66, JON 69, OLA 69, LUC 73) on the center-line intensity and beam profiles. Only very few measurements of the center-line velocity distribution are available (OLA 70a, SIE 70, WIL 72). The velocity distribution off the center-line has not been investigated at all.

In this paper we present a complete set of measurements on three multichannel arrays. The whole flow pattern has been investigated, including the angular dependence of the velocity distribution.

We will review the existing theory, and introduce suitable dimensionless quantities that allow us to predict in an easy way the theoretical performance of multichannel arrays.

5.2.2. Flow description

The flow from a multichannel source is given by

$$d^3\dot{N} = I(\theta)\, P_\theta(v)\, d^2\Omega\, dv \qquad (5.2.1)$$

where $I(\theta)$ (molecules s^{-1} sr^{-1}) is the intensity in the direction with an angle θ with the normal to the surface of the multichannel array and $P_\theta(v)$ is the normalized velocity distribution of molecules travelling in this direction.

Thus

$$\int_0^\infty P_\Theta(v)\, dv = 1 \qquad (5.2.2)$$

$$\int_{2\pi} I(\Theta)\, d^2\Omega = \dot{N} \qquad (5.2.3)$$

where $\dot{N}$(molecules s^{-1}) is the total flow rate. In order to compare arrays under different operating conditions, it is useful to normalize the center-line intensity with the flow rate. This is done by introducing the peaking factor κ , given by

$$\kappa = \pi \frac{I(0)}{\dot{N}} \qquad (5.2.4)$$

The factor π is added so that $\kappa = 1$ for an effusive source or cosine emitter, i.e. free molecular flow from an ideal thin-walled orifice.

The intensity in a direction Θ is now written

$$d^2\dot{N} = I(\Theta)\, d^2\Omega = (\dot{N}/\pi)\, \kappa\, f(\Theta)\, d^2\Omega \qquad (5.2.5)$$

with the angular profile $f(\Theta) = I(\Theta) / I(0)$. The function $\kappa f(\Theta)$ is the angular distribution function. Integration over the solid angle gives

$$\int_{2\pi} \kappa\, f(\Theta)\, d^2\Omega = \pi \qquad (5.2.6)$$

The velocity distribution in this direction is described with a deformation function $\Gamma_\Theta(v)$ defined as

$$\Gamma_\Theta(v) = P_\Theta(v) / F(v) \qquad (5.2.7)$$

where $F(v)$ is the normalized Maxwell-Boltzmann distribution of particle flux given by

$$F(v)\,dv = (2/\alpha)\,(v/\alpha)^3 \exp(-(v/\alpha)^2)\,dv \qquad (5.2.8)$$

$$\int_0^\infty F(v)\,dv = 1$$

with $\alpha = (2kT/m)^{\frac{1}{2}}$, T the source temperature, and m the molecular mass. This is the distribution of a flux of molecules in thermal equilibrium; the distribution of the corresponding density has the usual preexponential factor v^2.

Formula (5.2.1) is now written

$$d^3\dot{N} = (\dot{N}/\pi)\,\kappa\, f(\Theta)\, d^2\Omega\, \Gamma_\Theta(v)\, F(v)\, dv \qquad (5.2.9)$$

We describe all our measurements in terms of the peaking factor κ , the angular distribution function $\kappa f(\Theta)$, and the deformation function $\Gamma_\Theta(v)$. We prefer to use the angular distribution function $\kappa f(\Theta)$ which has a normalized integral, instead of the angular profile $f(\Theta)$ which is normalized by the condition $f(0) = 1$.

5.2.3. Theory

We consider a single channel with length L and radius a , operated at a number density n in the source chamber to which the channel is connected. The mean free path λ, corresponding to the density n, is given by

$$\lambda = (2^{\frac{1}{2}}\,\pi\, n\, \sigma^2)^{-1} \qquad (5.2.10)$$

with σ the molecular diameter ($\sigma = 3.5$ Å for O_2). In the flow through a channel we can distinguish different modes. In the transparent mode $\lambda >> L$ and $\lambda >> a$, and the flow is free molecular, i.e. only wall collisions occur.

In the opaque mode $\lambda > a$ still holds, but $\lambda \leq L$. The effect of intermolecular collisions now has to be taken in account. In most experiments this second mode of operation is used. Our measurements

also concern the opaque mode. Throughout our paper, we compare the measured flow properties as flow rate, center-line intensity, angular distribution, and velocity distribution with the theoretical predictions for the same channel in the transparent mode. For this reason, both the opaque channel and the transparent channel are treated in this paper.

In the third mode of operation $\lambda << a$ and $\lambda << L$, and we obtain continuum flow through the channel. In this paper, this mode is not treated.

5.2.3.1. Transparent channel

In this mode only wall collisions occur. Center-line molecules can travel through the channel without suffering any collisions, and the center-line intensity $I(0)_{\text{transp}}$ is equal to that of a cosine emitter with the same radius,

$$I(0)_{\text{transp}} = n\,\bar{v}(\pi\,a^2)\,/\,4\pi \qquad (5.2.11)$$

with $\bar{v} = 2a/\pi^{\frac{1}{2}}$, the mean molecular velocity in the source. In comparison with a cosine emitter the total flow rate is reduced by the flow resistance of the channel, expressed by a dimensionless quantity W

$$\dot{N}_{\text{transp}} = \tfrac{1}{4}\,W\,n\,\bar{v}(\pi a^2) \qquad (5.2.12)$$

with W the transmission probability or Clausing factor (CLA 29).

The factor W depends only on the geometry of the channel, for circular channels only on the ratio a/L. In the limit of long channels the transmission probability is given by $W = 8a/3L$, for all a/L ratios a good approximation is

$$W = (8a/3L)\,(1 + 8a/3L)^{-1} \qquad (5.2.13)$$

According to formula (5.2.4) the peaking factor of a transparent channel is

$$\kappa = W^{-1} \tag{5.2.14}$$

The normalized velocity distribution of molecules leaving the source in direction Θ is given by the Maxwell-Boltzmann distribution $F(v)$, the same as for a cosine emitter.

Before we discuss the angular distribution we have to introduce the wall collision rate ν, i.e. the number of molecules striking the wall per unit area per second. Because only wall collisions occur this quantity determines the flow pattern. In equilibrium conditions the relation between number density and wall collision rate is

$$\nu = \tfrac{1}{4} n \bar{v} \tag{5.2.15}$$

Assuming diffuse reflection of molecules leaving the wall, the intensity $I(\Theta)$ can be directly calculated (CLA 30) when the collision rate ν on the entrance opening and the collision rate $\nu(z)$ on the wall of the channel are known. z is the position along the length of the channel, with $z = 0$ at the exit. The wall collision rate $\nu(z)$ is determined by an integral equation, of which no exact analytical solution is available. For long channels a good approximation is (OLA 70, HEL 67a, 67b, BEIJ 75)

$$\nu(z) / \nu = (1 - W)z/L + \tfrac{1}{2}W \tag{5.2.16}$$

with W the Clausing factor.

Using this approximation the angular distribution function for $\Theta > \arctan(2a/L)$ is given by (OLA 70, CLA 30)

$$\kappa f(\Theta) = \frac{\pi I(\Theta)}{\dot{N}} = \frac{1}{\pi} \frac{\cos^2\Theta}{\sin\Theta} \frac{8a/3L}{W} (1 - W) + \frac{\cos\Theta}{2} \tag{5.2.17}$$

where for the flow rate the exact expression $\dot{N} = W\, v(\pi a^2)$ is used. For long channels this angular distribution is nearly independent of the ratio a/L.

For $0 < \Theta < \arctan(2a/L)$ the angular distribution function is

$$\kappa\, f(\Theta) = (2\cos\Theta/\pi W)\,\{(1 - \tfrac{1}{2}W)\,R(p) + \frac{2}{3}(1 - W) \times (1 - (1 - p^2)^{3/2})\,p^{-1}\} + \tfrac{1}{2}\cos\Theta \qquad (5.2.18)$$

with $p = (L/2a)\tan\Theta$ and $R(p) = \arccos p - p(1 - p^2)^{\frac{1}{2}}$. For $\Theta = 0$ we have $\kappa\, f(0) = W^{-1}$.

Due to the fact that formula (5.2.16) is only an approximation, the angular distribution defined by formulas (5.2.17) and (5.2.18) does not completely satisfy the integral normalization given by formula (5.2.6). At $L/a = 4$ the deviation is 2.1%, at $L/a = 10$ it is 0.8%, and with increasing L/a we see a further decrease of the deviation. In figure 5.2.1 we show $\kappa\, f(\Theta)$ for channels with $L/a = 4$ and $L/a = 40$ as calculated with a Monte Carlo method (BEIJ 75).

In table 5.2.1 these Monte Carlo results are listed, together with the angular distributions calculated with formulas (5.2.17) and (5.2.18). We see that the results of formulas (5.2.17) and (5.2.18) are a good approximation of the Monte Carlo angular distributions.

We can understand these results in a more direct way if we consider the optical analog of free molecular flow. Walls are ideal diffuse reflecting surfaces, and the wall collision rate is equal to the emittance (energy per unit area per second).

The intensity in a direction Θ is equal to the amount of light we see when looking into the channel from this direction. Normalizing the intensity of two channels (with the same radius) of length L_1 and L_2 to the same flow rate means normalizing the source collision rate to W_1^{-1} and W_2^{-1}, respectively, if W_1 and W_2 are the transmission probabilities of the channels. Looking into the channel at angles $\Theta > \max(\arctan(2a/L_i))$ we see the same exit collision rate $v(0)$ and a wall collision rate gradient

Table 5.2.1 The angular distribution function $k\ f(\Theta)$ of free molecular flow through a cylindrical channel, calculated with a Monte Carlo method for $L/a = 4$ and $L/a = 40$, in comparison with the angular distribution function calculated with formulae (5.2.17) and (5.2.18).

	$L/a = 4$		$L/a = 40$	
Θ	Monte Carlo a)	Formulae (5.2.17) and (5.2.18)	Monte Carlo a, b)	Formulae (5.2.17) and (5.2.18)
0	2.80	2.80	16.75	16.75
10	2.15	2.15	2.42	2.36
30	1.00	1.01	0.941	0.934
45	0.606	0.624	0.579	0.590
60	0.343	0.360	0.327	0.347
75	0.145	0.156	0.138	0.153

a) (BEIJ 75); b) for the channel with $L/a = 40$ the Monte Carlo value $W = 0.0597$ has been used, instead of the Clausing value $W = 0.0613$, (BEIJ 75).

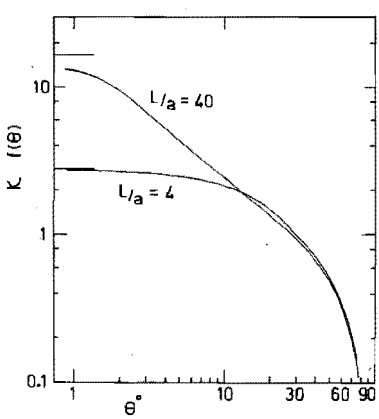

Figure 5.2.1. The angular distribution function $\kappa f(\Theta)$ for free molecular flow through a cylindrical channel, calculated with a Monte Carlo method for L/a=4 and L/a=40. The horizontal lines indicate the value κ of the distribution function for $\Theta = 0^{o}$.

$$\frac{d\nu(z)}{dz} = \frac{1 - W}{WL} \qquad (5.2.19)$$

which is nearly independent of the ratio L/a for long channels. Thus for these angles we can hardly distinguish the two channels by their flow pattern, i.e. the amount of light we see.

5.2.3.2. Opaque channel

We now consider a channel operated in the opaque mode, with $\lambda \leq L$ and $\lambda > a$. Free molecular flow ceases and we have to take into account the effect of gas-phase collisions on the flow pattern. Insight can be achieved by considering the random walk of the individual molecules in the channel in the transparent mode. Per collision with the wall of the channel the average displacement along the axis is equal to the radius a with a corresponding average path length of $2a$ (CLA 28). The average number of wall collisions of a molecule is L/a (CLA 28). In the opaque mode an estimate for the average number of gas-phase collisions is $2L/\lambda$. Thus, for long channels there is a large range where the average number of gas-phase collisions is much less than the average number of wall collisions, and where the random walk of the molecules will still be governed mainly by wall collisions. It is reasonable to assume that in first order the wall collision rate distribution $\nu(z)/\nu$ and the total flow $\dot{N}$ are undisturbed by the transition from transparent to opaque operating conditions.

At large angles Θ the angular distribution is still only determined by the wall collision rate and will be the same as in the transparent mode. We call these molecules type I. When looking into the channel with decreasing angle Θ we will gradually start to see type II molecules that are scattered into this direction by gas-phase collisions and the contribution of the walls far in the channel will become increasingly attenuated.

In the forward direction the walls do not contribute. When λ is small enough the contribution of type III molecules travelling straight through the channel from the source to the exit will diminish, and we only see type II molecules that are scattered in the forward

direction by gas-phase collisions inside the channel.

Before we consider the center-line intensity, we introduce the reduced source density n^* defined as

$$n^* = n/n_0 = L/\lambda \tag{5.2.20}$$

where n_0 is a reference source density at which the mean free path is equal to the length L of the channel.

Thus

$$n_0 = (2^{\frac{1}{2}} L \pi \sigma^2)^{-1} \tag{5.2.21}$$

The reduced source density n^* is the inverse Knudsen number based on the length of the channel and is a measure of the opaqueness of the channel. Using n^* will simplify the formula in this section

We first discuss a simple model of Hanes (HAN 60). Assuming a linear number density gradient n/L from the source density n at $z = L$ to a zero exit density at $z = 0$, we determine the point $z = L'$ where $\lambda\,(n(L')) = L'$. This results in $L' = Ln^{*\,-\frac{1}{2}}$ and the density at $z = L'$ is

$$n(L') = n\, n^{*\,-\frac{1}{2}} \tag{5.2.22}$$

We now make the simplifying assumption that the center-line beam is emitted from this surface and no further attenuation occurs. Thus this surface at L' is the equivalent of the entrance opening of a channel in the transparent mode. By substituting formula (5.2.22) in formula (5.2.11) we calculate the center-line intensity

$$I(0)_{\text{opaque}} = I(0)_{\text{transp}}\, n^{*\,-\frac{1}{2}} \tag{5.2.23}$$

The flow rate is unaffected by opaque conditions, and the resulting peaking factor is

$$\kappa_{\text{opaque}} = \kappa_{\text{transp}}\, n^{*\,-\frac{1}{2}} = W^{-1}\, n^{*\,-\frac{1}{2}} \tag{5.2.24}$$

Although the model is quite crude, the length L' gives an impression which part of the channel is most important for the center-line beam formation. Assuming the same number density profile and an isotropic velocity distribution of the gas in the channel, Giordmaine and Wang (GIO 60) integrate the contribution of type II molecules over the length of the channel, and add to this the contribution of type III molecules. Their result can be written as a function of n^* and is given by (GIO 60, JON 69)

$$I(0) = I(0)_{\text{transp}} \{(\tfrac{1}{2}\pi^{\frac{1}{2}})\ (\tfrac{1}{2}n^*)^{-\frac{1}{2}}\ \text{erf}((\tfrac{1}{2}n^*)^{\frac{1}{2}})\} = I(0)_{\text{transp}} A(n^*) \tag{5.2.25}$$

As $\dot{N}_{\text{opaque}} = \dot{N}_{\text{transp}}$ this results in a peaking factor

$$\kappa = W^{-1}\ A(n^*) \tag{5.2.26}$$

In the case of a very opaque channel the error function is unity and formula (5.2.25) reduces to

$$\kappa = (\tfrac{1}{2}\pi)^{\frac{1}{2}}\ W^{-1}\ n^{*\,-\frac{1}{2}} \qquad (n^* \gg 1) \tag{5.2.27}$$

which differs only by the factor $(\tfrac{1}{2}\pi)^{\frac{1}{2}}$ with the result of Hanes in formula (5.2.24).

For $n^* \ll 1$, formula (5.2.25) reduces to

$$\kappa = W^{-1} \qquad (n^* \ll 1) \tag{5.2.28}$$

which is the correct result for a channel in the transparent mode. The number density profile used by Giordmaine and Wang is wrong in assuming a zero exit density. However, their results for the center-line intensity only deviate slightly from calculations with a nonzero exit density which are discussed in detail by Olander and Kruger (OLA 70). considering this and the fact that different experiments still give results with a rather large spread, we prefer to use the simple

analytical results of the Giordmaine-Wang calculations.

To compare experimental results of different channels we introduce the reduced peaking factor κ^* given by

$$\kappa^* = \kappa/\kappa_{transp} = \kappa W \qquad (5.2.29)$$

Formula (5.2.26) then reduces to $\kappa^* = A(n^*)$ and all experimental results can be given in one plot of κ^* as a function of n^*. In the limiting case of continuum flow with $\lambda << a$, $\lambda << L$ the process at the exit must be described in terms of adiabatic expansion from a nozzle. The resulting peaking factors can be predicted from continuum flow theory (OWE 52 , SHE 63, SHE 66) and are $\kappa = 1.97$ for a monatomic gas and $\kappa = 1.26$ for a diatomic gas.

We now discuss the angular distribution for an opaque channel. A parameter that is often used to characterize the sharpness of the angular distribution is $\Theta_{\frac{1}{2}}$, the half-width at half-maximum. Monte Carlo calculations (BEIJ 75) show that $1.68(a/L)$ is a good approximation for the half-widths of long channels in the transparent mode (for $L/a > 10$ within 3%). We define a reduced half-width as

$$\Theta^*_{\frac{1}{2}} = \Theta_{\frac{1}{2}}(1.68a/L)^{-1} \qquad (5.2.30)$$

by dividing the measured half-width by the half-width of the same channel in the transparent mode. We can now give all our measurements in one plot of $\Theta^*_{\frac{1}{2}}$ as a function of n^* .

In a qualitative way we can predict the shape of the angular distribution function. For large angles Θ the distribution will be the same as in the transparent mode. For decreasing angles the distribution will level off to a lower peaking factor, as predicted by formula (5.2.25).

In the simple model of Hanes (HAN 60) this departure of the angular distribution from the prediction in the transparent mode will start at an angle $\Theta \simeq \arctan(2a/L')$, slightly larger than the half-width $\Theta_{\frac{1}{2}}$. We will compare our experimental results for $\kappa f(\Theta)$ with the calculations for a transparent channel. With an assumed number

density profile in the channel, one can also make a model calculation of the angular distribution of an opaque channel. The different calculations are discussed by Olander and Kruger (OLA 70); we suffice with the abovementioned qualitative comparison.

Finally, we discuss the behaviour of the velocity distribution. The center-line beam consists of molecules that are attenuated by gas-phase collisions. Slow molecules have a larger cross-section and during the process of beam formation in the channel they will be preferentially scattered out of the center-line beam.

By extending the model of Giordmaine and Wang with a velocity-dependent mean free path Olander (OLA 70) calculated the resulting deformation of the velocity distribution. His results show an increasing loss of slow molecules for increasing n^*. For $n^* > 10$ the deformation remains constant. We will compare our measurements with the results from his calculations.

At large angles the beam consists mainly of molecules emitted from the wall of the channel. These molecules leaving the wall are fully thermalized. Compared with the center-line molecules they have to travel a shorter distance through lower number densities near the exit of the channel and collisions that coudd cause a distortion of the velocity distribution will be rare. As in the case of the angular distribution, we expect that the gradual onset of the deformation will be at angles slightly larger than the half-width $\Theta_{\frac{1}{2}}$.

5.2.4. Experimental setup

5.2.4.1. Time-of-flight machine

All measurements have been done with our time-of-flight machine. A full description is given elsewhere (BEIJ 74a), we only give the features that are important for the evaluation of the measurements reported in this paper. A four stage differentially pumped vacuum system is used, with a fifth stage as a beam trap. The area of the multichannel array that is used as a molecular beam source is approximately 1 mm^2. At 8 mm from the source a skimmer with a 2 mm-diam. hole and a full angle of 30^o is used as a flow resistance for the differential pumping of the second stage. The skimmer is slender and

Table 5.2.2 Characteristics of the multichannel arrays

Array No.	1	2	3
Radius (μm)	8	25	70
Length (mm)	0.45	2.7	1.17
L/a	56	108	16.7
Clausing factor (calculated)	0.0446	0.0240	0.133
Transparency ε(%)	44	55	50
Number of channels (counted)	2504	180	26
Channel cross-section	irregular	circular	circular

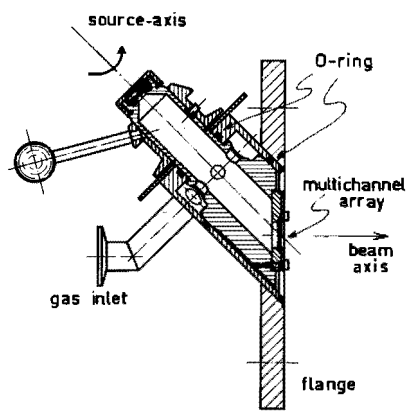

Figure 5.2.2. The rotatable source. Rotation of the inner part of the source tilts the multichannel array with respect to the beam axis, enabling us to measure the angular distribution.

long to eliminate the influence of backscattered molecules on the molecular beam.

The pressure in the first stage and second stage never exceeds 10^{-5} and 8 10^{-7} torr, respectively. The length of the second stage is 100 cm. Further stages have working pressures lower than 10^{-8} torr. Assuming an effective total cross-section of 400 Å^2 the attenuation of the beam by the residual gas is 10% at the highest flow rate measurements and typically 5% at the lower flow rates. The chopper motor is located 50 cm from the source. The first disc has two narrow slits opposite each other with an open time of 0.6%. A second disc with two broader slits cuts off low-velocity molecules to avoid overlap of two succeeding periods. The flight path is 136 cm. Before entering the detector the beam passes a 1 mm-diam. collimator. The detector is an EAI residual gas analyzer, fitted with a cross beam ionizer and a Cu-Be multiplier. Output pulses are fed into a nuclear-physics multiscaler or a PDP-11 with a multiscaling interface (GEE 73).

To measure absolute beam intensities the detector system has been calibrated for molecular beam detection, by using an effusive source (cosine emitter) at large Knudsen numbers. During a month, different calibrations reproduce to within 5%.

The experimental determination of the zero of the flight-time scale and an investigation of possible systematic errors in the time-of-flight spectrum are described by Beijerinck et al (BEIJ 74a).

The velocity resolution of the measurements reported in this paper is always better than 3%.

5.2.4.2. Rotatable source

The multichannel array is mounted in a rotatable source, shown in figure 5.2.2. The inner part of the source, on which the array is mounted, can be rotated around the source axis making an angle of 45° with the source flange. The axis of the inner part of the source and the plane in which the array is mounted also make an angle of 45°. Rotation of the inner part around the source axis tilts the array with respect to the detector direction and enables us to measure the angular distribution. The bearing of the inner part of the source is provided

by two O-rings, which also serve as a vacuum seal for the connection of the gas inlet to the inner chamber.

If β is the angle of rotation around the source axis, and $\beta = 0$ corresponds to $\theta = 0$, the relation between β and the measuring direction θ is given by

$$\cos\theta = \cos^2(\tfrac{1}{2}\beta) \qquad (5.2.31)$$

The skimmer near the source limits the measuring range to $\theta \leq 60^\circ$. The vacuum flange of the source is mounted on a thick O-ring and can be accurately adjusted to align the axis of the channel of the array with the beam axis of the TOF machine, when the source is in the neutral position. This adjustement is done at the lowest flow rate, when the angular distribution has the largest peaking factor. The accuracy in finding the direction $\theta = 0^\circ$ is 0.1°, resulting in a maximum error of 3% in the largest peaking factor.

The source is fed from a gas-handling system which delivers an adjustable and calibrated gas flow, with a 2% accuracy. The driving pressure behind the array is measured through a separate connection to the source with a Mini McLeod and a Pirani gauge, with an accuracy of 5%.

All measurements have been done at room temperature 295 K, with highly purified O_2 gas (99.95%). The flow rate has been varied from $2.6\ 10^{-4}$ to $3.5\ 10^{-3}$ torr l s^{-1}. Great care has been taken in eliminating leaks to ensure that the total gas flow actually flows through the open channels. For the measurements in this paper the not used channels are blocked by growing a copper layer on the entrance or by using an epoxy glue for this purpose.

5.2.4.3. Multichannel arrays

The arrays are fabricated from stainless steel, and are commercially available (COL).

The characteristics of the three investigated arrays are listed in table 5.2.2. The values for the radius a, the length L, and the transparency ε result from our measurements. They differ appreciably

from the values stated by the manufacturer, with a maximum deviation of 30% for the diameter of the channels of array No. 1.

All three arrays were cut through along the axis by spark erosion, and the surface on the cut was finished and examined to check the straightness of the walls of the channel. Only the walls of the long channels of array No. 2 showed a slight waviness, the channels of array Nos. 1 and 3 were quite straight.

5.2.5. Experimental results

5.2.5.1. Transmission probability

In figure 5.2.3, we have plotted the ratio ($\dot{N}_{exp}/\dot{N}_{theor}$) as a function of the reduced source density n^*, $\dot{N}_{exp}$ is the experimentally determined flow rate and $\dot{N}_{theor}$ is calculated by substituting the measured pressure in formula (5.2.12) and multiplying this result with the number of open channels. We see the transmission probability is in good approximation independent of n^*, which is to be expected if the condition $\lambda > a$ is fulfilled (CAR 63). In terms of the reduced entrance density this condition is $n^* < L/a$. For array Nos. 2 and 3 the measured flow rate is equal to the calculated flow rate, indicating a good agreement of the transmission probability with the calculated Clausing factor.

For array No. 1 the measured gas flow is 30% smaller than the theoretical prediction with the calculated Clausing factor for a cylindrical channel. One reason is the irregular cross-section of the channels which increases the number of wall collisions and decreases the transmission probability (CLA 29). We estimate that this effect accounts for at least half the deviation. The remaining part of the deviation can easily be accounted for by the error in the measured value of the radius.

Because the arrays are fabricated from stainless steel there is no ambiguity in deciding if a channel is open and contributing to the gas flow, as in the case of glass mosaic arrays (JON 69), and the exact number of open channels can be determined by counting.

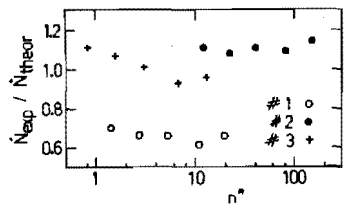

Figure 5.2.3. The ratio of the measured flow rate $\dot{N}_{exp}$ to the flow rate $\dot{N}_{theor}$ calculated with the measured source pressure, as a function of the reduced source density n^*.

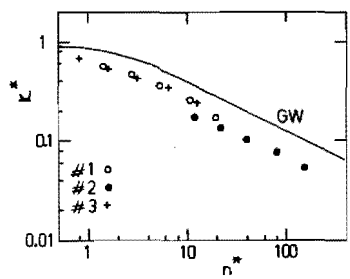

Figure 5.2.4. The reduced peaking factor κ^* as a function of the reduced source density n^*. The solid line is the theory of Giordmaine and Wang.

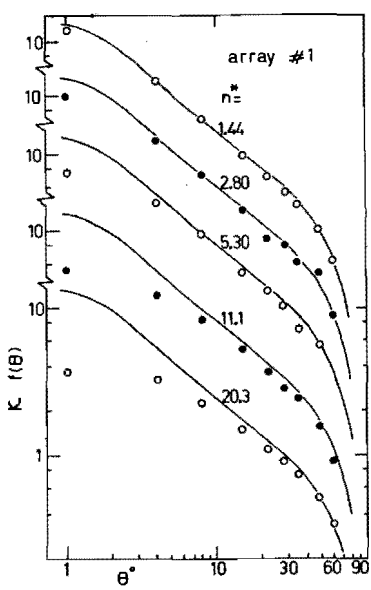

Figure 5.2.5. The angular distribution function $\kappa f(\theta)$, for different values of the reduced source density n^*. Measurements at different n^* values are shifted in vertical direction, resulting in a broken vertical scale. For comparison the solid line is the Monte Carlo angular distribution for L/a = 40 from figure 5.2.1.

5.2.5.2. Peaking factor

The peaking factor has been determined with formula (5.2.4) from separate measurements of the absolute value of the center-line intensity $I(0)$ and the flow rate $\dot{N}$.

In figure 5.2.4, we have plotted the reduced peaking factor κ^* as a function of n^*, for the three arrays. The solid line represents the theory of Giordmaine and Wang, as given by formula (5.2.26). All measurements are fairly well represented by one experimental curve, which lies 30% below the theoretical curve. Our results are in reasonable agreement with the measurements of Jones et al. (JON 69).

To predict the performance of a not investigated array we can use the experimental curve in the κ^* against n^* plot. By measuring the pressure in the source, we find κ^* in the plot. By measuring a and L of the channels of the array we can calculate the Clausing factor W and thus the actual peaking factor κ. To determine the center-line intensity $I(0)$ we need the value of the flow rate $\dot{N}$.

Calculation of $\dot{N}$ from the source pressure is rather sensitive to errors in the channel radius and depends moreover on the number of open channels, which can be very difficult to determine. We suggest, therefore, that the flow rate $\dot{N}$ be determined experimentally. An advantage of the κ^* -vs- n^* plot is that it does not depend on the number of channels.

5.2.5.3. Angular distribution

In figure 5.2.5 our measurements of the angular distribution function $\kappa f(\theta)$ for array no. 1 are shown for different values of n^*. For comparison the solid line is the Monte Carlo distribution for $L/a = 40$ from figure 5.2.1. For large angles $\theta > \theta_{\frac{1}{2}}$ there is a good agreement of the measurements with the Monte Carlo angular distribution for a long transparent channel. With decreasing angle $\theta < \theta_{\frac{1}{2}}$ the angular distribution levels off to a lower peaking factor. The measurements for arrays Nos. 2 and 3 show the same behaviour and for this reason are not given.

In figure 5.2.6, we have plotted the reduced half-widths as a function of n^*. All measured values for the three arrays coincide on

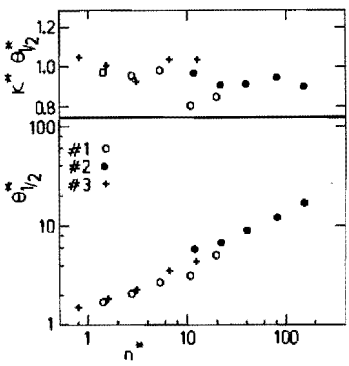

Figure 5.2.6. The reduced half-width at half-maximum $\Theta^*_{\frac{1}{2}}$ of the angular distribution function, as a function of the reduced source density n^*. In the upper part the product of the reduced peaking factor κ^* and the reduced half-width at half-maximum is given as a function of the reduced source density n^*.

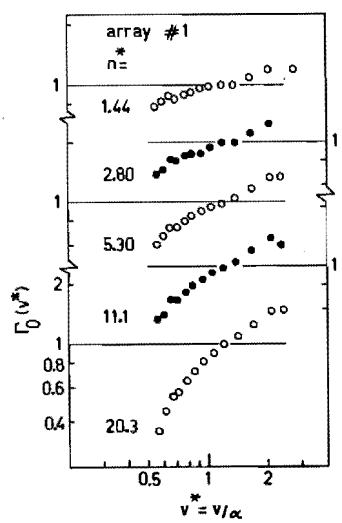

Figure 5.2.7. The deformation function $\Gamma_0(v^*)$ of the center-line beam as a function of the reduced velocity v^*, for different values of the reduced source density n^*.

one experimental curve.

The value of $\theta^*_{\frac{1}{2}}$ however contains no new information. In the upper part of figure 5.2.6 we have plotted $\kappa^* \theta^*_{\frac{1}{2}}$, the product of the reduced peaking factor and the reduced half-width. This product proves to be independent of n^* and equal to unity, which is the correct value for operation in the transparent mode.

The essential shape parameter of the angular distribution is the peaking factor which determines where the distribution starts to level off and which final value the distribution has for $\theta = 0$.

In the comparison of the measured angular dependence of the intensity of an array with results of model calculations, the use of the angular distribution function $\propto f(\theta)$ is to be preferred to the use of the angular profile $f(\theta)$. Using $f(\theta)$ has the disadvantage that, if the model predicts a wrong peaking factor, the large-angle part of the measured and calculated distribution will be scaled with a different factor. The correspondence will be poor, even if the large-angle behaviour was well predicted. In this way the comparison is only an extra test on the peaking factor. More useful information is obtained by comparing the angular distribution function.

5.2.5.4. Center-line velocity distribution

One of the first to demonstrate that the velocity distribution of atoms in the center-line beam from a multichannel source is non-Maxwellian were Hostettler and Bernstein (HOS 60). Their measurements show that both slow and fast atoms were lost, thus enriching the distribution with atoms of intermediate velocity. The source was operated at high pressures, and the loss of slow particles was attributed to clouding in front of the source. For the loss of fast particles no explanation was given. A n^* value cannot be derived from their paper.

Recent measurements on a glass capillary array by Angel and Giles (ANG 72) have been done at reduced source densities $n^* >> L/a$ and show the same behaviour, preferential loss of fast and slow atoms. They propose an energy exchange model to explain their observations. Fast atoms would catch up with slow atoms, and in these beam-beam

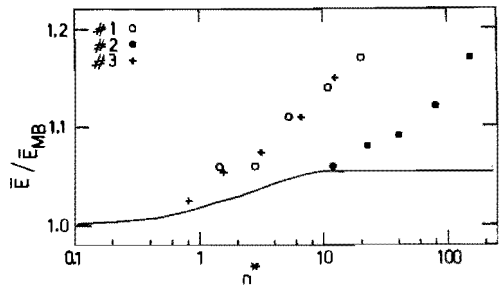

Figure 5.2.8. The ratio of the mean translational energy $\bar{E}$ of the center-line beam to the mean translational energy of a beam with a Maxwell-Boltzmann distribution, as a function of the reduced source density n^*. The solid line is the theory of Olander.

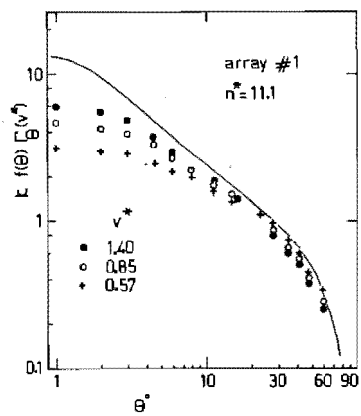

Figure 5.2.9. The differential angular distribution $\kappa f(\Theta)\Gamma_\Theta(v^*)$ as a function of the angle Θ, for different values of the reduced velocity $v^* = v/\alpha$ at a reduced source density $n^* = 11.1$. At large angles the differential angular distributions for different velocities coincide, indicating a Maxwell-Boltzmann velocity distribution.

collisions energy could be exchanged to produce an increase in the number of atoms of intermediate energy. This model is only presented qualitatively and no model calculations are undertaken. Although for the first experiment mentioned no n^* value is available, we believe that for both measurements $n^* >> L/a$ and thus $\lambda << a$, and we are in the transition region from the opaque mode to the continuum flow mode.

Experiments in the opaque mode (SIE 70, WIL 72) with $n^* < L/a$ show a different picture. Only slow particles are lost, resulting in a shift of the velocity distribution to higher velocities. Our measurements also show this behaviour. In figure 5.2.7 we have plotted the measured deformation functions $\Gamma_0(v)$ for array No. 1 at different n^* values. The deformation function is determined by comparison of the measured time-of-flight distribution with the measured distribution of an effusive source operated at large Knudsen numbers. A comparison of a time-of-flight distribution of an effusive source with the calculated Maxwell-Boltzmann distribution can be found in a previous paper (BEIJ 74a) and shows a very good agreement. To present all our data in a concise way, and to compare with other data available, we have plotted the reduced mean translational energy

$$\overline{E} \; / \; \overline{E}_{MB} = \left(\int_0^\infty v^2 \, P_0(v) \, dv \right) \left(\int_0^\infty v^2 \, F(v) \, dv \right)^{-1} \qquad (5.2.32)$$

of the center-line beam as a function of n^* in figure 5.2.8. The results for array Nos. 1 and 3 are in good mutual agreement, for array No. 2 the mean translational energy is smaller.

The data of Wilmoth (WIL 72) all indicate a much larger mean energy, the data of Olander (SIE 70) are all below our data; both their data have a large amount of scatter.

The solid line represents the theory of Olander (OLA 70a), which is in qualitative agreement with the measurements. However, none of the experiments show the feature of deformation function remaining constant beyond a certain n^* value.

5.2.5.5. Off center-line velocity distribution

We analyzed our measurements by plotting the differential angular distribution function given by

$$\kappa\, f(\Theta)\ \Gamma_{\Theta}(v)$$

as a function of the angle Θ. If $\Gamma_{\Theta}(v)$ is equal to unity, i.e. the velocity distribution is Maxwellian, the differential angular distribution is equal for all velocities and coincides with the angular distribution function $\kappa\, f(\Theta)$. In figure 5.2.9 we have plotted the differential angular distribution for array No. 1 for three different velocities at $n^{*} = 11.1$. With increasing angle Θ the differential angular distributions for different velocities converge, and coincide for angles larger that the half-width $\Theta_{\frac{1}{2}}$. Translated to deformation functions, this means that for an increasing angle the deformation function $\Gamma_{\Theta}(v)$ goes to unity and the molecules have a Maxwell-Boltzmann velocity distribution.

All our measurements show this same behaviour, we only show one typical measurement. For comparison we have drawn in the Monte Carlo angular distribution $\kappa\, f(\Theta)$ for $L/a = 40$ from figure 5.2.1.

The half-width $\Theta_{\frac{1}{2}}(v)$ of the differential angular distribution contains no new information. The product of the differential peaking factor $\kappa\, \Gamma_{0}(v)$ and the half-width $\Theta_{\frac{1}{2}}(v)$ is independent of v and is in good approximation equal to the product $\kappa\, \Theta_{\frac{1}{2}}$ of the angular distribution function.

5.2.6. Conclusions

The comparison of a channel in the opaque mode with free molecular flow through the same channel gives us a good qualitative insight in the process of beam formation. Both the angular distribution and the angular dependence of the velocity distribution show that the opaque conditions only influence the near-center-line molecules with $\Theta < \Theta_{\frac{1}{2}}$ and that the major part of the flow is undisturbed.

When using a multichannel array as a secondary beam source we have to realize that the major part of the flow rate is determined by

the large-angle distribution. In general, we can say that the angular distribution at large angles is independent of the channel dimensions and its mode of operation, and is not very different from an effusive source. To gain in comparison with an effusive source we have to collimate the beam to take advantage of the higher peaking factor.

The velocity distribution on the center-line is deformed, which results in a shift of the velocity distribution to higher velocities. One also has to be aware of the important change in the velocity distribution over the small angular range from 0 to $\Theta_{\frac{1}{2}}$ near the center-line.

5.2.7. Acknowledgments

The authors would like to thank M.P.J.M. Stevens and P. Theuws for their great help in gathering the data.

5.3. Monte Carlo calculation of molecular flow through a cylindrical channel

(H.C.W. Beijerinck, M.P.J.M. Stevens, and N.F. Verster, to be published).

5.3.0. Abstract

Molecular flow in a cylindrical channel is investigated with a Monte Carlo method by tracing the random walk of the molecules in the channel. The angular distribution of the molecules leaving the channel is calculated by using the wall collision rate as an intermediate result. The Monte Carlo wall collision rate is compared with a linear and a cubic approximation to the wall collision rate, calculated by DeMarcus and Neudachin with a variational method. For short channels the linear approximation gives a satisfactory description of the Monte Carlo results for the angular distribution, for long channels deviations of a few percent occur at small angles. Using the cubic approximation will decrease these deviations to less than one percent. The distribution of the transmitted and reflected molecules with respect to the number of wall collisions in the channel is calculated. These collision number distributions help to achieve insight in the perturbation of the flow by non-ideal conditions as adsorbing walls.

5.3.1. Introduction

The problem of molecular flow in a cylindrical channel was first investigated at the beginning of this century by Knudsen (KNU 9a, 9b) and Smoluchowski (SMO 10). Clausing (CLA 28, 29, 32) gave the first rigorous formulation of the problem and obtained an integral equation

for which he gave an approximate solution. His values for the transmission probability of a molecule entering the channel have been used ever since, and the transmission probability is often called the Clausing factor. In 1955 DeMarcus (MAR 55, 56) recalculated the transmission probability with a better approximate solution of the Clausing equation, showing that Clausing's values are a few percent high for long channels.

The advances of vacuum technology and the improved measuring techniques have revived the interest in molecular flow in the past two decades. The widespread use of molecular beams in modern physics created an interest in the angular distribution of the transmitted molecules (IVA 63, OLA 70, LIV 71, NEU 72).

We started our investigation to achieve a better understanding of the flow pattern from multichannel arrays, which are often used as molecular beam sources (JON 69, BEIJ 75a). Although these arrays are mostly operated at source densities where the mean free path is smaller than the length of the channels, the limiting case of free molecular flow is a good reference (BEIJ 75a). To solve the problem we employ a Monte Carlo method (DAV 60, SMI 66, WAR 69, 70, BER 73a, BLE 74), i.e. a simulation of molecular flow by tracing the random walk of many independent molecules. By using their history in a judicious way we calculate the angular distribution of the transmitted molecules. The accuracy of the result can be calculated on statistical grounds.

The distribution of the transmitted and reflected molecules with respect to the number of wall collisions they have suffered help us to achieve insight in the perturbation of the flow by non-ideal conditons as adsorbing walls (SMI 66).

5.3.2. Molecular flow through a cylindrical channel

In free molecular flow conditions the mean free path of the molecules is much larger than the channel dimensions and only wall collisions occur. Molecules leaving the wall are diffusively reflected according to the cosine law, without any memory of their angle of incidence. Molecules entering the channel are distributed uniformly

over the entrance surface and their angle of incidence with respect to the normal on the entrance surface is given by the cosine law.

We consider a cylindrical channel with length L and radius A. Throughout this paper all measures are given in units of the diameter $2A$. The coordinate along the axis of the channel is z, with the entrance of the channel at $z = 0$ and the exit at $z = l$, with $l = L/2A$. After a wall collision at position z a molecule will suffer the next collision with the wall at position $z + s$, with s the displacement between two successive wall collisions.

The probability distribution function $D(s)$ for a displacement s is determined by the condition of diffuse reflection at the wall and the geometry of the channel. Due to the rotational symmetry of the channel the flow pattern is fully determined by $D(s)$, which is given by

$$D(s) = 1 - \frac{|s|}{(1 + s^2)^{\frac{1}{2}}} - \frac{|s|}{2(1 + s^2)^{3/2}} \qquad (5.3.1)$$

$$\int_{-\infty}^{+\infty} D(s)\, ds = 1$$

The function $D(s)$ is derived in the Appendix (section 5.3.8). The distribution is narrow and decreases rapidly with increasing s. For $s = 0$ the function value $D(0) = 1$, for $s = 2$ the function value $D(2) = 1.6\ 10^{-2}$. For 97.5% of the molecules the condition $|s| < 2$ holds. The asymptotic behaviour for large s is given by $D(s) \simeq s^{-4}$. As we expect $D(s)$ is an even function.

The average length of a displacement is given by

$$\langle |s| \rangle = \int_{-\infty}^{+\infty} |s|\ D(s)\, ds = \tfrac{1}{2} \qquad (5.3.2)$$

The probability $P(s)$ for a displacement larger than s, which we will need further on, is given by

$$P(s) = \int_{s}^{+\infty} D(s')\, ds' = \frac{s^2 + \frac{1}{2}}{(1 + s^2)^{\frac{1}{2}}} - s \quad (s \geq 0) \qquad (5.3.3)$$

$$= 1 - P(-s) \qquad (s < 0)$$

With the distribution function $D(s)$ we now derive the integral equation for the wall collision rate, i.e. the number of molecules striking the wall of the channel per unit area per time unit. Throughout this paper we only consider the normalized wall collision rate of the channel $\nu(z)$, i.e. the wall collision rate when the collision rate on the entrance surface due to the molecules entering the channel is equal to unity. No molecules enter the channel through the exit.

To derive the integral equation we distinguish the number of molecules $\nu(z)$ striking the wall from the number of molecules $\tilde{\nu}(z)$ leaving the wall. Of course, inside the channel $\nu(z) = \tilde{\nu}(z)$. An equivalent formulation of the above mentioned conditions at the entrance and at the exit is to extend the channel at both ends with a virtual channel, with $\tilde{\nu}(z) = 1$ for $z < 0$ and $\tilde{\nu}(z) = 0$ for $z > l$.
The wall collision rate $\nu(z)$ is now given by the integral equation

$$\nu(z) = \int_{-\infty}^{+\infty} \tilde{\nu}(\zeta)\, D(\zeta - z)\, d\zeta \qquad (5.3.4a)$$

with $\tilde{\nu}(\zeta) = 1 \qquad$ for $\zeta < 0$

$\tilde{\nu}(\zeta) = \nu(\zeta) \qquad$ for $0 \leq \zeta \leq l$

$\tilde{\nu}(\zeta) = 0 \qquad$ for $\zeta > l$

The symmetry of the problem is clearly discernable. By evaluating the integral in the right hand side for $\zeta < 0$ and $\zeta > l$ equation (5.3.4a) can be written as

$$\nu(z) = P(z) + \int_{0}^{l} \nu(\zeta)\, D(\zeta - z)\, d\zeta \qquad (5.3.4b)$$

which is the usual form in which the integral equation is given. The function $P(z)$, given in equation (5.3.3), is the contribution to the wall collision rate due to the first collision of molecules entering the channel.

We now discuss some general properties of the solution $\nu(z)$ of the integral equation (5.3.4). If we reverse the conditions at the entrance and the exit, i.e. feed the channel from the other side, we get a solution $\nu'(z)$ of which we know that $\nu'(z) = \nu(l - z)$ and $\nu'(z) + \nu(z) = 1$. Thus

$$\nu(l - z) + \nu(z) = 1 \tag{5.3.5}$$

The wall collision rate can be written as

$$\nu(z) = f(z - l/2) + \tfrac{1}{2} \tag{5.3.6}$$

with f an odd function.
The kernel D of the integral equation (5.3.4) is an even function with only a narrow effective range, as we already discussed. The value of the function $\nu(z)$ is not modified by the integral operator if $\nu(z + s) + \nu(z - s) = 2\nu(z)$, i.e. the function is odd with respect to the point $(z\ ,\ \nu(z))$. Only a linear function satisfies this relation for all values of z . For long channels we expect that $\nu(z)$ is a linear function with only at the exit and the entrance deviations over a range equal to the width of D. Equation (5.3.4) shows that the value of the wall collision rate at the exit $\nu(l) > 0$. The lowest order approximation to $\nu(z)$ is a linear function from $\nu(0) = 1 - \alpha$ to $\nu(l) = \alpha$, given by

$$\nu(z) = \alpha + \left(\frac{1 - 2\alpha}{l}\right)(l - z) \tag{5.3.7}$$

where the exit collision rate α depends on the length l of the channel.

A simple approximation for the exit collision rate is given by

$$\alpha = T/2 \tag{5.3.8}$$

with T the transmission probability. In the limiting case of very short and very long channels this relation is exactly fulfilled (equation (5.3.12)).

Approximate solutions of the integral equation (5.3.4) have been calculated by different authors. DeMarcus (MAR 55,56) used a "squeezing" technique by determining upper and lower bounds for the function $\nu(z)$. DeMarcus (MAR 55,56) also used a variational method with a linear trial function f (equation (5.3.6)). Neudachin et al. (NEU 72) extended this method by using a cubic trial function. Several authors (LIV 71, SPA 63, RIC 64, HEL 67a) solved the equation by successive iteration. For short channels there is a rapid convergence. For long channels, however, many iteration steps are necessary due to the small effective range of D.

As reference solution $\nu_{ref}(z)$ for our Monte Carlo results we use the linear approximation of the wall collision rate (equation(5.3.7)) with the exit collision rate of Neudachin et al (NEU 72) and DeMarcus (MAR 55,56)

$$\alpha_{ref} = \tfrac{1}{2} - \frac{l}{3} \left\{ \frac{l^3 - 2 + (2 - l^2)(1 + l^2)^{\frac{1}{2}}}{l(1 + l^2)^{\frac{1}{2}} - \sinh^{-1} l} \right\} \qquad (5.3.9)$$

$$\lim_{l \to \infty} \alpha_{ref} = 2/3\, l$$

In figure 5.3.1 we have plotted various approximations of the exit collision rate, normalized to α_{ref}. The maximum deviation of the simple approximation of formula (5.3.8) from α_{ref} is 9% at $l = 2$. The results of Helmer (HEL 67b) are based on formula (5.3.8), by using an analytical approximation of T for short channels. Clausing's (CLA 30) results are in very good agreement with α_{ref} for $l < 0.2$.

With the normalized wall collision rate all flow parameters can be calculated. We are interested in the transmission probability of molecules entering the channel and the angular distribution of the transmitted molecules.

The transmission probability is defined as the number of transmitted molecules divided by the number of molecules entering the channel. The number of transmitted molecules can be found as the integral of $\nu(z)$ for $z \geq l$, or as the integral of $\bar{\nu}(z)$ for $z \leq l$, weighted with the escape probability $P(l - z)$ (equation(5.3.3)).

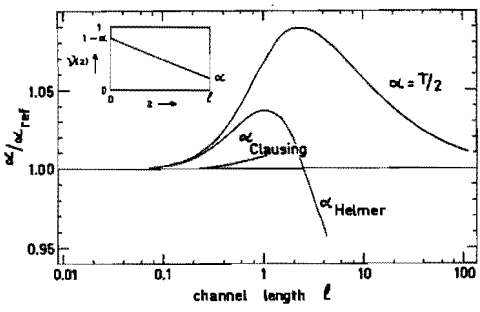

Figure 5.3.1. Various approximations of the exit collision rate α, *normalised to the reference exit collision rate* α_{ref}.

The result for T is

$$T = \frac{4}{\pi} \int_{l}^{+\infty} \nu(z)\ \pi\ dz = \frac{4}{\pi} \int_{-\infty}^{l} \vartheta(z)\ P(l - z)\ \pi\ dz \qquad (5.3.10)$$

Evaluation of the second integral of equation (5.3.10) for $z < 0$ yields

$$T = (1 - 2l(l^2 + 1)^{\frac{1}{2}} + 2l^2) + \frac{4}{\pi} \int_{0}^{l} \nu(z)\ P(l - z)\ \pi\ dz \qquad (5.3.11)$$

where the first term is the fraction of the molecules passing straight through the channel and the second term is due to molecules transmitted after a number of wall collisions. With the linear approximation for $\nu(z)$ of formula (5.3.7) and in the limiting case of large l formula (5.3.11) reduces to

$$T = \alpha + \frac{2}{3}\left(\frac{1 - 2\alpha}{l}\right) \qquad (5.3.12)$$

The first term is due to the exit collision rate, the second term is determined by the slope of the wall collision rate. It can be shown (MAR 56) that $T = 4/3\ l$ for $l \to \infty$, resulting in $\alpha = 2/3\ l$ in the limiting case of long channels.

The angular profile $f(\Theta)$ is the number of molecules leaving the channel in a direction Θ per unit of solid angle per time unit, normalized to $f(0)= 1$. Θ is the angle with the axis of the channel. The angular profile $f(\Theta)$ is given by

$$f(\Theta) = \frac{4 \sin\Theta}{\pi^2} \int_{l-(\tan\Theta)^{-1}}^{l} \tilde{\nu}(z) \{1 - ((l-z)\tan\Theta)^2\}^{\frac{1}{2}} \pi \, dz \qquad (5.3.13)$$

Integration of the contribution of molecules passing straight through the channel yields the usual formulae

$$f(\Theta) = \frac{2\cos\Theta}{\pi} \{\arccos(l\tan\Theta) - l\tan\Theta(1 - (l\tan\Theta)^2)^{\frac{1}{2}}\}$$

$$+ \frac{4\sin\Theta}{\pi^2} \int_{0}^{l} \nu(z) \{1 - ((l-z)\tan\Theta)^2\}^{\frac{1}{2}} \pi \, dz$$

$$\text{for } 0 \leq \Theta \leq \arctan(l^{-1}) \qquad (5.3.14)$$

$$f(\Theta) = \frac{4\sin\Theta}{\pi^2} \int_{l-(\tan\Theta)^{-1}}^{l} \nu(z) \{1 - ((l - z)\tan\Theta)^2\}^{\frac{1}{2}} \pi \, dz$$

$$\text{for } \arctan(l^{-1}) \leq \Theta \leq \pi/2 \qquad (5.3.15)$$

Formula (5.3.13) is derived in the Appendix (section 5.3.8.).

5.3.3. The Monte Carlo program

With the Monte Carlo method we simulate the physical process of molecular flow by tracing the random walk of many individual molecules. The trajectory of a molecule is governed by the probability distributions for starting position and starting direction. These quantities are transformed to new variables u_i that have a uniform distribution in the interval (0,1). With the usual numerical

techniques pseudo random numbers u are generated with uniform probability and assigned to the variables u_i . With the inverse transformation the starting position and direction are then determined.

The flow of the computer program is very simple. After generating a starting position and starting direction on the entrance surface we calculate the position z_1 of the first collision with the wall. If $z_1 > l$, i.e. the molecule passed straight through the channel, we start with the history of a new molecule. If $0 \leq z_1 \leq l$ we generate a starting direction in the point of collision and calculate the position z_2 of the next collision with the wall. This procedure is repeated until $z_j < 0$ or $z_j > l$ and the molecule leaves the channel. We then start with the history of a new molecule. At the end of the chapter we will discuss in some detail the calculation of the position z_1 of the first wall collision and the calculation of the displacement s between two successive wall collisions.

Along the axis the channel is divided into equal slices and the number of collisions with each slice is recorded. In this way we generate the wall collision rate $\nu(z)$. The results are discussed in section 5.3.4.

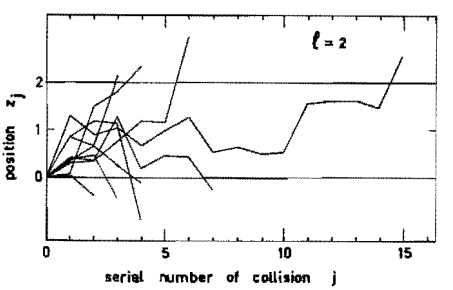

Figure 5.3.2. The random walk of a sample of 9 molecules in a channel with length $l = 2$.

Molecules leaving the channel through the exit or entrance are recorded in two arrays as a function of the number of wall collisions they have suffered. These collision number distributions are discussed in section 5.3.6.

The Monte Carlo calculations were done on a Burroughs B6700 computer, using a modified version of Algol 60. For long channels the calculation time required is determined only by the total number of wall collisions. For a channel with length l the calculation time is given by $2Nlt$, with N the sample size, $2l$ the average number of wall collisions per molecule (equation (5.3.24)) and t the calculation time per wall collision.

When running a Monte Carlo calculation for a channel with length l , with some extra bookkeeping we can simultaneously generate Monte Carlo results for a number of shorter channels contained within the channel, resulting in an important decrease of calculation times.

For demonstration purposes the Monte Carlo calculation was also programmed on a small table-top calculator (HEW). In figure 5.3.2 we have plotted the random walk of a number of molecules in a channel with $l = 2$. The horizontal scale is the serial number of the wall collision j , the vertical scale is the position z_j . Successive points (j , z_j) of one trajectory are connected by straight lines. The history of a molecule is terminated if the molecule leaves the channel on either side.

5.3.3.1. The position of first collision

The molecules entering the channel are distributed uniformly over the entrance surface. We use a polar coordinate frame (r , ϕ) centered on the axis. We choose $\phi = 0$. The normalized distribution with respect to r is given by

$$F(r)\,dr = 8r\,dr \qquad (0 \leq r \leq \tfrac{1}{2}) \qquad (5.3.16)$$

Transformation to $u_1 = 4r^2$ renders a uniform distribution in (0,1), and a starting position can be generated. From this position the molecule leaves the entrance surface. The normalized angular

distribution is given by the cosine law

$$F(\Theta, \phi)\, d\Theta\, d\phi = \frac{\cos\Theta \sin\Theta}{\pi}\, d\Theta\, d\phi \qquad (5.3.17)$$

where Θ and ϕ are polar angles with respect to the channel axis z. We transform to the variables $u_2 = \sin^2\Theta$ and $u_3 = \phi/2\pi$. The position z_1 of the first collision with the wall of the channel is determined by u_1, u_2 and u_3. One finds

$$z_1 = ((1 - u_2) / u_2)^{\frac{1}{2}}\ \tfrac{1}{2}(-u_1^{\frac{1}{2}} \cos 2\pi u_3 + (u_1 \cos^2 2\pi u_3 + 1 - u_1)^{\frac{1}{2}}) \qquad (5.3.18)$$

5.3.3.2. The displacement along the axis

After a collision with the wall at z_{j-1}, we have to generate new starting directions if the molecule did not escape. The distribution of starting directions is given by the cosine law (equation (5.3.17)) with (Θ', ϕ') polar angles with respect to the normal on the wall of the channel in the point of collision. We define $u_4 = \sin^2\Theta'$ and $u_5 = \phi'/2\pi$. The position z_j of the next collision is

$$z_j = z_{j-1} + s \qquad (5.3.19)$$

with s the displacement along the axis determined by u_4 and u_5 and equal to

$$s = \frac{2(u_4 - u_4^2)^{\frac{1}{2}} \sin 2\pi u_5}{1 - u_4 \sin^2 2\pi u_5} \qquad (5.3.20)$$

Table 5.3.1 The angular profile $f(\Theta)$ for a channel with $l = 2$. The angular profile $f(\Theta)_{MC}$ is calculated from the Monte Carlo wall collision rate ν_{MC} ($N = 3\ 10^5$), $f'(\Theta)_{MC}$ from the smoothed Monte Carlo wall collision rate and $f(\Theta)_{ref}$ from the reference wall collision rate ν_{ref}.

Θ°	$f(\Theta)_{MC}$	$\sigma(f(\Theta)_{MC})$	$f'(\Theta)_{MC}$ ($\pm$0.0001)	$f(\Theta)_{ref}$
0	1.0000		1.0000	1.0000
1	0.9776		0.9776	0.9776
2	0.9550		0.9550	0.9550
5	0.8855	0.0001	0.8856	0.8856
10	0.7667	0.0002	0.7668	0.7668
15	0.6471	0.0003	0.6471	0.6473
20	0.5316	0.0004	0.5317	0.5318
30	0.3556	0.0004	0.3558	0.3559
45	0.2165	0.0004	0.2168	0.2167
60	0.1228	0.0003	0.1230	0.1230
75	0.0519	0.0002	0.0521	0.0523

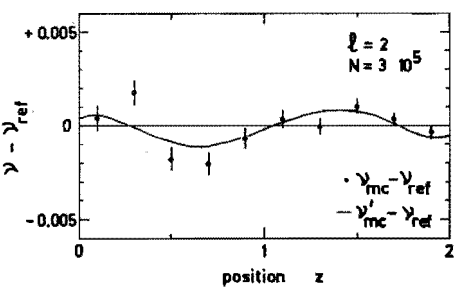

Figure 5.3.3. The wall collision rate for a channel with length $l = 2$. The deviation of the Monte Carlo wall collision rate ν_{MC} and the smoothed Monte Carlo wall collision rate ν'_{MC} from the linear reference wall collision rate ν_{ref}.

5.3.4. The wall collision rate and the angular distribution

Along the axis the channel is divided in equal slices. The number of slices n is large, a typical order of magnitude is 100 l. The output of the Monte Carlo program is an array W with the slice number i as index and the total number of wall collisions with the slice as the elements $W(i)$. We assume a statistical error $W(i)^{\frac{1}{2}}$ in the number of collisions per slice. The collision density on the entrance surface due to molecules entering the channel is equal to $4N/\pi$ with N the sample size. The normalized Monte Carlo wall collision rate $\nu_{MC}(z_i)$ in the points $z_i = (i - \frac{1}{2})\ l/n$ is now given by

$$\nu_{MC}(z_i) = W(i)\ \ n/4lN \qquad (5.3.21)$$

By substituting the normalized Monte Carlo wall collision rate $\nu_{MC}(z_i)$ in equation (5.3.14) and (5.3.15) we can calculate the Monte Carlo angular profile $f(\Theta)_{MC}$ by numerical integration.

By substituting $\nu_{MC}(z_i)$ in the right hand side of the integral equation(5.3.4) and evaluating the integral by numerical integration, we can smooth the statistical noise of the Monte Carlo wall collision rate $\nu_{MC}(z_i)$. Doing this only eliminates noise with a period smaller than the effective range of the kernel D , and this procedure will be most effective for short channels.

We now discuss the results for two channels with $l = 2$ and $l = 25$ respectively.

5.3.4.1. Channel with $l = 2$

To emphasize the deviation of the wall collision rate from a linear function we plot the deviation of the Monte Carlo wall collision rate from the reference wall collision rate ν_{ref}, as given by formula(5.3.7) and (5.3.9). In figure 5.3.3 the solid points are the function $(\nu_{MC} - \nu_{ref})$, with an error bar indicating the statistical error. The sample size is $N = 3\ 10^5$ molecules. The solid line ν'_{MC} is achieved by smoothing the Monte Carlo wall collision rate ν_{MC} with one iteration step in the integral equation. The maximum difference between the smoothed wall collision rate and ν_{ref} is less than 0.001 in

Table 5.3.2 The angular profile $f(\theta)$ for a channel with $l = 25$. The angular profile $f(\theta)_{MC}$ calculated with the Monte Carlo wall collision rate ν_{MC} ($N = 6\ 10^4$) compared with $f(\theta)_{ref}$ calculated with the reference wall collision rate ν_{ref}.

θ°	$f(\theta)_{MC}$	$\sigma(f(\theta)_{MC})$	$f(\theta)_{ref}$
0	1.0000		1.0000
1	0.7269	0.0001	0.7268
2	0.4855	0.0002	0.4848
5	0.2133	0.0003	0.2076
10	0.1174	0.0003	0.1135
15	0.0832	0.0003	0.0810
20	0.0650	0.0003	0.0638
30	0.0448	0.0003	0.0446
45	0.0281	0.0003	0.0280
60	0.0163	0.0002	0.0164
75	0.0072	0.0002	0.0072

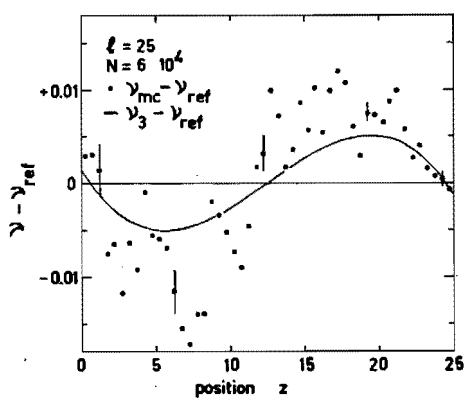

Figure 5.3.4. The wall collision rate for a channel with length $l = 25$. The deviation of the Monte Carlo wall collision rate ν_{MC} and the cubic approximation of the wall collision rate ν_3 of Neudachin from the linear reference wall collision rate ν_{ref}.

absolute measure; in relative measure the deviation is always less than 0.3%.

In table 5.3.1 the results for the angular profile are listed. The first column contains the angular profile $f(\Theta)_{MC}$ as calculated directly from the Monte Carlo wall collision rate ν_{MC}, together with the standard deviation $\sigma(f(\Theta)_{MC})$ due to the statistical noise in the number of collisions per slice.

Due to the short length of the channel smoothing of ν_{MC} is still very effective. After smoothing, different Monte Carlo wall collision rate distributions (with sample size $N = 3\ 10^5$) all result in the same angular profile $f'(\Theta)_{MC}$ as listed in the second column of table 5.3.1 , within an absolute error of 0.0001. In the third column we have listed $f(\Theta)_{ref}$, calculated from ν_{ref}. As one would expect from the coincidence of the wall collision rate, we see a good agreement of $f'(\Theta)_{MC}$ with $f(\Theta)_{ref}$.

5.3.4.2. Channel with $l = 25$

In figure 5.3.4 the solid points are the function $(\nu_{MC} - \nu_{ref})$, the deviation of the Monte Carlo wall collision rate from the reference wall collision rate. An error bar indicates the statistical error. The sample size is $N = 6\ 10^4$ molecules. The solid line represents the deviation of the cubic approximation ν_3 of the wall collision rate of Neudachin (NEU 72) from the reference wall collision rate ν_{ref} . Near the exit we observe a good agreement of ν_{MC} with the cubic approximation ν_3 . Further from the exit the cubic approximation does not fully describe the Monte Carlo results. This can be understood if we realize that Neudachins variational method minimizes the transmission probability, which is mainly determined by the wall collision rate near the exit, in the region $|l-z| < 2$.

In the first column of table 5.3.2 we give $f(\Theta)_{MC}$, the angular profile calculated directly from the Monte Carlo wall collision rate. In the next column the standard deviation $\sigma(f(\Theta)_{MC})$ is given. In the last column we give the angular profile $f(\Theta)_{ref}$ as calculated from the reference wall collision rate ν_{ref}. At large angles we see a good agreement with the Monte Carlo results. At an angle $\Theta = 5^\circ$ half the

channel contributes, and the Monte Carlo angular profile $f(\Theta)_{MC}$ is 3% high compared with $f(\Theta)_{ref}$, as one should expect from the wall collision rate given in figure 5.3.4. Using the cubic approximation will decrease this deviation to less than 1%.

5.3.5. Transmission probabilities

In table 5.3.3 our results for the transmission probability T are compared with the results of different authors. Our values for T in the first row are determined by straightforward counting of the number of transmitted molecules in our Monte Carlo calculations, and dividing this number with the sample size N. The statistical error in T is given by

$$\sigma_T = (1 - T)^{\frac{1}{2}} T^{\frac{1}{2}} / N^{\frac{1}{2}} \qquad (5.3.22)$$

The values T (variational) have been determined by DeMarcus (MAR 55, 56, BER 65) and Neudachin et al. (NEU 72) by solving the integral equation with a variational method and due to the specific method used the values given are upperbounds for the transmission probability. The values T (squeezing) have been determined by DeMarcus (MAR 55,56) with a "squeezing" technique and the errors given should be interpreted as rigorous upper and lower bounds for the value of the transmission probability. The value T (Monte Carlo) was calculated by Ward et al. (WAR 70) with a Monte Carlo method. Within the statistical error our results are in good agreement with all the data discussed above. In the last row we list the values for T given by Clausing (CLA 28). We see that his results are 0.6% high for $l = 2$ and 3% high for $l = 20$.

As an alternative to straight forward counting of transmitted molecules we can also determine the transmission probability by substituting the Monte Carlo wall collision rate in formula (5.3.11). This is the same strategy we used for the calculation of the angular profile. The error is then determined by the statistical error of the contributions of the different slices. In comparison with the straight forward counting we gain in accuracy because we also use information of non-transmitted molecules. For $l = 2$ with a sample size $N = 3\ 10^5$ we

Table 5.3.3 The calculated transmission probabilities T in comparison with results of different authors.

l	0.5	1	2	20	25
N	10^5	$6\ 10^5$	$6\ 10^5$	$1.5\ 10^5$	$1.2\ 10^5$
$T \pm \sigma_T$ a)	0.6725 $\pm$0.0015	0.5148 $\pm$0.0006	0.3568 $\pm$0.0006	0.0597 $\pm$0.0006	0.0488 $\pm$0.0006
T(variational) b)		0.51423	0.35658	0.05952	0.0485
T(squeezing) c)	0.671984 $\pm$0.000005	0.51423 $\pm$0.00001			
T(Monte Carlo) d)			0.3568 $\pm$0.0002		
T(Clausing) e)	0.6720	0.5136	0.3589	0.0613	0.0499

a) this work; b) a linear trial function was used (MAR 55, 56 , NEU 72, BER 65); c) DeMarcus (MAR 55, 56); d) Ward et al. (WAR 70); e) Clausing (CLA 29).

find $T = 0.3564 \pm 0.0004$ and we have gained a factor two in accuracy in comparison with σ_T. However, because accurate values of the transmission probability are available, we did not further employ this method and we only use our T values as an extra check on the calculations.

5.3.6. Collision number distributions

In the previous part of this paper we have always assumed ideal diffusively reflecting walls. However, in an experiment this condition is not always fulfilled. Processes such as adsorption by the wall (SMI 66) or recombination on the wall (LIV 71) will effect the flow in the channel. The magnitude of the effect will depend on the number of wall collisions a molecule suffers inside the channel.

In this section we investigate the number of wall collisions in a channel with ideal diffusively reflecting walls and apply the results to the problem of a channel with adsorbing walls (SMI 66).

We define the distribution functions $T(p)$ and $R(p)$ as the distribution of the transmitted and reflected molecules with respect to the number of wall collisions p they have suffered before leaving the channel through the exit or the entrance respectively. The functions $T(p)$ and $R(p)$ are only defined for integral values of p larger or equal to zero and larger or equal to unity respectively. The distribution functions are normalized by the conditions

$$\sum_{p=0}^{\infty} T(p) = T$$

$$\sum_{p=1}^{\infty} R(p) = 1 - T \qquad (5.3.23)$$

Thus $T(p)$ is the fraction of the molecules entering the channel that leaves the channel through the exit after exactly p collisions with the wall.

The average number of collisions $\langle p \rangle$ of all molecules (reflected or transmitted) is given by

$$\langle p \rangle = 2\,l \qquad (5.3.24)$$

which can easily be derived from $v(z)$ using the symmetry relation of equation (5.3.5).

For the transmitted molecules the average number of collisions $\langle p_T \rangle$ is given by

$$\langle p_T \rangle = \frac{1}{T} \sum_{p=0}^{\infty} p\,T(p) \qquad (5.3.25)$$

For long channels Clausing (CLA 28) calculated $\langle p_T \rangle$ by considering the flow as a diffusion problem, resulting in

$$\langle p_T \rangle = l^2 / 2 \qquad (l >> 1) \qquad (5.3.26)$$

We can understand this result by considering the random walk of the molecules in the channel. The average length $\langle |s| \rangle$ of a displacement along the axis between two successive wall collisions is equal to ½. To be transmitted the total displacement has to be larger than the length l of the channel. In a one-dimensional random walk problem, the mean square displacement is proportional to the number of collisions and we expect $\langle p_T \rangle \approx l^2$. However, we can give $\langle p_T \rangle$ as a function of the wall collision rate $\nu(z)$. The probability that a molecule colliding with the wall at position z will leave the channel through the exit without passing the entrance plane is equal to $(1 - \nu(z))$ (CLA 28). For $\langle p_T \rangle$ we get the expression

$$\langle p_T \rangle = \frac{4}{\pi T} \int_0^l \nu(z) \, (1 - \nu(z)) \, \pi \, dz \qquad (5.3.27)$$

Using the linear approximation of $\nu(z)$ results in

$$\langle p_T \rangle = \frac{2l}{3T} \, (1 + 2\alpha - 2\alpha^2) \qquad (5.3.28)$$

In the limiting case of long channels we get the result of Clausing (formula (5.3.26)) by substituting $T = 4/3 \, l$ and neglecting terms of lower order than l^2.

The average number of collisions $\langle p_R \rangle$ of a reflected molecule is given by

$$\langle p_R \rangle = \frac{\langle p \rangle - T \langle p_T \rangle}{1 - T} \qquad (5.3.29)$$

In the limiting case of long channels this results in

$$\langle p_R \rangle = 4l / 3 \qquad (5.3.30)$$

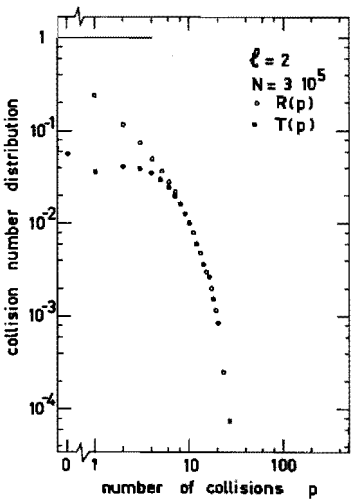

Figure 5.3.5. The normalised distributions R(p) and T(p) of the reflected and transmitted molecules with respect to the number of wall collisions in the channel, for a channel with length l = 2.

Table 5.3.4 Theoretical and Monte Carlo values of the average number of collisions <p> of all molecules, and the average number of collisions $\langle p_T \rangle$ and $\langle p_R \rangle$ of molecules that are transmitted and reflected respectively.

		$\langle p_T \rangle$		$\langle p_R \rangle$		<p>	
l	N	theor. a)	Monte Carlo	theor. b)	Monte Carlo	theor. c)	Monte Carlo
2	$2\ 10^4$	4.76	4.80	3.58	3.55	4	3.998
25	$6\ 10^4$	358.6	364.4	34.2	33.9	50	50.000

a) equation (5.3.28); b) equation (5.3.29); c) equation (5.3.24).

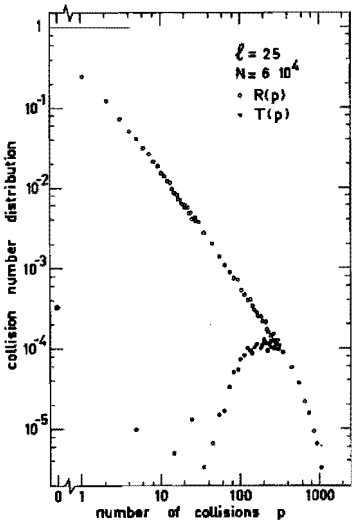

Figure 5.3.6. The normalised R(p) and T(p) of the reflected and transmitted molecules with respect to the number of wall collisions in the channel, for a channel with length l = 25.

In the Monte Carlo calculation we have recorded the distribution functions $R(p)$ and $T(p)$. In table 5.3.4 we compare the Monte Carlo values for $\langle p \rangle$, $\langle p_T \rangle$ and $\langle p_R \rangle$ with their theoretical values calculated with the equations (5.3.24), (5.3.28) and (5.3.29). We see a good agreement.

In figure 5.3.5 and 5.3.6 we have plotted $R(p)$ and $T(p)$ for channels with $l = 2$ and $l = 25$ respectively. For large p values we see that $R(p)$ and $T(p)$ coincide, in other words after a large number of collisions a molecule forgets that it entered from one side of the channel, it has lost its "memory". The molecule than has an equal chance of leaving the channel on either side. This is confirmed by recording the contribution to the wall collision rate of these molecules, which is an even function in $(z - l/2)$. For small values of p the distribution function of reflected molecules $R(p)$ is nearly independent of l, for long channels. For example for $l = 20$ and $l = 25$ the first significant difference shows up at $p = 25$.

We now apply these collision number distributions to the problem of a cylindrical channel with adsorbing walls, which is discussed by Smith and Lewin (SMI 66). When γ is the sticking coefficient for one single collision, the transmission probability T_γ and the reflection probability R_γ are given by

$$T_\gamma = \sum_{p=0}^{\infty} (1-\gamma)^p \; T(p)$$

$$R_\gamma = \sum_{p=1}^{\infty} (1-\gamma)^p \; R(p) \qquad (5.3.31)$$

They can be calculated from one Monte Carlo calculation of $R(p)$ and $T(p)$. Also the dependence of R_γ and T_γ on the values of l and γ can be clarified. From the large number of collisions of transmitted molecules in the case of long channels we can understand the large effect of small values $\gamma = 0.01$ on the transmission probability. By considering the behaviour of $R(p)$ for small values of p we can understand that for large values of the sticking coefficient the reflection probability becomes independent of l with increasing length.

5.3.7. Conclusions

Free molecular flow in a cylindrical channel has been investigated. In the field of molecular beams various approximations of the wall collision rate have been used to calculate the angular distribution of the molecules leaving the channel.

Good predictions for the angular distribution are obtained by using the linear or cubic approximation to the wall collision rate, as calculated by DeMarcus (MAR 55,56) and Neudachin (NEU 72) with a variational method. By comparison with the actual solution for the wall collision rate, calculated with a Monte Carlo method, we have investigated the accuracy of their results. For short channels their linear approximation gives a satisfactory description of the Monte Carlo results for the angular distribution. Using the linear approximation for long channels results in deviations of a few percent at small angles. Using Neudachins cubic approximation will decrease these deviations to less than one percent.

Two models which are quite often used are those of Giordmaine and Wang (GIO 60) and Zugenmaier (ZUG 66). However, both models are in contradiction with the actual shape of the wall collision rate. The

first model employs a linear wall collision rate with an exit collision rate equal to zero. The second model uses a linear function with a finite exit collision rate, but violates the symmetry of the solution by always using an entrance collision rate equal to unity. Predictions for the angular distribution from both models are quite unsatisfactory.

In many cases the results of a linear wall collision rate of the correct symmetry with an exit collision rate equal to $T/2$ are accurate enough for comparison with experimental results (BEIJ 75).

A final conclusion concerns the use of Monte Carlo techniques. With a Monte Carlo method complicated problems can often be treated in a very simple way. However, when applying such a method, it is often useful to consider carefully which information we have to generate and how we can gain by combining Monte Carlo results and simple analytical formulae.

5.3.8. Appendix: the displacement distribution function and the formula for the angular profile

We derive the probability distribution $D(s)$ for a displacement s (eqaution (5.3.1)) and the formula for the calculation of the angular profile $f(\theta)$ (equation (5.3.13)) from the cosine law for molecules leaving the wall and the geometry of the channel.

The normalized probability distribution for starting directions from the wall is given by

$$F(\theta',\phi')\, d\theta'\, d\phi' = \frac{\cos\theta' \sin\theta'}{\pi}\, d\theta'\, d\phi' \qquad (5.3.32)$$

with $0 \leq \theta' \leq \pi/2$

$0 \leq \phi' < 2\pi$

with (θ' , ϕ') polar angles with respect to the normal on the wall in the point of collision.

We transform the distribution to polar angles (θ , ϕ) with respect to the channel axis, with $\phi = 0$ corresponding to the normal on the wall.

$$F_1(\Theta\ ,\ \phi) = \frac{2}{\pi}\ \sin^2\Theta\ \cos\phi\ d\Theta\ d\phi \qquad (5.3.33)$$

with $0 \leq \Theta \leq \pi$

$-\pi/2 \leq \phi \leq \pi/2$

Transformation to the displacement $s = \cos\phi\ /\tan\Theta$ and the angle Θ yields

$$F_2(\Theta\ ,\ s)\ d\Theta\ ds = \frac{2}{\pi}\ \sin^2\Theta\ \frac{s\ \tan^2\Theta}{(1 - s^2\tan^2\Theta)^{\frac{1}{2}}}\ d\Theta\ ds \qquad (5.3.34)$$

with $s \geq 0$ and $0 \leq \Theta \leq \arctan(s^{-1})$

or $s < 0$ and $\arctan(s^{-1}) \leq \Theta \leq \pi$

The probability distribution $D(s)$ for a displacement s is now given

$$D(s)\ ds = \left(\int_0^{\arctan(s^{-1})} F_2(\Theta\ ,\ s)\ d\Theta\right) ds \qquad (s \geq 0) \qquad (5.3.35)$$

resulting in equation (5.3.1)

We now discuss equation (5.3.13) for the calculation of $f(\Theta)$. The probability of a molecule for leaving the wall at an angle Θ with the channel axis and having a displacement larger than s is given by

$$\left(\int_s^{(\tan\Theta)^{-1}} F_2(\Theta\ ,\ s')\ ds'\right) d\Theta = \frac{2}{\pi}\ \sin^2\Theta\ (1 - s^2\ \tan^2\Theta)^{\frac{1}{2}}\ d\Theta$$

$$(s \geq 0) \qquad (5.3.36)$$

The probability per unit of solid angle is found by dividing by $2\pi\sin\Theta\ d\Theta$. Multiplication by 4 satisfies the condition $f(0) = 1$ when using the normalized wall collision rate. The contribution to $f(\Theta)$ of

the wall collision rate of a slice located between z and $z + dz$ is given by

$$\pi \, \nu(z) \, dz \quad \{ \frac{4\sin\theta}{\pi 2} \quad (1 - ((1 - z) \tan\theta)^2)^{\frac{1}{2}} \}$$

and equation (5.3.13) is selfevident.

6. The new time-of-flight machine

6.1. Introduction

The molecular beam machine consists of 6 differentially pumped vacuum stages. A schematic view of the machine is given in figure 6.1.

In the first chamber the main beam source is located. The second chamber contains the chopper motor assembly. In the third chamber the secondary beam is located.

The first two chambers are mounted on carriages that run on two rails. The chambers can be rolled back to provide an easy accessibility while retaining the alignment of the chambers with respect to the third chamber, which is fixed to the frame. The beam axis, i.e. the axis of the alignment telescope, has been aligned with respect to the third chamber.

The fourth chamber only serves as a buffer chamber for the connection to the fifth chamber, i.e. the detector chamber. The detector chamber has a differentially pumped inner chamber (stage 6), in which the beam detector is mounted. The beam passes through the inner chamber and is dumped in the outer detector chamber. The stages 4, 5 and 6 are all mounted on a subframe that can be adjusted with respect to the main frame. This sub-assembly is connected to stage 3 with a bellows.

Between stage 4 and 5 an in-line all metal UHV valve is located, which is used to separate the detector chamber from the buffer chamber during a bake-out. With this valve it is also possible to demount the whole detector chamber assembly without letting the chamber up to air.

In the design of the beam machine special emphasis is laid on reliability and flexibility. For a large molecular beam machine flexibility is of vital importance, to allow for changes in the

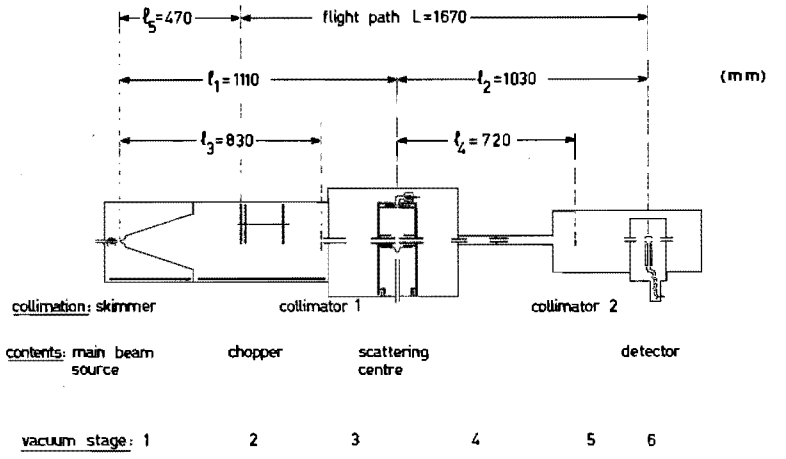

Figure 6.1. Schematic view of the new time-of-flight machine

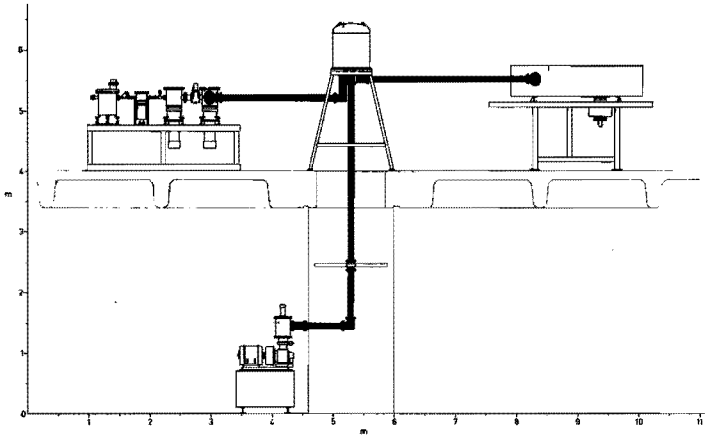

Figure 6.2. The cryopumping facility

research program.

The molecular beam machine is alternately used for two research projects, as mentioned in chapter 1. The change-over from one configuration to the other only takes one day.

In the Eindhoven molecular beam group two central experimental facilities are available for all molecular beam machines: the cryo-pumping facility and the computer facility. They are briefly discussed in the following sections 6.1.1. and 6.1.2..

6.1.1. The cryopumping facility

In the Eindhoven molecular beam group much effort has been put in providing several molecular beam machines with the facility of extensive 20 K cryopumping. With a distribution system (SES 70, 72) the large output of a Stirling A20 cryogenerator - 50 Watt at 18 K and 500 Watt at 80 K - can be connected to a maximum of four experimental set-ups.

In figure 6.2 a schematic view of the set-up is given. The Stirling cryogenerator is located in the basement. The cold is delivered to heat exchangers at the two temperature levels. The cold is transported by circulating pressurized He gas (20 atm) in closed circuits, one for each temperature. The helium flow is driven by electrical fans. A low loss, vacuum jacketed transport line connects the cryogenerator to the distribution station in the main laboratory room on the first floor, where also the experimental set-ups are located.

Each experimental set-up can be connected independently either to an auxiliary circuit for warming up or to the cold output of the cryo-generator. Simultaneous use of the cold by more than one experiment is possible. From the distribution station four transport lines radiate outwards to the four users.

Cryopumps at the experimental set-ups are part of the circulation loops and consist of soft copper pipe soldered onto copper shields of the desired geometry. Designing problems are reduced by the large amount of available 20 K cooling power.

6.1.2. The computer facility

Since spring 1971 a PDP-11/20 computer is available in the group, with 8k of 16 bit core memory and a high speed reader/punch and a teletype as peripherals. This initial configuration was bought with only the time-of-flight experiment in mind, as an alternative for a multiscaler. A multiscaling interface and a plotter/scope connection (GEE 72a) were the first interfaces to be finished.

In the period 1973-1975 a home-made multiuser interfacing system (LOW 73, VUG 75) was developed allowing a maximum of eight independent users, i.e. experimental set-ups. The experiments connected are two from the molecular physics group and two from the neighbouring atomic physics group. An extension with one experiment from each group is expected in the near future. Due to the increase of active users the 8k core memory was extended to 24k, and recently a 1M disc unit for data and program storage has been added. Two extra teletypes have been added as user terminals in the atomic physics group.

A multiuser operating system ROSIE (Real-time Operating System for Independent Experiments) (GEE 73, SLA 74, SMI 74) has been developed, which handles up to eight independent real time user programs. Special features of ROSIE are its flexibility and the convenient man-machine communication. All basic measuring routines are available as standard commands, with a set of free parameters for a detailed specification of the routine. Each command can be used in a direct mode. More important however is the possibility for typing in a list of these commands that is stored in memory and can be executed on request. Parts of the program can be repeated with a for-statement. Conditional statements can be used to warn the experimentalist when experimental parameters drift out of their specified range. Simple arithmetic operations can be performed on arrays of measured data. Mode statements are used to specify if different tasks in the program are to be executed parallel or in series.

6.2. Vacuum system

In table 6.1 the characteristics of the vacuum system are listed, together with typical operating conditions.

The buffer chamber and the detector chamber are standard UHV equipment, bakeable at 400°C. A special bake-out oven has been developed (BEIJ 73). A schematic view of the oven is given in figure 6.3. The oven is double walled and constructed from aluminum plate. Four hot air guns are used for heating, each with a maximum heat output of 3 kW. An air compressor delivers the air flow of 1500 l/min. Each hot air gun can be switched on to deliver 1.2, 1.8 or 3 kW. The intake of the air compressor can be throttled. With these two facilities we can adjust the temperature inside the oven. The large flow of turbulent hot air at the desired temperature guarantees a uniform temperature inside the oven. During the bake out the detector chamber is pumped with a separate ion-getter pump connected to the roughing line of the detector chamber.

Due to the plug-in nature of the hot air guns the actual heating system, i.e. air compressor and hot air guns, is not specific for one oven but is used for several experiments within the department.

The vacuum system is safeguarded against failure with standarised safeguarding modules (BEIJ 74). An important feature of the safeguarding provisions is a pneumatically operated in-line valve between stage 3 and 4, which closes automatically in case of any failure in the first three stages to save the ultra high vacumm of the detector chamber.

The total pressure in the inner detector chamber is of the order of magnitude of 10^{-10} torr. The partial pressure of argon under typical operating conditions is $\leq 10^{-11}$ torr, as determined from the effective area for residual gas detection and the absolute efficiency for molecular beam detection.(see section 6.6). This corresponds to a count rate of 1.5 kHz.

A typical residual gas spectrum is given in figure 6.4.

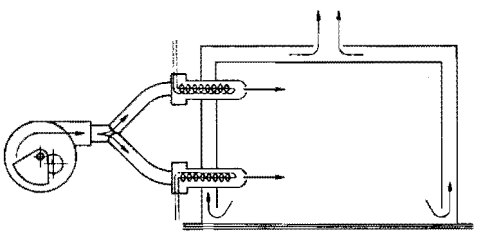

Figure 6.3. Schematic of the bake-out oven with the air compressor and the hot air guns.

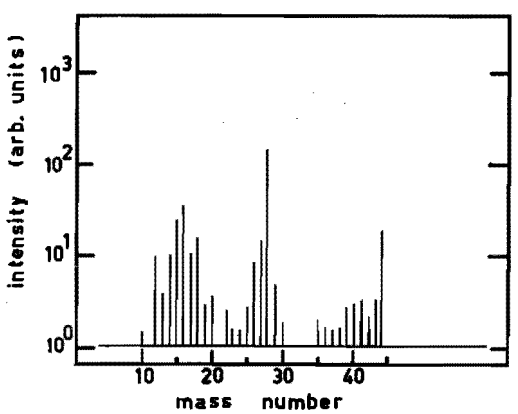

Figure 6.4. Residual gas spectrum of the inner detector chamber. The total pressure is of the order of 10^{-10} torr. (mass numbers 2 and 4 have not been measured)

Table 6.1 Characteristics of the vacuum system

Vacuum stage i	Name of stage	Pump	Flow resistance stage $i \rightarrow i+1$ (1/s)	Operating pressure (torr)	General information
1	Source chamber	800 l/s oil diffusion 20 K cryopump		$5\ 10^{-5}$	Primary beam source, possibility of cryo-expansion chamber $J_{primary} = 0.1$ torr l/s
2	chopper chamber	680 l/s oil diffusion 20 K cryopump	1.8	$3\ 10^{-8}$	Chopper motor, calibration source, beam collimators
3	scattering chamber	180 l/s oil diffusion 20 K cryopump	0.23	$1\ 10^{-8}$	Secondary beam source, cryo-expansion and beam trap chamber, $J_{secondary} = 1$ torr l/s
4	buffer chamber	1 l/s ion getter	0.38	$5\ 10^{-9}$	UHV, bakeable
5	outer detector chamber	50 l/s ion getter	1.0	$5\ 10^{-10}$	UHV, bakeable, beam collimator
6	inner detector chamber	20 l/s ion getter	1.0	$1\ 10^{-10}$	UHV, bakeable, beam detector

6.2.1. Differential pumping

As mentioned in the introduction the molecular beam machine is a multistage differentially pumped machine. One might wonder how effective differential pumping is in the case of a beam machine, with the flow resistances, the source and the detector all carefully aligned. Insight in this problem is achieved by considering the optical analog of free molecular flow. Walls are ideal reflecting surfaces. Molecules are only emitted from surfaces and travel straight line trajectories. The background density in the ionizer of the detector is given by

$$\int_{4\pi} \frac{n(\Omega)}{4\pi} \, d^2\Omega \qquad (6.1)$$

where $n(\Omega)$ is the local density near the surface, that is seen in the direction Ω. The major part of the solid angle is taken up by the detector chamber itself, and follows the simple formula of differential pumping. The contribution in the direction of the beam axis could spoil the differential pumping. This contribution is written as

$$\sum_i \frac{n_i A_i}{4\pi l_i^2} \qquad (6.2)$$

as a summation over the number of stages i , with density n_i and effective area A_i at a distance l_i. A worst case estimate of an area of 10 mm^2 at 1 m from the detector with a pressure of 10^{-6} torr gives a background density of 10^{-12} torr, which is of the same order of magnitude as the partial pressure of the beam gas inside the detector chamber. In normal operating conditions this effect can be neglected.

A dangerous situation can occur when using a scattering box instead of a secondary beam. One then has to take care that the exit aperture of the scattering box is smaller than the entrance aperture, to avoid that the detector can see the highly illuminated (high density) inside walls of the box.

6.3. Primary beam

6.3.1. Beam source

All primary beam sources are plug-in modules. Pumping of the primary beam is done with a cryo-expansion chamber (section 6.5.) or with an oil diffusion pump with a cryopump as a conventional background pump.

In the scattering experiments described a supersonic beam source was used, with the second mode of pumping. The skimmer is fixed to the source flange, the nozzle position is externally adjustable with micrometers. A 15 mm long conical skimmer is used of 0.3 mm diameter. The nozzle diameter is large, typically 250 μm, to pair a high intensity with operation at low inverse Knudsen numbers, i.e. a broad velocity distribution. The intensity distribution over the skimmer opening is fairly uniform due to the large size of the virtual source (section 5.1.3.). A typical operating pressure is 10 torr, resulting in an inverse Knudsen number of 50 and a flow rate of the order of 10^{-1} torr l/s.

Higher primary beam velocities are achieved by heating the nozzle tip over a length of 10 mm with a closely wound tungsten filament. The nozzle material is alumina; the nozzles are made by grinding a small hole in a sealed-off tube. The gas temperature is limited to 1500 K, further acceleration has to be done by using the "seeded beam" technique (MIL 69).

6.3.2. Beam collimation

The skimmer of the primary beam source is the first collimator and the actual beam source with sharp boundaries. The second collimator is located in the chopper chamber, near the scattering center. The third collimator is located in the outer detector chamber (figure 6.1). Both collimators are externally adjustable with micrometers. Each collimator has three collimating holes with different diameters that are externally interchangeable. Typical collimator diameters range from 0.1 to 1 mm. The dimensions of the collimators used for the scattering experiments are given in section 7.1.

The alignment of the collimators on the beam axis is done with the

Table 6.2 Characteristic measures of the chopper

Outer diameter discs	176	mm
Disc thickness	1.5	mm
Distance first disc-second disc	19.5	mm
Distance first disc-third disc	175	mm
First disc: beam slit I	1.50	mm
beam slit II	4.80	mm
synchronization slit	9°	
Second disc	20°	
Third disc: cut-off slit	$16^{\circ}\ 30'$	
velocity selector slit	1.50	mm

Table 6.3 Chopper slit characteristics and timing diagram of a synchronization period

Chopper slit characteristics	Slit I	Slit II
Slit width (mm)	1.50	4.80
Slit height (mm)	3.0	3.0
Radius center of slit (mm)	73.5	76.5
Open time	0.0065 T	0.020 T
Timing normal mode		
Synchronization pulse	$t = 0$	$t = 0$
Center of transmission function of beam	$t = 0.025\ T$	$t = 0.025\ T$
Begin beam cut-off	$t = 0.69\ T$	$t = 0.63\ T$
End beam cut-off	$t = 0.75\ T$	$t = 0.81\ T$
Effective measuring range	0.665 T	0.605 T
Background	0.25 T	0.19 T
Timing velocity selecting mode		
Synchronization pulse	$t = 0$	
Transmission beam molecules	$t = 0.025\ T$	
Arrival selected molecules	$t = 0.50\ T$	

aid of a telescope, fitted with a parallel displacer, and an intense light source. We use a 150 W halogen slide projector lamp, which provides a spatially uniform light source of 3 x 3 mm^2. A typical alignment procedure is the following. After mounting the primary beam source the axis of the telescope is centered on the skimmer with the parallel displacer. Then the detector is adjusted to the new beam axis, with the help of the measured displacement of the beam axis. The nozzle position is then optimized on beam intensity by scanning the nozzle over the skimmer. With the telescope the remaining collimators at the scattering center and the detector are aligned. Finally the alignment is checked by scanning the primary beam with the middle collimator.

After demounting of the primary beam source the position of the beam axis reproduces within an area of 1 mm diameter. The diameters of the flow resistances between the different vacuum stages are all much larger ($\geq$ 5 mm) and allow this displacement.

6.4. Chopper motor

In the second vacuum stage a three disc chopper is located (figure 6.5.a and 6.5.b). Each disc has two slits opposite each other, for reasons of balancing. Each revolution of the chopper motor thus corresponds to two chopper periods.

In figure 6.6 we show the configuration of the slits in the three chopper discs and their alignment. The wide slit at the circumference of the first disc is used for the synchronization mechanism and will be discussed later.

The first disc is the actual beam chopper. By externally adjusting the vertical position of the chopper one can choose from two slits of different width, i.e. different time resolution.

The last disc has a broad slit to cut-off low velocity molecules as a normal chopper (figure 4.1) and a narrow slit for use as a velocity selecting chopper for calibration purposes (figure 4.5). We choose from these two possibilities by spinning the chopper in the normal or reverse direction.

An intermediate disc is used to eliminate molecules that could be

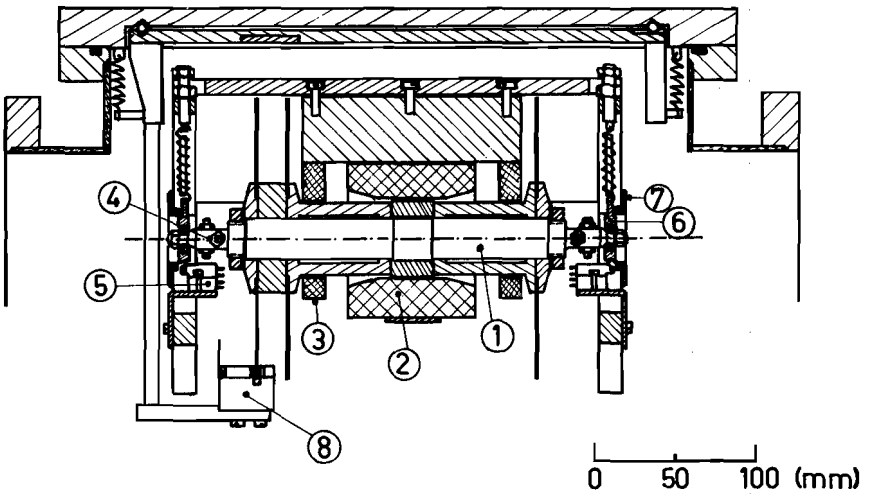

Figure 6.5.a. Side view of the chopper motor

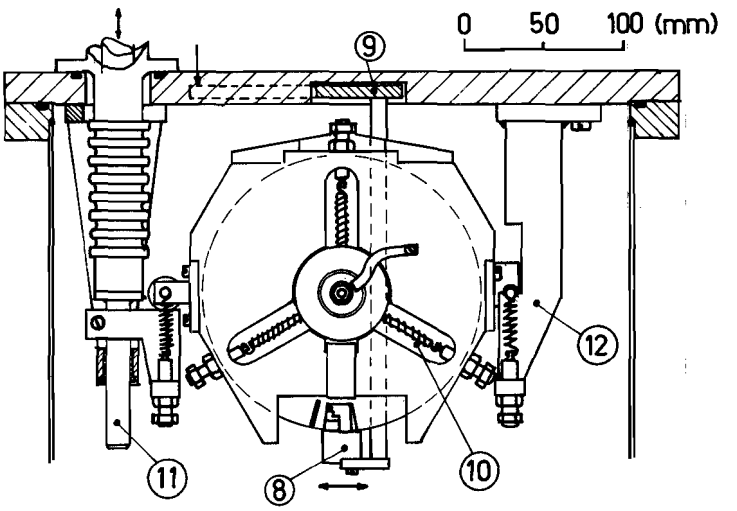

Figure 6.5.b. Front view of the chopper motor, seen from the detector. 1) motor axis; 2) stator; 3) teflon safety catch; 4) balancing screws; 5) vibration monitor (hi-fi stereo cartirdge); 6) ball-bearing housing; 7) teflon ring, for limitation of axial movement; 8) syncrhonization assembly; 9) support of the synchronization assembly; 10) suspension springs of ball-bearing housing; 11) adjustable support of chopper motor; 12) fixed support of chopper motor.

transmitted by the last disc in the next period.This is only the case when using the wide slit of the first disc; when using the narrow slit the thickness of the first disc is sufficient.

The chopper can be lifted completely out of the beam for alignment of the main beam.

In table 6.2 the characteristic measures of the chopper are given. In table 6.3 the characteristics of the two chopper slits in the first disc are given, together with their timing diagram within a chopper period.

6.4.1. Synchronization assembly

In figure 6.7 the synchronization assembly is drawn, together with the first chopper disc. The synchronization pulse is derived from the lamp-phototransistor set, when the leading edge of the broad synchronization slit on the circumference of the first disc passes the light beam.

Connected to the actual synchronization mechanism is a molecular beam slit, 3 mm wide and 5 mm high. This slit is located in a vertical plane exactly above the light beam. With a micrometer the position of the synchronization assembly can be externally adjusted in the horizontal plane, in a direction perpendicular to the primary beam (figure 6.5.b). By scanning the synchronization assembly it is centered on the primary beam. The light beam of the synchronization mechanism and the primary beam are then in one vertical plane.

Due to the special configuration of the first chopper disc the synchronization pulse now has a well determined negative off-set of 0.025 T with respect to the center of the transmission function of the chopper for the molecular beam, with T the chopper period. Due to the symmetry of the slits this off-set is independent of the direction of rotation of the chopper.

The width of the light beam of the synchronization mechanism is 0.5 mm, resulting in a maximum error in the off-set of $\pm$ 0.001 T without any further calibration.

Fluctuations of a few percent in the chopper period have a negligible influence on the off-set.

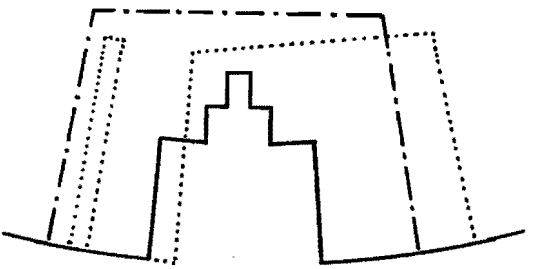

Figure 6.6. Alignment of the slits in the three chopper discs, as seen from the primary beam source. Solid line: first chopper disc; dash-dotted line: second chopper disc; dotted line: third chopper disc. Normal mode: clock-wise rotation. Velocity selecting mode: counter clock-wise rotation.

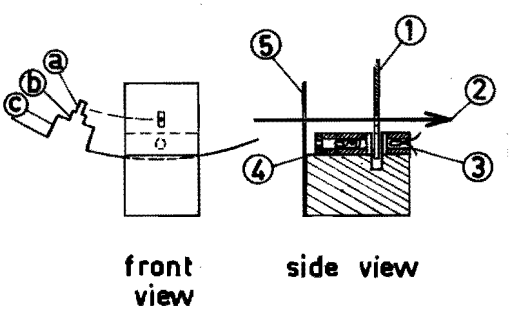

Figure 6.7. Synchronization assembly. 1) first chopper disc; 2) molecular beam; 3) photo diode; 4) lamp; 5) collimating slit for molecular beam; a) slit I; b) slit II; c) synchronization slit. By scanning the syncrhonization assembly in the horizontal plane it is centered on the molecular beam.

6.4.2. Construction features

The chopper motor is a two phase induction motor, driven with a variable frequency between 20 Hz and 500 Hz. The stator is encased in an epoxy resin, which has been applied in a vacuum oven. This epoxy resin serves as a heat conductor to transport the dissipated power from the stator windings to the base plate of the motor. It also diminishes the outgassing of the segmented core of the stator. The rotor on the axis is a soft iron ring.

The measured torque M(Nm) of the motor is given by

$$M = 3\ 10^{-4}\ I_{eff}^{2}\ \Delta f \qquad (6.3)$$

for $\Delta f \leq 30$ Hz. The quantity Δf(Hz) is the slip between the applied frequency and the rotation frequency of the motor and I_{eff}(A) is the effective current for each phase of the stator. More detailed measurements are reported elsewhere (LOW 73a).

Fitted with MPB (Miniature Precision Bearings/Krytox 240Ac) ball-bearings with the original lubricant the chopper motor has a slip Δf = 4 Hz at a driving frequency of 78 Hz and a stator current I_{eff} = 1 A. The friction of the bearings, and thus the slip, can be considerably reduced by replacing the lubricant by molybdinum powder.

The axis is supported by a ballbearing at each side. The outer ring of the ballbearing is mounted in a light weight aluminum housing, supported by three springs. These springs are damped by rubber string mounted inside the springs. In this way the dynamical load of the bearings, due to an unbalance of the axis, is minimized.

Chopper discs are located at both sides of the stator, and thus the final balancing has to be done in situ after mounting the axis. Two stereo cartridges (from a record player) serve as a vibration monitor, with their needle in an axial groove in the housing of each bearing. The phase and amplitude of the output of the stereo cartridges are correlated to the position and magnitude of the unbalance of the axis. At each side the axis has two balancing screws at a 90^{o} angle. By successively displacing these balancing screws we introduce an extra unbalance which allows us to calibrate the output of the stereo

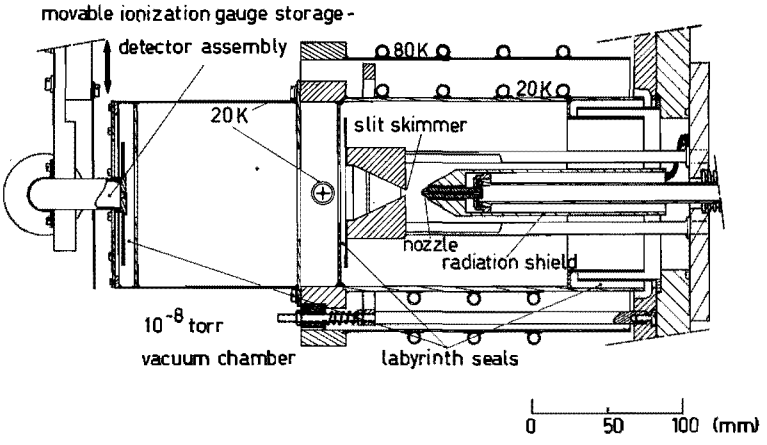

Figure 6.8. Side view of the secondary beam source, as seen from the primary beam source. The cross indicates the primary beam.

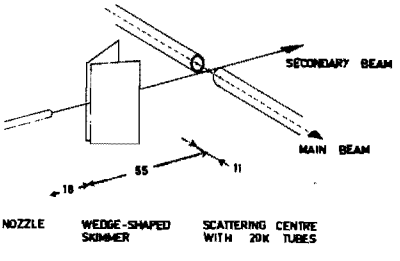

Figure 6.9. Schematic view of the scattering center.

cartridges. With this calibration it is an easy procedure to balance the axis dynamically with the balancing screws by successive iteration (MEN 74).

6.5. Secondary beam

The secondary beam is a cryopumped room temperature supersonic beam source (HAB 73). The skimmer is fixed to the source flange, the nozzle is moveable in all directions through a bellows and is adjusted externally with micrometers. The nozzle-skimmer distance can be varied over a range of 20 mm. Quartz nozzles are used, which are made by grinding a small hole in the fused end of a capillary. A typical nozzle diameter is 200 μm. The nozzle is kept at room temperature by using a radiation shield. The skimmer is not conical but wedge-shaped. The wedge is perpendicular to the main beam. The width of the skimmer slit can be set in the range of 0.1 to 1.8 mm. The height of the slit is 3 mm. It is a slender and long skimmer with inner and outer half angles or 15° and 20° respectively. The length of the wedge is 18 mm.

The secondary beam is pumped in an 20 K cryo-expansion and beamtrap chamber. A schematic view of the secondary beam cryopump is given in figure 6.8. The effective pumping speed of the cryo-expansion chamber is of the order of magnitude of 10^4 l/s. At the maximum flow rate of 5 torr l/s the pressure inside the cryo-expansion is less than $7\ 10^{-4}$ torr. Sealing of the cryo-expansion chamber to the cryo-beamtrap and the outer vacuum chamber is accomplished with "cold labyrinth" seals (figure 6.8). Due to the high sticking coefficient ($\geq$ 0.995 for room temperature N_2 on a 17 K surface (HAB 75a))the tightness of the seals is very satisfactory. Spacious clearings in the seals allow for thermal contractions and for easy mounting. In fact the source is designed as a plug-in unit.

The source is fed from a gashandling system with a constant pressure, provided by an adjustable pressure reducer on a high pressure gas cylinder and measured with a capsule dial gauge. Facilities are available to measure the flow rate through the nozzle with a pressure drop method.

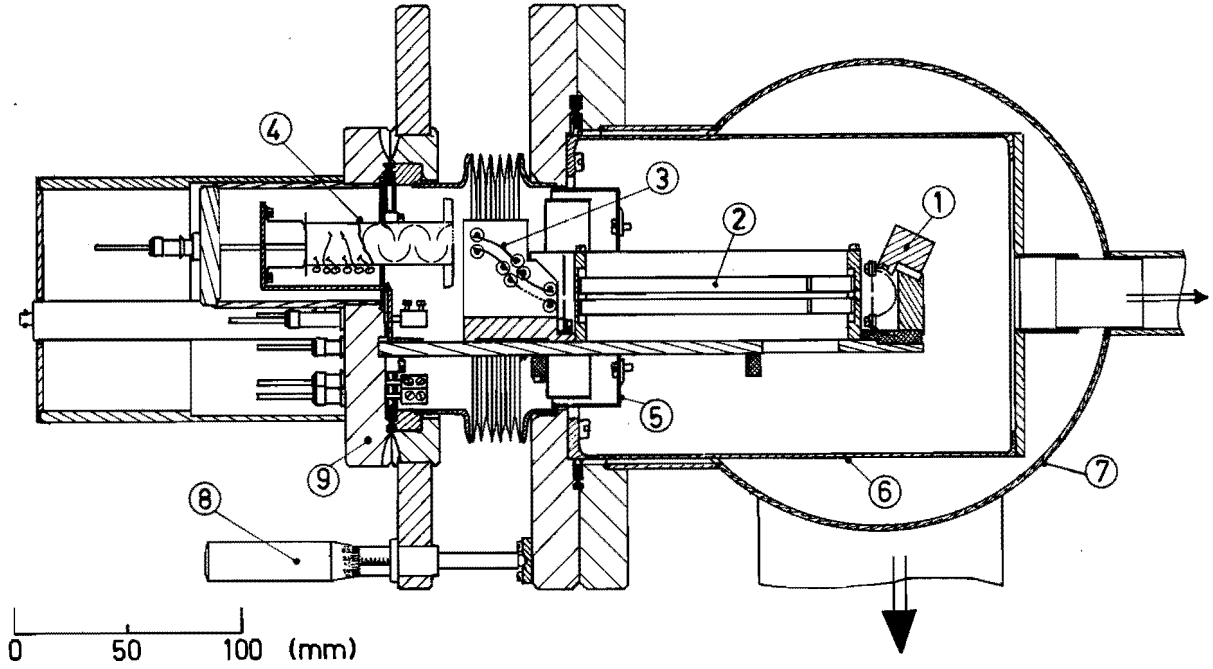

Figure 6.10. Side view of the detector inside the detector chamber. 1) ionizer; 2) quadrupole rods; 3) deflection plates; 4) electron multiplier; 5) labyrinth; 6) inner detector chamber; 7) outer detector chamber; 8) micrometer; 9) flange of detector assembly.

Switching the beam on and off during the scattering experiment is done with two electro-pneumatic valves that connect the source either to the pressure reducer or to a rotary vacuum pump. Compared with a beam shutter the switch over time is quite long ($\sim$ 10 s), but good results are guaranteed. A beam shutter inside the expansion chamber of a supersonic beam source can easily interfere with the expansion process.

An ionisation gauge is used as a storage detector for monitoring the center-line intensity and for measuring beam profiles.

In figure 6.9 a schematic view of the scattering center is given. The beams are crossed at an angle of 90°. Due to the fact that the skimmer wedge is perpendicular to the main beam the"scattering profile" is well determined and constant over the cross-section of the main beam. To protect the main beam, it passes the scattering center through 12 mm diameter tubes at 20 K, only leaving an opening of 11 mm at the intersection of the beams. A typical value of the skimmer width is 1.5 mm with a 15 mm nozzle-skimmer distance, resulting in a full opening angle of 0.1 rad. The geometrical width at the intersection of the beams then is 5.5 mm. The height at the intersection is 12 mm.

The secondary beam source is directly interchangeable with the main beam source, enabling us to make an accurate TOF analysis of the parallel velocity distribution of the secondary beam. With these features the scattering center is well defined.

6.6. Detector system

The detector assembly is mounted in the inner detector chamber, in the horizontal plane and perpendicular to the molecular beam. It consists of an ionizer, a quadrupole mass filter, a set of deflection plates and an electron multiplier. A bellows allows external adjustment of the assembly with three micrometers (figure 6.10).

Output pulses of the electron multiplier ($\sim$ 5 10^4 electrons/ion) are fed into a charge sensitive amplifier (Simtec P-11). Further amplification and analysis is done with an amplifier/pulse height analyser (Ortec 486). The TTL output of the analyser (operated in integral mode, i.e. all pulses above the lower level are accepted) is

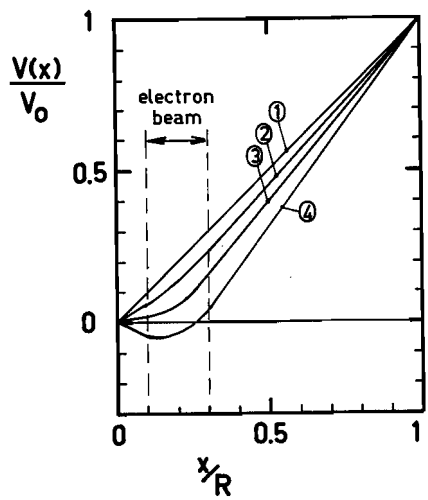

Figure 6.11. Potential between two infinite flat plates, with an infinite electron sheet with a uniform current density j(A/m^2) centered at x = 0.2 R with height d = 0.2 R. The electron energy is 100 eV. Due to the surface charge of the electron beam we get a jump of the electrical field over the electron beam. 1) jd = 0 (A/m); 2) jd = 0.25 (A/m); 3) jd = 0.5 (A/m); 4) jd = 1 (A/m). The electric field without the electron beam $V_0/R = 10^4$ (V/m). For jd = 1 (A/m) the beam ions are trapped by the spacecharge field of the electron beam.

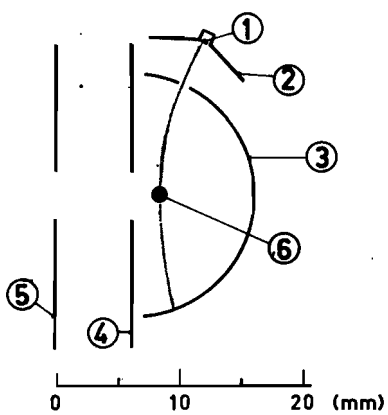

Figure 6.12. Schematic view of the ionizer. 1) filament (- 120 V); 2) Pierce electrode (- 145 V); 3) anode or ionizing chamber (+ 70 V); 4) extractor (+ 30 V); 5) entrance plate quadrupole mass filter (0 V); 6) molecular beam.

transported to the input of the time-of-flight multiscaling interface (section 6.7.1.).

6.6.1. Ionizer design

For a time-of-flight detector a fast response is necessary. An electron bombardment detector is well suited for this purpose. However, we have to take care that the space charge field of the electron beam does not create a potential well which could trap the beam ions and thus delay their extraction. For this reason the electron current is limited. In a simple model we investigate this limitation.

We consider two infinite parallel flat plates at a distance R with a potential difference V. An infinite plane electron beam of height d and current density j (A/m^2) is located between these plates. This electron sheet causes a surface charge $\sigma_{electron}$(C /m^2) given by

$$\sigma_{electron} = \frac{j\,d}{v_e} \tag{6.4}$$

with v_e the velocity of the electrons. This surface charge $\sigma_{electron}$ causes a jump δE of the electric field over the electron beam, given by

$$\delta E = \frac{\sigma_{electron}}{\varepsilon_o} \tag{6.5}$$

with ε_o the permittivity of vacuum. The velocity v_e of the electrons is fixed by the maximum in the ionization cross-section of all gases at 100 eV, and thus we use the surface current density jd(A/m) as parameter in this discussion.

In figure 6.11 we give the potential $V(x)$ between the two plates, with jd as parameter. The electric field without the electron beam is $V/R = 10^4$ V/m. The electron beam is centered on the molecular beam at $x = 0.2\ R$ and its height is $d = 0.2\ R$. The energy of the electrons is 100 eV. In the case of $jd = 1$ A/m the ions of the molecular beam are trapped. A situation providing a suitable extraction is the case of $jd = 0.25$ A/m. Substituting the practical dimensions $R = 10$ mm and $d = 2$ mm of the ionizer results in a limiting value $j = 0.125$ mA/mm^2

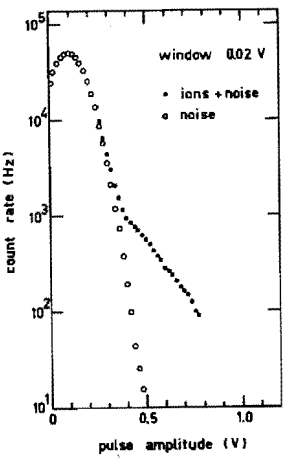

Figure 6.13. Pulse height spectrum of the output pulses of the electron multiplier. Solid points: pulses due to ions (mass number 18) and to noise. Open points: pulses due to noise. Switching the ionizer on and off does not influence the noise spectrum. The horizontal scale is 8.2 10^{-5} V per electron at the output of the multiplier.

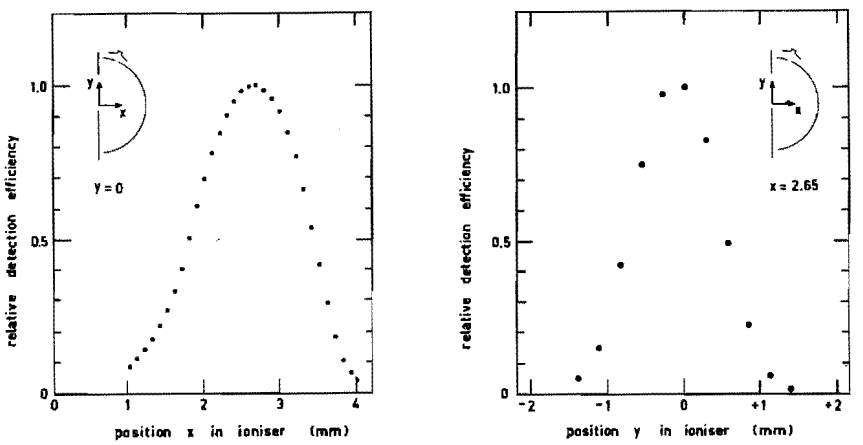

Figure 6.14. Spatial sensitivity of the ionizer, measured by scanning the whole detector assembly over the molecular beam with the aid of the adjustment micrometers. The molecular beam diameter was 0.2 mm. a) horizontal scan, perpendicular to the electron beam; b) vertical scan, along the electron beam.

of the current density. With an ionization length of 3 mm the total electron current is limited to 0.75 mA. Assuming an ionization cross-section of 3 10^{-20} m^2 (typical for Ar, N_2, O_2 at 100 eV), the ionization efficiency for molecules with v = 1000 m/s is then given by

$$\eta_i \text{ (1000 m/s)} = 1.0\ 10^{-4} \text{ ions/molecule} \qquad (6.6)$$

Another essential feature of a molecular beam ionizer is a sensitive volume which drops off rapidly outside the molecular beam, to minimize the count rate due to the residual gas.

6.6.2. Construction of the detector

In figure 6.12 the ionizer is shown. A Pierce type electron gun is used. The anode, i.e. the ionizer chamber, is cylindrical. The position of the molecular beam and typical electron trajectories are indicated. A positive potential between anode and extractor provides the extraction field for the beam ions. After leaving the ionizer chamber the ions are further excellerated by the extractor potential. Typical operating conditions are given in the figure caption.

The quadrupole mass filter consists of gold plated quartz rods, which are enclosed between two endplates with four accurately machined holes.

The electron multiplier is placed off axis. The ions are transported by a set of deflection plates between the mass filter and the electron multiplier. A fine grid in the lower deflection plate allows metastable molecules and photons to be transmitted without reaching the multiplier. An important source of low energy noise pulses is eliminated in this way (see figure 4.4 and 6.13).

6.6.3. Performance of the detector

In figure 6.13 two pulse height spectra of the output pulses of the detector are shown. The first spectrum is due to ions and noise; the second spectrum is only due to noise. This second spectrum is measured by tuning the mass filter to zero transmission, i.e. infinite resolution. Switching the ionizer off does not influence this second pulse height spectrum. In normal operating conditions the lower

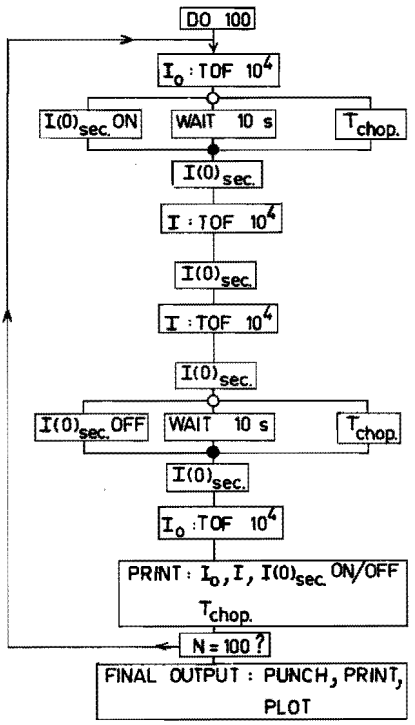

Figure 6.15. Flow diagram of a total cross-section measurement, consisting of 100 basic measuring cycles of 315 seconds each. An open circle indicates the parallel mode, a solid circle the serial mode of execution of the separate commands. I and I_0: TOF 10^4: indicates the analysis during 10^4 chopper periods of the attenuated and unattenuated primary beam, respectively; $I(0)_{sec}$: measurement of the secondary beam center-line intensity (the words ON and OFF indicate the switching of the secondary beam); T_{chop}: measurement of the chopper period; WAIT 10 s: indicates a pause of 10 seconds to allow the secondary beam to settle; PRINT: print-out on the teletype.

level is fixed at 440 mV (see figure 6.13).

The spatial sensitivity of the detector, i.e. the net result of the electron beam profile and the acceptance of the quadrupole mass filter, has been measured by scanning the detector assembly over the cross-section of the molecular beam, with the aid of the micrometers. Scans are made both in the horizontal and the vertical plane, i.e. perpendicular to the electron beam and along the electron beam. The results are given in the figures 6.14a and 6.14b. With these graphs the effective area for detection of residual gas molecules can now be calculated and is equal to (2.4 ± 0.4) mm^2.

The overall detection efficiency has been measured by using an effusive source (section 4.2.7), resulting in

$$\eta_o(\mathrm{Ar}) = 2\ 10^{-6} \text{ counts/molecule} \qquad (6.7)$$

for Ar molecules of 1000 m/s.

This value is much lower than the calculated ionization efficiency given in equation (6.6). We believe that the main reason is a poor transmission of the mass filter due to the closed construction of the endplates of the mass filter. This construction will be changed to investigate the effect.

6.7. Data acquisition with the PDP-11

The new time-of-flight machine is connected to the PDP-11 computer facility in the molecular beam group, as described in section 6.1.2. At the time of the scattering experiments described in chapter 7 the PDP performed the following tasks:

- accumulation of the time-of-flight spectra of the attenuated and the unattenuated primary beam with the time-of-flight multiscaling interface (section 6.7.1.);
- checking the intensity of the primary beam, by calculation of the increase of the count in a fixed time channel of the time-of-flight spectra of the attenuated and unattenuated primary beam;
- display of the time-of-flight spectra and the measuring routine;
- switching the secondary beam on and off (section 6.5);

- checking the center-line intensity of the secondary beam, by a read out of the ionization gauge storage detector (section 6.5);
- checking the chopper frequency.

The last three tasks are performed with the universal interfacing system.

The whole measuring routine is a sequence of basic ROSIE commands. A typical measuring time is 4.5 or 9 hours, consisting of 50 or 100 basic measuring cycles of the order of 300 seconds. A flow diagram of the basic measuring cycle used for the measurements in chapter 7 is given in figure 6.15. During a measurement the experimentalist only supervises the display and the periodic output of the teletype, consisting per measuring cycle of five numbers giving information on the checks mentioned above. The experimentalist also checks a number of parameters that are not yet controlled and/or supervised by the computer, e.g. the cryotemperature, detector voltages, information on the vacuum system, etc. At the end of a measurement, i.e. after 4.5 or 9 hours, the time-of-flight spectra are dumped on paper tape for further analysis on the B6700 central computer of the university.

Basic adjustments as a change of the primary beam temperature are then made manually by the experimentalist and a new measurement is started.

Fully automised measurements are rather dull, as the experimentalist has no real tasks to perform except for keeping awake. However automation inmensely increases the reliability of the data obtained.

Further automation is planned and will be finished in the near future. These extensions include a stepping motor controlled collimator (collimator 1 in figure 6.1) for automatic alignment of the primary beam, control of the secondary beam scanner with a stepping motor, a computer controlled variable frequency drive for the chopper motor and several ADC's and DAC's for controlling and checking a variety of parameters.

6.7.1. The time-of-flight multiscaling interface

The multiscaling interface has been designed and constructed by Geel (GEE 72, 73a, 73b). We give a short qualitative description of the principle of operation and give the specifications of the interface.

A block diagram of the interface is given in figure 6.16. The interface runs under computer control. The software device handler routine prepares a sweep, i.e. the analysis of one burst of molecules transmitted by the chopper, by loading the address register AREG with the address of the first channel and the channel count register CREG with the inverse of the number of channels. The channel time and the delay are set in the device status register SREG and then the start circuitry is enabled to receive a synchronization pulse, indicated with TRIGGER in figure 6.16. The synchronization pulse opens a gate for pulses from a 6.4 MHz quartz oscillator. After suitable scaling, according to the setting in SREG, this gives clock pulses with a period t_{ch} marking the boundaries of the time channels. The clock pulses are first counted by the delay scaler, thus determining a delay of a number of channels as given by SREG.

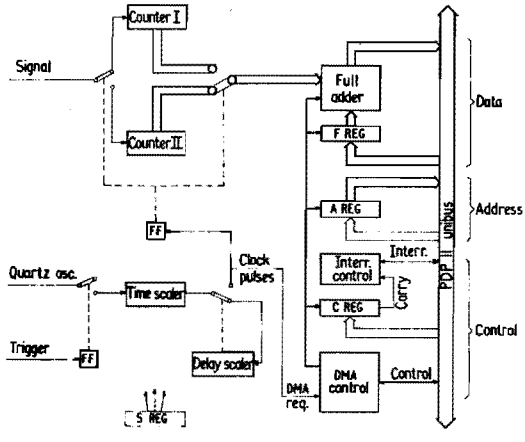

Figure 6.16. Block diagram of the time-of-flight multiscaling interface. The bold lines indicate the data transfer executed per time channel. (GEE 73).

Two identical registers are used to receive the SIGNAL pulses, each register functioning alternately as counter or as buffer. The data transfer runs parallel with the counting of the signal pulses. If during time channel k the signal pulses are counted in counter I, then counter II containing the number of signal pulses counted during time channel $(k - 1)$ is connected to the hardware full adder. The contents of counter II are added to the memory word corresponding to channel $(k - 1)$ with the aid of the DMA (Direct Memory Acces) and the RMW (Read-Modify-Write) facilities of the PDP-11 computer (PDP 70). Register AREG provides the memory address. The buffer register II is then cleared and the registers AREG and CREG are increased. These functions are all completed before the end of time channel k.

A carry from CREG indicates that the required number of channels has been reached. The clock pulses are stopped and an interrupt is requested at the highest priority level. The device handler routine gets control and checks if the next sweep should be started. If there are no objections the next sweep is prepared.

A double word of 16-bit core memory is reserved for each time channel. The interface only accumulates in the least significant word (LSW), the increase of the most significant word is done by the program. We only use 15 bits of the LSW for information (bits 0-14) and use bit 15 as an overflow bit. Overflow is indicated by a flip-flop which is reset at the beginning of each sweep and set by bit 15 of the full adder output. The state of this flip-flop is available in the status register SREG. The device handler routine checks this bit; if it is set it scans the array of LSW's. For each LSW where bit 15 is set, this bit is cleared and the corresponding MSW is incremented. The resulting representation of the count per time channel is 2^{15} x MSW + LSW.

The channel times available are given by

$$t_{ch} = 2^{p+1}\ 1.25\ \mu s \qquad p = 1\ ,\ \ldots\ ,\ 7 \tag{6.8}$$

The shortest channel time of 2.5 μs is equal to 16 oscillator periods. The number of channels given as delay after the synchronization pulse is

$$k_{delay} = 2^{q+1} - 1 \qquad q = 0, \ldots, 7 \tag{6.9}$$

resulting in a delay time

$$t_{delay} = k_{delay} \; t_{ch} \tag{6.10}$$

The shortest channel time of 2.5 µs is determined by the 2 µs required for the data transfer with a RMW cycle.

7. Total cross-section measurements

In this chapter we discuss the first total cross-section measurements with the new time-of-flight machine, for the systems Ar-Ar and Ar-Kr. In section 7.1. we calculated the corrections that have to be applied to the experimental data due to the finite angular resolution of the apparatus. In section 7.2. the influence of the finite velocity resolution on the experimental results is treated. In section 7.3. we discuss the two analysing schemes we have used to determine the positions of the glory extrema, and we present our experimental results. In section 7.4. we summarise our experimental data and compare them to other experimental results and to calculated results.

7.1. Angular resolution

Due to the finite angular resolution of the apparatus we also measure part of the differential cross-section, as already mentioned in section 2.3. and 3.2.. As a result equation (3.8) for the case of an ideal total cross-section measurement has to be modified for the description of the actual experiment.

The attenuation of the primary beam is described by

$$dI(x) = \frac{-\, I(x)\, J_2\, g}{v_1\, v_2}\, dx \int_{\Omega} (1 - \eta(\Theta,\Phi))\, \sigma_L(\Theta,\Phi)\, d\Omega \qquad (7.1)$$

with x the coordinate along the primary beam, $I(x)$ the primary beam intensity at position x , $\sigma_L(\Theta,\Phi)$ the differential cross-section in the L system and $\eta(\Theta,\Phi)$ the probability that a molecule scattered over an angle (Θ,Φ) is still detected. Integration over x results in

$$\ln \frac{I}{I_o} = -\, \xi Q_{exp} = -\, \xi \int_{\Omega} (1 - \eta(\Theta,\Phi))\, \sigma_L(\Theta,\Phi)\, d\Omega \qquad (7.2)$$

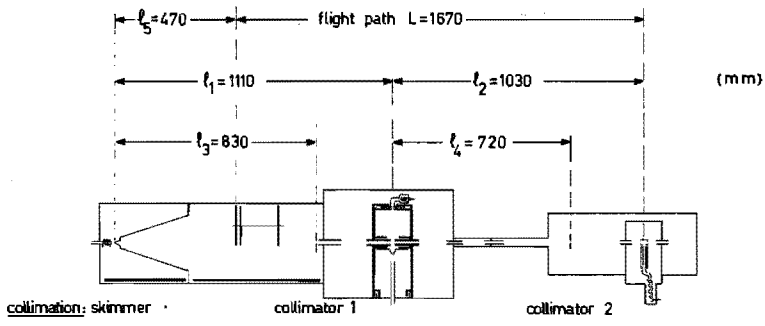

Figure 7.1. Schematic view of the primary beam geometry.

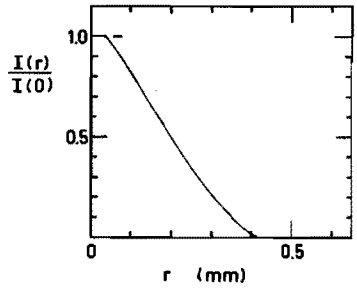

Figure 7.2. The profile of the primary beam in the plane of collimator 2. Dimensions of collimators: skimmer 0.3 mm diam.; collimator 1 0.2 mm diam.. Collimator 2 has a diameter of 0.5 mm, and thus only primary beam particles with $r \leq 0.25$ are detected.

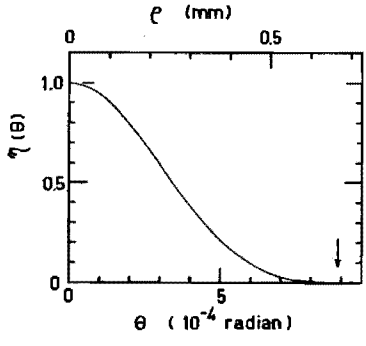

Figure 7.3. The angular resolution function $\eta(\Theta)$, calculated with the primary beam profile in figure 7.2. Dimensions of collimators: skimmer 0.3 mm diam.; collimator 1 0.2 mm diam.; collimator 2 0.5 mm diam..

with $\xi = \frac{J_2 \, l \, g}{v_1 v_2}$.

With equation (2.5) and (3.8) this can also be written as

$$Q_{exp} = Q - \Delta Q \tag{7.3}$$

with $\Delta Q = \int_{\Omega} \eta(\Theta,\Phi) \; \sigma_L(\Theta,\Phi) \; d\Omega$.

For the calculation of ΔQ we need the functions $\eta(\Theta,\Phi)$ and $\sigma_L(\Theta,\Phi)$. We first discuss the angular resolution function $\eta(\Theta,\Phi)$.

The angular resolution function depends only on the primary beam geometry. The source and the first collimator give an intensity profile $I_o(\vec{r})$ in the plane of the second collimator. Scattering over an angle (Θ,Φ) displaces this beam profile over $\vec{\rho}$,with $|\vec{\rho}| = l_{coll}\Theta$ and a polar angle Φ. The length l_{coll} is the distance from the scattering center to the second collimator. The function $\eta(\Theta,\Phi)$ is then given by (BUS 66, KUS 64)

$$\eta(\Theta,\Phi) = \frac{\int_{A_{coll}} I_o(\vec{r} - \vec{\rho}) \; d\vec{r}}{\int_{A_{coll}} I_o(\vec{r}) \; d\vec{r}} \tag{7.4}$$

where the integration is performed over the open area A_{coll} of the second collimator. In equation (7.4) we have assumed that each particle passing the last collimator is detected with an efficiency independent of the direction in which it travels.

As our primary beam geometry has cylindrical symmetry, the angular resolution function $\eta(\Theta,\Phi)$ will depend only on Θ , and in the following equations will be written as $\eta(\Theta)$.

In the actual calculation of $I_o(\vec{r})$ and $\eta(\Theta)$ we have assumed that the skimmer area of the primary beam source has a uniform intensity distribution and is the actual beam source. This is a reasonable assumption if we consider the nozzle diameter used (section 6.2.) and its corresponding virtual soruce radius (section 5.1.3.).

In figure 7.1 the beam geometry is given. In figure 7.2 the calculated beam profile $I_o(r)/I_o(0)$ is given. In figure 7.3 the resulting

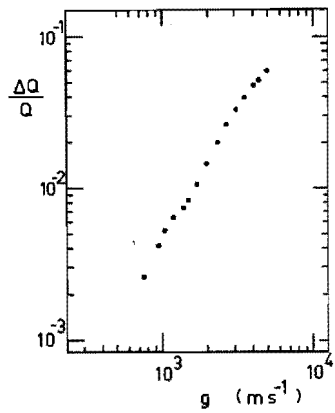

Figure 7.4. The relative angular resolution correction ΔQ/Q of the total cross-section Q for Ar-Ar.

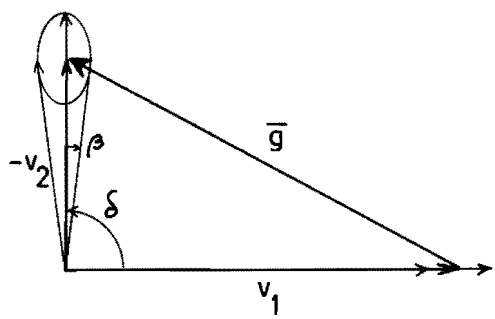

Figure 7.5. Newton diagram of the scattering experiment.

angular resolution function $\eta(\Theta)$ is given, calculated with equation (7.4).

The function $\eta(\Theta)$ can also be measured experimentally, by scanning collimator 1 (figure 7.1). The experimental results are in good agreement with the calculated values (VER 75).

The differential cross-section in the L system is given by

$$\sigma_L(\Theta,\Phi) = \sigma(\theta(\Theta,\Phi)) \quad \left|\frac{d\omega}{d\Omega}\right| \tag{7.5}$$

with θ and ω the CM scattering angle and the CM solid angle respectively and $\left|\frac{d\omega}{d\Omega}\right|$ the Jacobian of the transformation of the CM system to the L system. This transformation is given by (the beams are crossed at 90°)(PAU 65)

$$\theta = \Theta \frac{m_1}{\mu} \left(1 - \left(\frac{v_2}{g}\right)^2 \sin^2 \phi\right)^{\frac{1}{2}} \tag{7.6}$$

$$\left|\frac{d\omega}{d\Omega}\right| = \frac{m_1^2 v_1}{\mu^2 g}$$

In our case the angular resolution function $\eta(\Theta)$ is limited to angles that, after transformation to the CM system, are small compared with $k^{-1} Q^{-\frac{1}{2}}$ (equation (2.28) and (2.29)) and we can neglect the angular dependence of $\sigma(\theta)$ and only use $\sigma(0)$ to calculate ΔQ with equation (7.3).

Using equation (2.17) for $\sigma(0)$ the relative angular resolution correction $\Delta Q/Q$ is given by

$$\left(\frac{\Delta Q}{Q}\right) = \frac{1}{8\pi} \left\{1 + \tan^2 \frac{\pi}{(s-1)}\right\} \frac{m_1^2 v_1 g Q}{\hbar^2} \int_0^{\pi} \Theta\, \eta(\Theta)\, d\Theta \tag{7.7}$$

By using equation (2.18) for Q with $s = 6$ and assuming $v_1 = g$ the relative correction $\Delta Q/Q$ is proportional to $g^{8/5}$. For the angular resolution function $\eta(\Theta)$ (figure 7.3) of the primary beam geometry, as used in our scattering experiments, the integral in (7.7) is given by

$$\int_0^{\pi} \Theta \, \eta(\Theta) \, d\Theta = 7.9 \; 10^{-8} \qquad (7.8)$$

With this number we can calculate the angular resolution correction for all scattering partners with equation (7.7), provided that $\Delta Q/Q < 0.03$.

By using the mass number M_1 of the primary beam particles and using the numerical values of h and equation (7.8), we can write equation (7.7) as

$$\left(\frac{\Delta Q}{Q} \right) = 7.8 \; 10^{5} \left(1 + \tan^2 \frac{\pi}{s-1} \right) M_1^{\,2} \, g \, v_1 \, Q \qquad (7.9)$$

For $s = 6$ the function $(1 + \tan^2 \pi/(s-1)) = 1.53$. In figure 7.4 the relative correction $\Delta Q/Q$ is given for the case of Ar-Ar, calculated with an effective power $s = 6.7$ of the attractive potential (BRE 73) and by using Q values calculated with the BFW potential (BRE 73). The Q values used include the glory contribution, which is equivalent to using equation (2.27) for the differential cross-section and neglecting the phase difference of the glory oscillations in Q and $\sigma(0)$. The overall accuracy of an angular resolution correction is of the order of ten percent (e.g. using $s = 6$ instead of $s = 6.7$ increases the ratio $\Delta Q/Q$ by 13% (see figure 2.2)).

7.2. Velocity resolution

The relative velocity g is determined by the primary beam velocity $\vec{v}_1$ and the secondary beam velocity $\vec{v}_2$, resulting in (figure 7.5)

$$g = (v_1^{\,2} + v_2^{\,2} - 2 v_1 v_2 \cos(\delta - \beta))^{\frac{1}{2}} \qquad (7.10)$$

The beams are crossed at an angle $\delta = \pi/2$.

The primary beam velocity $v_1(k)$ as a function of the number k of the time channel is given by

$$v_1(k) = \frac{L}{t_{fl}(k)} \qquad (7.11)$$

with $t_{fl}(k) = (k - \tfrac{1}{2})\, t_{ch} + t_o$

as already given in equation (4.8). For the new time-of-flight machine the effective delay time t_o is given by

$$t_o = -0.025T - 2\mu s + t_{delay} \qquad (7.12)$$

with T the chopper period and t_{delay} the delay time of the time-of-flight multiscaling interface (equation (6.10)). The term - 2μs is the net result of a small delay of 8μs in the synchronization amplifier and the flight time of 10μs of the ions in the quadrupole detector. The term - $0.025T$ is the off-set of the synchronization pulse (see 6.4.1.).

The three main contributions to the distribution function of relative velocities g are: the finite velocity resolution of the primary beam, the velocity distribution of the secondary beam and the opening angle of the secondary beam (figure 7.5). As we present our experimental data in section 7.3. as a function of the inverse relative velocity g^{-1}, we calculate the RMS width of the resulting distributions in g^{-1} for all three contributions.

- The resolution of the primary beam velocity depends on the open time of the chopper t_b, the width of the primary beam at the first chopper disc, the width t_{ch} of a time channel and the length of the ionizing region with respect to the flight path L. In all practical cases the only important contribution is of the open time t_b of the chopper. For the scattering experiments the broad chopper slit II was used with T = 7.1 ms, resulting in t_b = 142 μs(section 6.4). The resulting distribution function of primary beam velocities is rectangular with full width $\Delta v_1 = 8.5\ 10^{-5}\ v_1^2$ m s^{-1}. The RMS width of the resulting distribution of inverse relative velocities g^{-1} is given by

$$\sigma_{v_1}(g^{-1}) = \left(\frac{v_1}{g}\right)^3 2.5\ 10^{-5}\ m^{-1}\ s \qquad (7.13)$$

- The velocity distribution of the secondary beam is given by equation (5.11) with u = 540 m/s and $\alpha_{\prime\prime}$ = 27 m/s for an Ar secondary beam. The velocity u is an experimentally determined value, and shows that the nozzle is slightly under room temperature (T_{nozzle} = 282 K). The value of $\alpha_{\prime\prime}$ has been calculated. The RMS width of the resulting distribution in g^{-1} is given by

$$\sigma_{v_2}(g^{-1}) = \left(\frac{v_2}{g}\right)^3 6.6\ 10^{-5}\ m^{-1}\ s \qquad (7.14)$$

- The width of the skimmer slit of the secondary beam was 1.8 mm with a nozzle-skimmer distance of 18 mm, resulting in an opening angle of 0.1 radian, i.e. $-0.05 \leq \beta \leq +0.05$. The effect of the virtual source radius on the beam profile can be neglected in first order (see 5.1.3.). The RMS width of the resulting distribution in g^{-1} is given by

$$\sigma_{\beta}(g^{-1}) = \left(\frac{v_1 v_2^2}{g^3}\right) 5.4\ 10^{-5}\ m^{-1}\ s \qquad (7.15)$$

With the three distribution functions for v_1, v_2 and β we have also treated the convolution of the function $\xi(v_1, v_2, \beta)Q_{attr}$ (equation (3.8) and equation (2.18) with s= 6) and the function $\xi(v_1, v_2, \beta)Q_{gl}$ (equation (3.8) and (2.22))with the method of second moments (VER 75). This calculation shows that for Ar-Ar a correction has to be applied to the measured value of Q_{attr}, which is equal to -0.15% at g = 1500 m/s. The damping of the amplitude of the glory undulations for Ar-Ar is 5% for the N = 2.5 minimum and 3% for the N = 2 maximum.

7.3. Analysis of the results

In this section we discuss the analysis of the first eight measuring runs with the new time-of-flight machine. Six runs have been done for the Ar-Ar system; two runs for the Ar-Kr system. In all cases argon was used as the primary beam. In table 7.1 we give information

Table 7.1 Characteristic experimental conditions of the scattering experiments.

system	measure-ment number	date/ number	total measuring time (hours)	signal-to-background ratio	count rate (kHz)	attenuation ξQ
Ar-Ar	1	300375/00	9	5.1	10	0.18
Ar-Ar	2	310375/00	9	2.4	6.9	0.16
Ar-Ar	3	010475/02	4.5	2.2	6.5	0.15
Ar-Ar	4	240475/00	4.5	17.6	31	0.20
Ar-Ar	5	240475/02	4.5	16.0	35	0.20
Ar-Ar	6	240475/04	9	15.3	34	0.20
Ar-Kr	7	010475/00	4.5	4.7	11.4	0.14
Ar-Kr	8	310375/02	4.5	2.6	7.0	0.13

on the typical experimental circumstances: the maximum count rate of the primary beam signal and the signal-to-background ratio (both in the maximum of the time-of-flight spectrum), the average attenuation, the total measuring time and for bookkeeping reasons the date and serial number of the measurement.

A measuring run results in two time-of-flight spectra $N(k)$ and $N_o(k)$ of the attenuated and unattenuated primary beam respectively, consisting of the signal $I(k)$ and $I_o(k)$ superimposed on the background $B(k)$ and $B_o(k)$ respectively, as given by

$$N(k) = I(k) + B(k) \tag{7.16}$$

The statistical error in $N(k)$ is given by $(N(k))^{\frac{1}{2}}$. The background levels $\overline{B}$ and $\overline{B}_o$ respectively are determined by averaging over a large number of channels (beyond the cut-off of the second disc) and the attenuated and unatttenuated signal $I(k)$ and $I_o(k)$ respectively are retrieved by subtracting $\overline{B}$ and $\overline{B}_o$ from the contents of the time channels. The measured value of the total cross-section Q_{exp} as a function of k is determined according to equation (7.2), resulting in

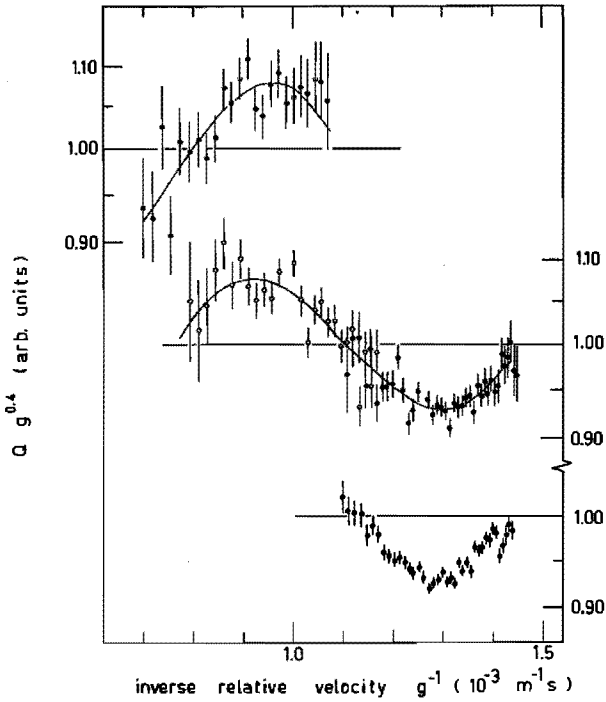

Figure 7.6. Experimental results for the total cross-section for Ar-Ar as a function of the inverse relative velocity g^{-1}. *The solid points are the function* $Q_{exp}\, g^{0.4}$, *with an error bar indicating the statistical error. The solid line is the smoothed function* $\hat{Q}_{exp}\, g^{0.4}$. *Top: measurement no. 3. Middle (left): no. 2. Middle (right): no.1. Bottom: no. 6. The vertical scale is logarithmic.*

$$Q_{exp}(k) = \frac{v_1(k)}{g(k)} \ln \left\{ \frac{I(k)}{I_o(k)} \right\} \qquad (7.17)$$

The primary beam velocity $v_1(k)$ and the relative velocity $g(k)$ are determined by equation (7.10) and (7.11), and we now have Q_{exp} as a function of g.

Table 7.2 Experimental results for the position g_N(m/s) and the magnitude of the glory extrema for the Ar-Ar system.

measurement number	$N = 2.5$		$N = 2$	
	method I (parabola)	method II (Fourier)	method I (parabola)	method II (Fourier)
1	769 ± 4	771		
2			1090 ± 25	1080
3			1011 ± 36	1046
4	778 ± 2	778		
5	779 ± 2	779		
6	776 ± 2	777		

1/2 $\dfrac{\{\tilde{Q}_{exp}\, g^{0.4}\}_{N=2}}{\{\tilde{Q}_{exp}\, g^{0.4}\}_{N=2.5}} = 1.163$ (method II)

To find the true value of the total cross-section we have to correct Q_{exp} with the angular resolution correction (equation (7.3) and (7.9)) and the velocity resolution correction (discussed in section 7.1.). In the following analysis these corrections have not yet been applied, and we have analysed the uncorrected measured values Q_{exp}. However, concerning the positions of the glory extrema the influence of these corrections is negligible. Concerning the amplitude the effect is taken in account in 7.4.

Following the convention in the field of total cross-section measurements we consider the extrema of the function $Q\, g^{0.4}$. To determine the positions of the extrema in the function $Q_{exp}\, g^{0.4}$ we have used two different analysing schemes.

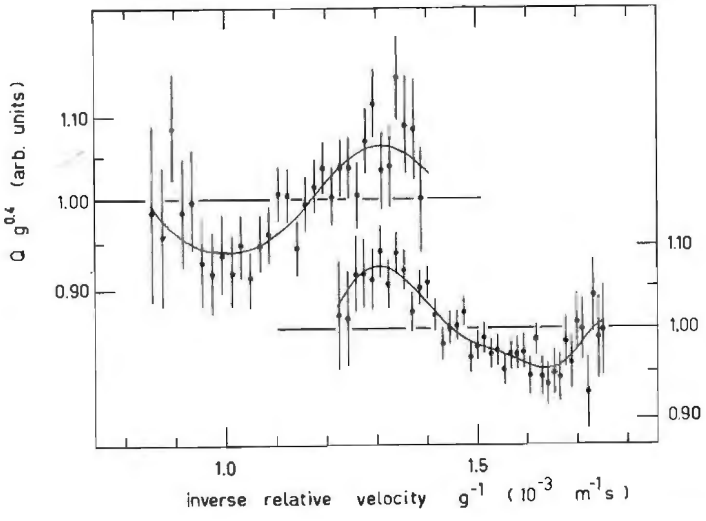

Figure 7.7. Experimental results for the total cross-section for Ar-Kr as a function of the inverse relative velocity g^{-1}. *The solid points are the function* $Q_{exp}\, g^{0.4}$, *with an error bar indicating the statistical error. The solid line is the smoothed* $Q_{exp}\, g^{0.4}$. *Top: measurement no. 8. Bottom: no. 7. The vertical scale is logarithmic.*

The first scheme (method I) is very straightforward. With a weighted least squares method we have fitted a parabola through the experimental function $Q_{exp}\, g^{0.4}$ as a function of the inverse relative velocity g^{-1}. As in this representation the glory oscillations are in first order well represented by a cosine (equation (2.22)) the parabola is a good approximation. The position of the extremum is determined from the parabola, together with the statistical error determined from the errors in the data points $Q_{exp}\, g^{0.4}$.

The second scheme (method II) of determining the positions of the extrema in $Q_{exp}\, g^{0.4}$ works as follows. From the time-of-flight spectra $N(k)$ and $N_o(k)$ we calculate the square root $(N(k))^{\frac{1}{2}}$ and $(N_o(k))^{\frac{1}{2}}$. In this representation all time channels have the same statistical error 0.5 and thus the same weight. We calculate the Fourier spectrum of

Table 7.3 Experimental results for the position g_N(m/s) and the magnitude of the glory extrema for the Ar-Kr system.

	N = 3.5		N = 3		N = 2.5	
measure-ment number	method I (parabola)	method II (Fourier)	method I (parabola)	method II (Fourier)	method I (parabola)	method II (Fourier)
7	616 ± 9	617	902 ± 120	772		
8			762 ± 8	762	983 ± 10	987
7	$\frac{\{\tilde{Q}_{exp}\, g^{0.4}\}_{N=3}}{\{\tilde{Q}_{exp}\, g^{0.4}\}_{N=3.5}}$ =	= 1.111 (method II)				
8	$\frac{\{\tilde{Q}_{exp}\, g^{0.4}\}_{N=3}}{\{\tilde{Q}_{exp}\, g^{0.4}\}_{N=2.5}}$	= 1.129 (method II)				

the spectra $(N(k))^{\frac{1}{2}}$ and $(N_o(k))^{\frac{1}{2}}$. By comparing the Fourier coefficients with the expected value for statistical noise and by considering the autocorrelation of the residu we determine where we can cut-off the high frequency Fourier coefficients. Typically the lowest 17 to 21 Fourier coefficients (of the 150 available) contain all information. With these remaining low frequency Fourier functions we calculate the smoothed spectra $(\tilde{N}(k))^{\frac{1}{2}}$ and $(\tilde{N}_o(k))^{\frac{1}{2}}$ and by squaring these quantities we obtain the smoothed time-of-flight spectra $\tilde{N}(k)$ and $\tilde{N}_o(k)$ of the attenuated and unattenuated primary beam. In the same way as given previously the function $\tilde{Q}_{exp}\, g^{0.4}$ is calculated. The positions of the extrema in the smoothed function $\tilde{Q}_{exp}\, g^{0.4}$ are then determined by directly looking at this function.

In figure 7.6 the experimental results for Ar-Ar are given. The points are $Q_{exp}\, g^{0.4}$ with an error bar indicating the statistical error due to the statistical error in the time-of-flight spectra. The solid line is the smoothed function $\tilde{Q}_{exp}\, g^{0.4}$. The middle curve in this figure is the result of two measuring runs. They are scaled to each

other by scaling the smoothed results. For reasons of clarity the upper and the lower measurement are not scaled to the measurements in the middle, and the smoothed curve of the lower measurements has been omitted.

In table 7.2 the extrema positions are given, as calculated with both analysing schemes, method I and method II. We observe that both methods give practically the same results.

The ratio's given for the magnitude of the glory extrema are determined from the smoothed function $\tilde{Q}_{exp}\, g^{0.4}$.

In figure 7.7 the results of the two measuring runs for Ar-Kr are given. The points are the function $Q_{exp}\, g^{0.4}$ with an error bar indicating the statistical error. The solid line is the smoothed function $\tilde{Q}_{exp}\, g^{0.4}$. For the low velocity measurement the cut-off in the Fourier spectrum has been done at a too high frequency, resulting in the "waviness" in the $N = 3.5$ minimum. This disappears when choosing the correct cut-off. The results of method II in table 7.3 are determined with the correct cut-off.

The results for the extrema positions for the Ar-Kr system are given in table 7.3. Again we see a good agreement of both analysing methods. For measurement 7 the position of the $N = 3$ maximum is determined far more accurate with the second analysing scheme (method II) than with the parabola fit (method I). This can be understood if we realise that method II takes in account all data points and method I only uses a limited number of points. However, the results of method I do coincide with those of method II within the statistical error given by the weighted least squares parabola fit procedure. The results of method II for the position of the $N = 3$ maximum of the measurements 7 and 8 are in good agreement.

The ratio's given for the magnitude of the glory extrema are determined from the smoothed function $\tilde{Q}_{exp}\, g^{0.4}$ (with the correct cut-off).

Table 7.4 Comparison of our results for the magnitude and position g_N(m/s) of the glory extrema for Ar-Ar with other experimental results and calculated results.

	Experimental results		Calculated results b)		
Glory extremum N	This work	Bredewout a)	BFW	MS	MSV III
2.5	778 ± 5	802 ± 25	775	770	755
2	1060 ± 30	1090 ± 30	1065	1065	1030

This work	$\frac{(\tilde{Q}_{exp}\, g^{0.4})_{N=2}}{(\tilde{Q}_{exp}\, g^{0.4})_{N=2.5}} = 1.163$	BFW potential	$\frac{(Q\, g^{0.4})_{N=2}}{(Q\, g^{0.4})_{N=2.5}} = 1.181$
		MSV III potential	$\frac{(Q\, g^{0.4})_{N=2}}{(Q\, g^{0.4})_{N=2.5}} = 1.168$

a) Bredewout (BRE 73)

b) All calculations are due to Bredewout (BRE 73)

7.4. Discussion of the results

In table 7.4 we give a summary of our results for Ar-Ar, in comparison with the experimental results of Bredewout (BRE 73) and the calculated values (BRE 73) for the three "best" potentials mentioned in section 3.1. The errors given for our results are a combination of the statistical errors given in section 7.3. and estimated errors in the absolute calibration of the primary beam velocity and the secondary beam velocity. We see a very good agreement of our data with the results calculated with the BFW potential. Our experimental values are significantly higher than the predictions with the MSV III potential, and slightly higher than the results of the MS potential.

Table 7.5 Comparison of our results for the magnitude and the position g_N (m/s) of the glory extrema for Ar-Kr with other experimental results and calculated results.

	Experimental results		Calculated results
Glory extremum N	This work	Bredewout a)	Barker pot. b)
3.5	616 ± 11		623
3	767 ± 10	755 ± 20	772
2.5	983 ± 12	967 ± 20	967

$$\frac{(\tilde{Q}_{exp}\, g^{0.4})_{N=3}}{(\tilde{Q}_{exp}\, g^{0.4})_{N=3.5}} = 1.111 \qquad \frac{(Q\, g^{0.4})_{N=3}}{(Q\, g^{0.4})_{N=3.5}} = 1.113$$

$$\frac{(\tilde{Q}_{exp}\, g^{0.4})_{N=3}}{(\tilde{Q}_{exp}\, g^{0.4})_{=2.5}} = 1.129 \qquad \frac{(Q\, g^{0.4})_{N=3}}{(Q\, g^{0.4})_{N=2.5}} = 1.135$$

a) Bredewout (BRE 73)

b) Calculations due to Bredewout (BRE 73) with an unpublished potential of Barker.

Within their error the experimental results of Bredewout (BRE 73) coincide with our data.

The preference for the BFW (and the MS) potential can be understood qualitatively. The positions of the glory extrema are sensitive to the shape of the potential well, and specifically in this region the BFW potential is more flexible than the MSV III potential and thus can better fit the "true" shape of the potential.

The experimental value of the amplitude of the $N = 2.5$ to $N = 2$ glory oscillation is in good agreement with the value calculated with the BFW potential, if we take in account the calculated damping of the

amplitude of this glory oscillation of 8% (see section 7.2) and apply the angular resolution correction (figure 7.4) which increases the ratio given by 0.5%. We then find

$$\left\{ \frac{(\bar{Q}_{exp}\, g^{0.4})_{N=2}}{(\bar{Q}_{exp}\, g^{0.4})_{N=2.5}} \right\}_{corrected} = 1.182$$

For Ar-Kr our experimental results are summarised in table 7.5 and compared to the experimental results of Bredewout (BRE 73) and to calculated results for an unpublished potential of Barker (BRE 73). We see a fair agreement of our data with the predictions of the Barker potential. Within their errors the experimental results of Bredewout (BRE 73) coincide with our data.

8. Conclusions

In this work it has been shown that the time-of-flight method can be developed into an accurate and reliable method for the analysis of the velocity distribution of molecular beams. Attractive features of the time-of-flight method are:

- calibration of the flight-time scale with an accuracy of 0.2% is achievable. With careful design this calibration is independent of the alignment of the chopper and the beam;
- a high velocity resolution, of the order of 0.5% (as necessary for the research on supersonic beam sources) is readily achievable;
- flexibility in choosing the velocity resolution;
- simultaneous analysis of the whole velocity distribution eliminates drift and fluctuations of the apparatus;
- automation of the experiments is readily achievable;
- time-of-flight spectra are an ideal input for numerical analysing schemes.

For the research on molecular beam sources the time-of-flight method is ideally suited. In a short time a large number of velocity distributions can be measured as a function of the source parameters such as pressure, temperature, angle, etc., resulting in a wealth of experimental information.

Concerning the results of the first scattering experiments we can conclude that the accuracy in the determination of the positions of the glory extrema is sufficient to distinguish between different potentials, even in the case of Ar-Ar where three nearly equivalent potentials are available. The high resolution in the relative velocity allows us to take in account the amplitude of the glory oscillations to help to distinguish between different potentials.

All scattering experiments described in this thesis are the result of five measuring days. The prospects for the future of the scattering experiments look promising.

References

ALC 69a Alcalay, J.A., and Knuth, E.L., Rev. Sci.Instr. 40(1969)438
ALC 69b Alcalay, J.A., and Knuth, E.L., Rev. Sci.Instr. 40(1969)1652
ALC 70 Alcalay, J.A., and Knuth, E.L., Rev. Sci.Instr. 41(1970)399
AND 65 Anderson, J.B., and Fenn, J.B., Phys.Fluids 8(1965)780
AND 74 Andres, R.P., private communication
ANG 72 Angel, G.C., and Giles, R.A., J.Phys. B5(1972)50

BAR 68 Barker, J.A., and Pompe, A., Austr.J.Chem. 21(1968)1683
BAR 71 Barker, J.A., Fisher, R.A., and Watts, R.O., Mol.Phys. 21(1971)657
BAR 71a Barker, J.A., Bobetic, M.V., and Pompe, A., Mol.Phys. 20(1971)347
BAR 74 Barker, J.A., Report R.J.1409(21714)IBM Research Laboratory, San Jose, California, 1974.
BEC 56 Becker, E.W., and Henkes, W., Z.f.Phys. 146(1956)320
BEC 61 Becker, G., Z.Phys. 162(1961)290
BEC 70 Beck, D., Proceedings of the Int.School of Physics "Enrico Fermi" Course XLIV (ed. Ch.Schlier), Academic Press, New York, 1970
BER 62 Berkling, K., Helbing, R., Kramer, K., Pauly, H., Schlier, Ch., and Toschek, P., Z.Angew.Phys. 166(1962)406
BER 65 Berman, A.S., J.Appl.Phys. 36(1965)3356
BER 66 Bernstein, R.B., in Advances in Chemical Physics, vol. X (ed. J. Ross), Wiley, New York, 1966
BER 73 Bernstein, R.B., and La Budde, R.A., J.Chem.Phys. 58(1073)1109
BER 73a Berceanu, I., and Ignatovich, I.V., Vacuum 23(1973)441
BEIJ71 Beijerinck, H.C.W., Geel, J., and Verster, N.F., Abstract of Papers of VII ICPEAC (ed.L.M.Branscomb),North Holland Press, Amsterdam, (1971)1007
BEIJ73 Beijerinck, H.C.W., and Verster, N.F., Vacuum 23(1973)133
BEIJ74 Beijerinck, H.C.W., Habets, A.H.M., Sessink, B.W.L.M., and Verster, N.F., J.Phys.E.:Sci.Instr. 7(1974)639
BEIJ74a Beijerinck, H.C.W., Moonen, R.G.J.M., and Verster, N.F., J. Phys.E. 7(1974)31
BEIJ75 Beijerinck, H.C.W., Stevens, M.P.J.M., and Verster, N.F., (to be published, section 5.3)
BEIJ75a Beijerinck, H.C.W., and Verster, N.F., J.Appl.Phys. 46(1975) 2083
BLE 74 Blechschmidt, D., J.Vac.Sci.Techn. 11(1974)570
BOB 70 Bobetic, M.V., and Barker, J.A., Phys.Rev. B2(1970)4169
BRE 73 Bredewout, J.W., Thesis, University of Leiden, 1973
BUC 72 Buck, U., J.Chem.Phys. 57(1972)578
BUC 74 Buck, U., Pauly, H., Pust, D., and Schlensener, J.H., Rarefied Gas Dynamics (ed. M.Becker and M.Fiebig) DFVLR Press, Porz-Wahn (1974)C-10
BUC 74a Buck, U., in "Molecular Beams" (ed.K.Lawley), Wiley, New York, 1974
BUS 66 Von Busch, F., Z.f.Phys. 193(1966)412
BUS 67 Von Busch, F., Strunck, H.J., and Schlier, Ch.,Z.f.Phys. 199(1967)518

CAN 71 Cantini, P., Dondi, M.G., and Torello, F., Z.f.Naturf. 26a(1971)1634
CAR 63 Carlson, K.D., Gilles, P.W., and Thorn, R.J., J.Chem.Phys. 38(1963)2725
CAV 70 Cavallini, M., Callinaro, G., Meneghetti, L., Scoles, A., and Valbusa, V., Chem.Phys.Letters 7(1970)303
CAV 71 Cavallini, M., Dondi, M.A., Scoles, A., and Valbusa, V., Proceedings 3rd Symp.Int.sur les Jets Mol. (Cannes) 1971
CLA 28 Clausing, P., Thesis, University of Leiden,(1928)
CLA 29 Clausing, P., Physica 9(1929)65
CLA 30 Clausing, P., Z.Phys. 66(1930)471
CLA 32 Clausing, P., Ann. Physik 12(1932)961
COL Collimated Hole Structures, Brunswick Corporation Technical Products Division, One Brunswick Plaza, Skokie, Ill. 60076

DAV 60 Davis, D.H., J.Appl.Phys. 31(1960)1169
DAV 66 Davies, W.D.T., Control 10(1966)302
DAV 73 David, R., Faubel, M., and Toennies, J.P., Chem.Phys.Letters 18(1973)87
DUR 63 Düren, R., and Pauly, H., Z.f.Phys. 175(1963)227

FIS 72 Fisher, R.A., and Watts, R.O., Mol.Phys. 23(1972)1051

HAB 73 Habets, A.H.M., Beijerinck, H.C.W., and Verster, N.F., Proceedings IV Symp.Int. sur les Jets Mol. (Cannes) 1973
HAB 74 Habets, A.H.M., Beijerinck, H.C.W., and Verster, N.F., Rarefied Gas Dynamics (ed. M.Becker and M.Fiebig) DFVLR Press, Porz-Wahn (1974)B-6
HAB 75 Habets, A.H.M., private communication
HAB 75a Habets, A.H.M., Verster, N.F., and Vlimmeren, Q.A.G. van, Rev.Sci.Instr. 46(1975)613
HAG 68 Hagena, O.F., and Varma, A.K., Rev.Sci.Instr. 39(1968)47
HAG 70 Hagena, O.F., Rev.Sci.Instr. 41(1970)893
HAN 60 Hanes, G.R., J.Appl.Phys. 31(1960)2171
HEL 66 Helbing, R., Thesis, University of Bonn (1966)
HEL 67 Helmer, J.C., J.Vac.Sci.Technol. 4(1967)360
HEL 67a Helmer, J.C., J.Vac.Sci.Technol. 4(1967)179
HIR 67 "Intermolecular forces" Adv.Chem.Phys. XII (ed.J.O. Hirschfelder) Wiley, New York, 1967
HIR 71 Hirschy, V.L. and Aldridge, J.P., Rev.Sci.Instr. 42(1971)381
HOS 60 Hostettler, H.U., and Bernstein, R.B., Rev.Sci.Instr. 31(1960)872
HEW Hewlett Packard Calculator 9100 B and Plotter 9125 A

GEE 72a Geel, J., Mol.Phys.Group, Rep. NO-72-2, Eindhoven University of Technology, 1972
GEE 72 Geel, J., Mol.Phys.Group, Rep. NO-72-7, Eindhoven University of Technology, 1972
GEE 73 Geel, J., Verster, N.F., and Beijerinck, H.C.W., Book of Abstracts of the VIII ICPEAC (ed.B.C.Cobic and M.V.Kurepa) Belgrade (1973)901
GEE 73a Geel, J., and Verster, N.F., J.Phys.E.:Sci.Instr. 6(1973)644

GEE 73b Geel, J., Verster, N.F., and Beijerinck, H.C.W., Book of Abstracts of the VIII ICPEAC (ed. B.C.Cobic and M.V.Kurepa) Belgrade (1973)899
GIB 73 Gibbons, T.G., Klein, M.L., and Murphy, R.G., Chem.Phys. Letters 18(1973)325
GIO 60 Giordmaine, J.A.,and Wang, T.C., J.Appl.Phys. 31(1960)463
GUN 57 Günther, K.G., Z.Angew. Phys. 9(1957)550

IVA 63 Ivanov, B.S. and Troitski, V.S., Sov.Phys.-Tech.Phys. 8(1963)365

JOH 66 Johnson, J.C., Stair Jr., A.T., and Pritchard, J.L., J.Appl. Phys. 37(1966)1551
JON 69 Jones, R.H., Olander, D.R. and Kruger, V., J.Appl. Phys. 40(1969)4641

KLE 73 Klein, M.L. and Barker, J.A., Phys.Rev. B7(1973)4707
KNU 9a Knudsen, M., Ann. Physik 28(1909)75
KNU 9b Knudsen, M., Ann. Physik 28(1909)999
KOF 48 Kofsky, I.L., and Levinstein, H., Phys.Rev. 74(1948)500
KUS 64 Kusch, P., J.Chem.Phys. 40(1964)1

LAN 60 Landau, L.D., and Livshitz, E.M., "Mechanics", Pergamon Press, London, 1960
LAN 66 Lanczos, C., "The variational principles of mechanics", University of Toronto Press, Toronto, 1966
LAN 67 Landau, L.D.,and Livshitz, E.M., "Mechanique quantitique", Editions MIR, Moscou, 1967
LEM 70 Lempert, G.D., Ph.D. Thesis, University College, London 1970
LEM 71 Lempert, G.D., Corrigan, S.J.B., and Wilson, J.F., Chem.Phys. Letters 8(1971)67
LIE 60 Liepmann, H.W., J.Fluid Mech. 21(1960)21
LIV 71 Livshitz, A.I., Metter, I.M. and Rikenglanz, L.E., Sov.Phys.-Tech.Phys. 16(1971)276
LOW 73 Lowes, P., Mol.Phys.Group, Rep. NO-73-11, Eindhoven University of Technology, 1973
LOW 73a Lowes, P., Mol.Phys.Group Rep.NO-73-15, Eindhoven University of Technology, 1973
LUC 73 Lucas, C.B., Vacuum 23(1973)395

MAI 71 Maitland, G.C., and Smith, E.B., Mol.Phys. 22(1971)861
MAR 55 De Marcus, W.C., and Hopper E.H., J.Chem.Phys. 23(1955)1344
MAR 56 De Marcus, W.C., Union Carbide Nuclear Company, Oak Ridge Gaseous Diffusion Plant, Report 1302, parts I-IV, Oak Ridge, Tennesee (1956/1957)
MEN 74 Menger, P., Mol.Phys.Group, Rep. NO-74-18, Eindhoven University of Technology, 1974
MIC 49 Michels, A., Wijker, H and Wijker, Hub., Physica 15(1949)627
MIL 69 Miller, D.R., and Andres, R.P., Rarefied Gas Dynamics (ed. L.Trilling and H.Y.Wachman), Academic Press, New York, 2(1969)1385
MOR 64 Project SQUID Techn. Rep. UVA-4-P-1, University of Virginia, 1964

NAR 60 Narashima, R., Phys.Fluids 3(1960)476
NAR 61 Narashima, R., J.Fluid Mech. 10(1961)371
NAU 63 Naumov, A.I., Sov.Phys.-Tech.Phys. 8(1963)88
NEU 72 Neudachin, I.G., Porodnov, B.T., and Suetin, P.E., Sov.Phys.-Tech.Phys. 17(1972)848

OLA 69 Olander,D.R., J.Appl.Phys. 40(1969)4650
OLA 70 Olander,D.R., and Kruger, V., J.Appl.Phys. 41(1970)2769
OLA 70a Olander,D.R., Jones, R.H., Siekhaus, W.J., J.Appl.Phys. 41(1970)4388
OWE 52 Owen, P.L. and Thornhill, C.K., Aeronaut. Res.Council Repts. and Memo 2616 (1952)

PAR 72 Parson, J.M., Siska, P.E., and Lee, Y.T., J.Chem.Phys. 56(1972)1511
PAU 65 Pauly, H., and Toennies, J.P., in Advances in Atomic and Molecular Physics, vol. I (ed. D.R.Bates and I.Estermann), Academic Press, New York, 1965
PDP 70 PDP-11, Handbook 1970, Digital Equipment Corporation
PRI 70 Price, D.L., and Sköld, K., Nucl.Instr.Meth. 82(1970)208

RIC 64 Richley, E.A., and Reynolds, T.W., NASA techn. Note D2330, NASA, Washingtom D.C. (1964)

SCO 66 Scott Jr., J.E., Morton, H.S., Phipps, J.E. and Moonan, J.F., Rarefied Gas Dynamics (ed.J.H. de Leeuw), Academic Press, New York (1966)331
SCO 71 Scott, Jr.,J.E., Entropie 42(1971)3
SES 70 Sessink, B.W.L.M., Mol.Phys.Group, Rep. SR-1, Eindhoven University of Technology, 1970
SES 72 Sessink, B.W.L.M., and Verster, N.F., Proceedings 4th Cryogenic Engineering Conf. Eindhoven 1972 (Guilford IPC) 327
SHE 63 Sherman, F.S., Lockheed M Sc Technical Report Fluid Mechanics 6-90-63-61 (1963)
SHE 66 Sherman, F.S. and Ashkenas, H., Rarefied Gas Dynamics,(ed. J.H. de Leeuw), Academic Press, New York, 2(1966)84
SIE 70 Siekhaus, W.J., Jones R.H., and Olander, D.R., J.Appl.Phys. 41(1970)4392
SKO 68 Sköld, K., Nucl. Instr. Meth. 63(1968)114
SLA 74 Slaats, H., Mol.Phys.Group, Rep. NO-74-16, Eindhoven University of Technology, 1974
SMI 66 Smith, C.G., and Lewin, G., J.Vac.Sci.Techn. 3(1966)92
SMI 74 Smits, A., Mol.Phys.Group, Rep. NO-74-21, Eindhoven University of Technology,1974
SMO 10 Smoluchowski, M. von, Ann. Physik 33(1910)1559
SPA 63 Sparrow, E.M., Jonsson, V.K., and Lundgren, T.S., J. of Heat Transfer (Trans. of the ASME) 85(1963)111
STE 62 Stern, T.E., Blaquiere, A., and Valat, J., J.Nucl.Energy A/B 16(1962)499
STE 72 Steijn, R. van, and Verster, N.F., J.Phys.E.:Sci.Instr. 5(1972)691
STI 67 Stickney, R.E., Keating, R.F., Yamamoto, S., and Hastings, W.J., J.Vac.Sci.Techn. 4(1967)10

SWE 70 Swedenburg, R.L., Phipps, J.A. and Scott Jr., J.E., AEEP-3442-102-70-U, University of Virginia, 1970

TAN 70 Tanaka, Y., and Yoshino, K., J.Chem.Phys. 53(1970)2012

UIT 75 Uiterhoeve, P., Mol.Phys.Group, Rep. NO-75-4, Eindhoven University of Technology, 1975

VER 70 Verster, N.F., Mol.Phys.Group, Rep. NO-70-6, Eindhoven University of Technology, 1970

VER 73 Verster, N.F., Book of Abstracts of the VIII ICPEAC (ed. B.C.Cobic and M.V.Kurepa) Belgrade, 1973

VER 73a Verster, N.F. Mol.Phys.Group, Rep. NO-73-1, Eindhoven University of Technology, 1973

VER 75 Verberne, J.F.C., Mol.Phys.Group, Rep. NO-75-2, Eindhoven University of Technology, 1975

VIS 70 Visser, C.A., Wolleswinkel, J., and Los, J., J.Phys.E.:Sci. Instr. 3(1970)483

VUG 75 Vugt, P. van, Mol.Phys. Group, Rep. NO-75-1, Eindhoven University of Technology, 1975

WAH 71 Wahlbeck, P.G., J.Chem.Phys. 55(1971)1709

WAR 69 Ward, J.W., and Fraser, M.V., J.Chem.Phys. 50(1969)1877

WAR 70 Ward, J.W., Bivins, R.L., and Fraser, M.V., J.Vac.Sci. Techn. 7(1970)206

WEY 72 Wey, S.J., and Wahlbeck, P.G.,J.Chem.Phys. 57(1972)2932

WIL 72 Wilmoth, R.G., J.Vac.Sci.Techn. 9(1972)1121

ZIE 62 Zierep, J., "Vorlesungen über theoretische Gasdynamik", Verlag G.Braun (Karlsruhe) 1962

ZUG 66 Zugenmaier, P. Z.Angew. Phys. 20(1966)184

Summary

During the last years it has been realised that to determine the interaction potential for two atoms one has to use information of a variety of experiments, as each experiment only probes a limited part of the potential. Measurements of the velocity dependence of the total cross-section for elastic atom-atom scattering can supply valuable additional information for fixing a unique potential.

This study concerns the development of the time-of-flight method for the velocity analysis of molecular beams and its application to the measurement of the velocity dependence of the total cross-section of the noble gases. The intermolecular potential of Ar-Ar is the best known pair potential of the noble gas atoms, and for this reason we have chosen this system for our first scattering experiments.

A second application of the time-of-flight method is the research on molecular beam sources, both to achieve a better fundamental understanding of their operation and to develop reliable primary and secondary beam sources for the scattering experiment.

Chapter 1 has an introductory character. The history of the experiment is given and the specific aims of the time-of-flight project are discussed.

In chapter 2 we review elastic scattering theory, both in the frame work of classical mechanics and in the quantum mechanical description. Attention is paid to the semiclassical correspondence of classical particle trajectories with the partial waves of the quantum mechanical solution. The total cross-section and the small angle differential cross-section are discussed, with special emphasis on their relation. The results of this chapter are used in chapter 7 to derive the correction on the measured total cross-section, due to the finite angular resolution of the apparatus.

In the first part of chapter 3 we review the information available on the intermolecular potential of the Ar-Ar system. In the second part of this chapter we discuss the measurement of total cross-sections with the molecular beam method, and the time-of-flight method is compared to other methods used.

In chapter 4 it is shown that the single burst time-of-flight method can be developed into a reliable and well calibrated method for the analysis of the velocity distribution of molecular beams. A comparison of the single burst time-of-flight method with the cross-correlation time-of-flight method shows that the two methods are complementary and that the specific experimental circumstances determine which method is to be preferred.

In chapter 5 we discuss molecular beam sources. The peaking factor formalism is introduced, and helps to compare the performance of different types of sources. The effusive and the supersonic source are treated, and recent experimental results are given. The multi-channel source is treated in more detail. For the opaque mode an experimental investigation of the velocity distribution and the angular distribution of the flow pattern is presented. Comparison of these results with Monte Carlo calculations for free molecular flow in a cylindrical channel gives us a good qualitative insight in the process of beam formation.

The design and the performance of the new time-of-flight machine are discussed in chapter 6.

In chapter 7 we present the results of the first scattering experiments with the new time-of-flight machine. The experimental results for the total cross-section of Ar-Ar are in very good agreement with the results predicted with the Barker Fischer Watts potential.

Samenvatting

In de afgelopen jaren is men tot het inzicht gekomen dat het voor een nauwkeurige bepaling van de wisselwerkingspotentiaal noodzakelijk is om informatie van meerdere experimenten te gebruiken, omdat ieder experiment slechts informatie over een beperkt gedeelte van de potentiaal geeft. Metingen aan de snelheidsafhankelijkheid van de totale botsingsdoorsnede voor de elastische verstrooiing van twee atomen kunnen waardevolle aanvullende informatie verschaffen, die kan helpen bij de bepaling van de echte wisselwerkingspotentiaal.

Dit onderzoek betreft de ontwikkeling van de looptijdmethode voor de analyse van de snelheidsverdeling van een molecuulbundel en de toepassing van deze methode op de meting van de snelheidsafhankelijkheid van de totale botsingsdoorsnede van de edelgas atomen. De potentiaal van Ar-Ar is de best bekende potentiaal van alle edelgas paren, en daarom hebben wij dit systeem gekozen voor de eerste verstrooiingsmetingen.

In het onderzoek van molecuulbundelbronnen heeft de looptijdmethode een tweede, belangrijk, toepassingsgebied, zowel voor een fundamenteel onderzoek naar hun werking als voor de ontwikkeling van betrouwbare hoofd- en dwarsbundel bronnen voor gebruik bij de verstrooiingsexperimenten.

Hoofdstuk 1 heeft een inleidend karakter. De historische ontwikkeling van het experiment wordt beschreven en de doelstellingen van het looptijdproject worden geformuleerd.

In hoofdstuk 2 geven wij een overzicht van de theorie van elastische botsingen, zowel in het kader van de klassieke mechanica als in de quantum mechanische beschrijving. De correspondentie van de klassieke deeltjesbanen met de partiële golven van de quantum mechanische oplossing wordt toegelicht. De totale botsingsdoorsnede en de differentiële botsingsdoorsnede voor kleine hoeken worden besproken, en er wordt speciale aandacht besteed aan hun onderlinge relatie. De resultaten van dit hoofdstuk worden in hoofdstuk 7 gebruikt om de correcties te berekenen die, tengevolge van het eindige hoek oplossend vermogen van de opstelling, op de gemeten waarde van de totale botsingsdoorsnede moeten worden aangebracht.

In het eerste gedeelte van hoofdstuk 3 geven wij een overzicht van de beschikbare potentialen voor het systeem Ar-Ar. In het tweede gedeelte van dit hoofdstuk bespreken wij een geïdealiseerde molecuulbundel opstelling voor de meting van een totale botsingsdoorsnede. Het gebruik van de looptijdmethode voor dit soort metingen wordt vergeleken met methoden die voorheen gebruikt zijn.

In hoofdstuk 4 laten wij zien dat de gepulste looptijdmethode ontwikkeld kan worden tot een betrouwbare en goed geijkte methode voor de analyse van snelheidsverdelingen van molecuulbundels. Een vergelijking van de gepulste looptijdmethode met de random-correlatie looptijdmethode toont aan dat beide meetmethodieken complementair zijn en dat de specifieke experimentele omstandigheden uitmaken welke methode de voorkeur verdient.

In hoofdstuk 5 bespreken wij verschillende typen molecuulbundel bronnen. Het piekfactor formalisme wordt ingevoerd, en dit formalisme helpt ons om de werking van verschillende typen van bronnen met elkaar te vergelijken. De ideaal-gat bron en de supersone bron worden

behandeld, en recente experimentele resultaten worden gegeven. Aan de werking van de veelkanaalsbron wordt veel aandacht besteed. De resultaten van een experimenteel onderzoek naar de snelheidsverdeling en hoekverdeling van het stromingsveld in het zogenaamde "ondoorzichtige" regiem worden gepresenteerd. Een vergelijking van deze experimentele resultaten met Monte Carlo berekeningen voor vrije moleculaire stroming in een cylindrische buis geeft ons een goed kwalitatief inzicht in het proces van bundelvorming in het kanaaltje.

Het ontwerp en de werking van de nieuwe looptijdopstelling worden besproken in hoofdstuk 6.

In hoofdstuk 7 behandelen wij de resultaten van de eerste verstrooiingsmetingen met de nieuwe looptijdopstelling. De experimentele resultaten voor de totale botsingsdoorsnede van Ar-Ar zijn in zeer goede overeenstemming met de voorspellingen van de Barker-Fisher-Watts potentiaal.

Nawoord

Een groot onderzoeksproject als beschreven in dit proefschrift is ondenkbaar zonder de hulp van een groot aantal mensen. Aan de leden en oud-leden van de groep Molecuulbundels, die allen in meerdere of mindere mate hieraan meegeholpen hebben, komt hiervoor mijn vanzelfsprekende dank toe. Met name wil ik noemen ir. A.H.M.Habets, P.Magendans en W. van Renen die alle drie bij de ontwikkeling van de nieuwe looptijd machine een belangrijke bijdrage geleverd hebben.

Een woord van dank komt ook toe aan de vele studenten die bij het onderzoek betrokken zijn geweest.

De beschreven apparatuur is door de werkplaatsen van de CTD met grote zorg vervaardigd.

Het tikwerk en de verdere verzorging van het proefschrift was in handen van Jola Beijerinck, die ik hierbij bedank voor alle steun die ik ondervonden heb bij de tot stand koming van dit proefschrift.

Levensloop

25 juni 1945	geboren te 's-Gravenhage
juni 1962	eindexamen HBS-B aan het Utrechts Lyceum, gevestigd op de methode Montessori , te De Bilt
september 1962	aanvang studie aan de Rijksuniversiteit Utrecht
september 1964-augustus 1965	assistent college demonstraties
juni 1968-februari 1970	assistent natuurkunde practicum voor bijvak-studenten
februari 1970	doctoraal examen natuurkunde Rijksuniversiteit Utrecht
maart 1970	wetenschappelijk medewerker van de Afdeling der Technische Natuurkunde van de Technische Hogeschool Eindhoven

STELLINGEN

I

Als de condensatie waarschijnlijkheid of "sticking coefficient" γ vrijwel gelijk aan 1 is, zoals bij een cryopomp voor een molecuulbundel, is het voor een zinvolle meting van γ noodzakelijk om een meetmethode te kiezen die gevoelig is voor de reflectie waarschijnlijkheid $(1 - \gamma)$.

A.H.M.Habets, N.F.Verster en Q.A.G. van Vlimmeren, Rev.Sci.Instr. 46(1975)613

L.L.Levenson, J.Vac.Sci.Techn. 8(1971)629

II

De onnauwkeurigheid in de bepaling van een totale botsingsdoorsnede voor elastische atoom-atoom verstrooiing is tenminste gelijk aan tien procent van de correctie die, ten gevolge van het eindige hoekoplossende vermogen van de meetopstelling, op de gemeten waarde aangebracht moet worden.

III

De beschrijving van het intensiteitsprofiel van een supersone bron met de piekfactor en de virtuele bron is te verkiezen boven een beschrijving met de gebruikelijke parameters als de dichtheid en de snelheidsverdeling ter plaatse van de skimmer.

A.H.M.Habets, H.C.W.Beijerinck en N.F.Verster, Proc.IX RGD, Göttingen, 1974

J.B.Anderson, R.P.Andres en J.B.Fenn in Adv.Chem.Phys., vol 10, (ed.J.Ross) Academic Press, New York, 1966

IV

In een omgeving waar vrije moleculaire stroming optreedt is de locale dichtheid n_p gegeven door de integraal $n_p = (4\pi)^{-1} \int n_w \, d\Omega$ over de ruimtehoek Ω, waarbij n_w de dichtheid bij het wandoppervlak is dat vanuit p in de richting Ω gezien wordt. Deze uitdrukking speelt een belangrijke rol bij het ontwerp van een molecuulbundel apparaat.

S.O. Colgate, Vacuum 21(1971)483

V

Metingen in het thermische energiegebied van de snelheidsafhankelijkheid van de totale botsingsdoorsnede voor de verstrooiing van metastabiel $He(2^1S)$ en $He(2^3S)$ aan He in de grondtoestand kunnen uitsluitsel geven over de hoogte van de potentiaal berg in de wisselwerkingspotentiaal.

S.A.Evans en N.F.Lane, Phys.Rev. 188(1969)269
H.Haberland, C.H.Chen en Y.T.Lee in Atomic Physics, vol. 3 (Plenum Press, New York, 1973) 339

VI

De detectie van alkalimetalen met resonantie fluorescentie is gevoelig en snel genoeg voor toepassing in een looptijdexperiment. De te verwachten detectie efficiency is van de grootte orde van 10^{-3}.

F.C.M.Coolen, L.C.J.Baghuis, H.L.Hagedoorn en J.A. van der Heide, J.Opt.Soc.Am. 64(1974)482
F.C.M.Coolen en H.L.Hagedoorn, J.Opt.Soc.Am., wordt gepubliceerd

VII

Uit de hoekverdeling van een bundel atomaire waterstof, die onder omstandigheden van vrije moleculaire stroming uit een lange cilindrische buis stroomt, kan men de -kleine- recombinatie waarschijnlijkheid γ voor één enkele botsing met de wand bepalen. De numerieke resultaten van Livshits e.a. voor de hoekverdeling $f_\gamma(\Theta)$ worden voor grote hoeken Θ in zeer goede benadering beschreven door $f_\gamma(\Theta) = (1 - \gamma)^{\langle p_T \rangle} f(\Theta)$, waarbij $f(\Theta)$ de hoekverdeling is voor $\gamma = 0$ en $\langle p_T \rangle$ het gemiddelde aantal botsingen van een deeltje met de wand is voordat het de buis aan de uitgang verlaat, zoals berekend door Beijerinck e.a..

A.I.Livshits, I.M.Metter en L.E.Rikenglaz, Sov.Phys.-Techn.Phys. 16(1971)276
H.C.W.Beijerinck, M.P.J.M.Stevens en N.F.Verster, wordt gepubliceerd (hoofdstuk 5.3 van dit proefschrift)

VIII

Het verdient aanbeveling dat ieder stage- en afstudeerverslag van de afdeling der Technische Natuurkunde van de T.H.Eindhoven voorzien is van een samenvatting in de Engelse taal.

IX

Bij het werken met een experimentele onderzoeksopstelling moet de veiligheid van de experimentator gewaarborgd zijn. De verantwoordelijkheid hiervoor ligt niet alleen bij de experimentator zelf; ook zijn naaste omgeving behoort hierop toe te zien en moet ingrijpen bij het niet naleven van doeltreffende veiligheidsnormen.

X

Het verdient aanbeveling dat iedere natuurkunde student in de na-kandidaats fase van zijn studie lid wordt van de Nederlandse Natuurkundige Vereniging.

XI

In de begroting van de studietoelage van een student is een stelpost van *f* 300,-- opgenomen voor studieboeken en collegedictaten. Om de aanschaf en het gebruik van studieboeken te stimuleren, verdient het aanbeveling om bij een studiebeurs dit bedrag beschikbaar te stellen als krediet bij een wetenschappelijke boekhandel.

XII

Duurzame huishoudelijke apparaten behoren bij aankoop voorzien te zijn van uitgebreide technische service documentatie.

H.C.W.Beijerinck

Eindhoven, 5 september 1975